POLITECNICO DI MILANO

School of Industrial and Information Engineering

Master of Science
in
Engineering Physics – Nanophysics and Nanotechnology

Effects of spatial confinement on charge order in $YBa_2Cu_3O_{7-\delta}$ studied by Resonant X-ray Scattering

Supervisor: Prof. Giacomo Claudio Ghiringhelli
Co-supervisor: Dr. Riccardo Arpaia

Author:
Leonardo MARTINELLI
Matr. 896783

Academic year 2018 - 2019

Politecnico di Milano:
www.polimi.it

School of Industrial and Information Engineering:
www.ingindinf.polimi.it

"And no one showed us to the land
And no one knows the wheres or whys
But something stirs and something tries
And starts to climb towards the light."

Pink Floyd, *Echoes*

Contents

List of Figures

List of Tables

Sommario

Il presente lavoro di tesi riguarda l'analisi degli effetti di confinamento spaziale sull'ordine di carica nell' $YBa_2Cu_3O_{7-\delta}$ (YBCO) mediante *Resonant X-Ray Scattering* (RXS). L'YBCO appartiene alla famiglia dei cuprati superconduttori, di cui rappresenta probabilmente l'esempio più studiato. I cuprati sono una classe di materiali ceramici famosi per esibire proprietà superconduttive a temperature molto più alte di quelle previste dalla teoria BCS, elaborata negli anni '50 da Bardeen, Schrieffer e Cooper. Questa, tuttavia, non è l'unica peculiarità di questi materiali, che possiedono altre proprietà elettroniche non spiegabili attraverso l'ordinaria teoria delle bande: tra questi, appunto, la presenza di modulazioni spaziali della carica nei piani di CuO_2 con periodo incommensurato al reticolo cristallino. Tali onde possono essere osservate mediante l'utilizzo di scattering risonante di raggi X all'edge L3 del rame. L'importanza di tali fluttuazioni di carica risiede nel fatto che esse manifestano una chiara competizione con la superconduttività alle basse temperature: tale scoperta ha motivato negli ultimi anni la comunità scientifica a svolgere una serie di esperimenti volti a comprendere la natura e le caratteristiche di quest'ordine di carica. La speranza è quella di poter trovare in questo fenomeno la chiave per spiegare l'origine microscopica della superconduttività in questa classe di materiali.

L'elaborato di tesi si inserisce appieno in questo contesto. Il lavoro, di carattere sperimentale, è basato su due esperimenti di RXS effettuati presso la beamline UE46-PGM1 del sincrotrone Bessy II. Il primo, tenutosi a Gennaio 2019, ha riguardato lo studio di campioni nanopatternati di YBCO orientato lungo l'asse c; il secondo, a cui ho attivamente partecipato, ha utilizzato film sottili dello stesso materiale orientati lungo la direzione [100]. In entrambi gli esperimenti, quindi, i piani di CuO_2 risultano confinati: nel primo caso dalla geometria della struttura, nel secondo dallo spessore del film. Le misure raccolte sono state in seguito analizzate e confrontate con alcune simulazioni. I dati mostrano una chiara riduzione del segnale di Charge Order già quando le dimensioni dei piani a-b del campione vengono ridotte fino a qualche centinaio di nanometri. Tale evidenza è inaspettata, dal momento che la lunghezza di correlazione di queste modulazioni non supera i 10 nm. Questo risultato, che necessita di future conferme, sembra suggerire che il charge order sia sensibile ad effetti che hanno luogo su scala mesoscopica.

Abstract

In this thesis, I focus on the effects of spatial confinement on charge order in $YBa_2Cu_3O_{7-\delta}$ (YBCO), studied with *Resonant X-Ray Scattering* (RXS). YBCO belongs to the family of cuprate superconductors, among which it probably represents the most studied example. Cuprates are a class of ceramic materials, famous for exhibiting superconducting properties at temperatures above the limits imposed by BCS theory, formulated in the '50s by Bardeen, Schrieffer and Cooper. This is, however, not the only peculiarity of these crystals, which display other electronic properties not explained by the standard band-theory: among them, indeed, the presence of spatial modulations of electronic charge with a period not commensurate to the underlying lattice. These can be detected by the use of resonant x-ray scattering at Copper L3 edge. The importance of such charge density waves resides in the fact that they exhibit a clear competition with superconductivity at low temperatures. This evidence encouraged the scientific community to perform a series of experiments devoted to understanding the nature and the characteristics of this charge order. The hope is to find, in this phenomenon, the key to explain the microscopic origin of superconductivity in this class of materials.

This dissertation fits precisely in this context. The thesis work, prominently experimental, is based on two RXS experiments performed at beamline UE46-PGM1 at Bessy II synchrotron facility. The first of them, held in January 2019, probed nanopatterned samples of YBCO; the second one, in which I participated, used thin films of the same material grown along [100] direction. In both cases the CuO_2 planes are then confined: in the former by the geometry of the structure, in the latter by the film thickness. Acquired data has been subsequently analysed and compared to some numerical simulations. They show a clear reduction in the charge order signal when the dimension of *a*-*b* planes is shrunk down to some hundreds of nanometers. This is interesting, since the correlation length of such modulations is lower than 10 nm. This result, which needs further confirmation, seems to suggest that charge order is sensitive to phenomena taking place at the mesoscale.

Introduction

After their discovery in the mid 90s, charge density modulations in cuprates have attracted increasing attention. They are universally present in cuprates, and they are now believed to be an intrinsic instability of the superconductive CuO_2 planes; despite that, however, their characteristics differ significantly between different cuprate families. The interest in charge order revolves not only around its mysterious properties, but also around its relationship with superconductivity. The fact that they are present only in superconducting samples, and absent in parent compounds, has over the year spurred the realization of complex experiments to understand their nature. Despite these efforts, however, a satisfactory theoretical framework is still missing and further research and ideas are required. A recent work of Campi et al. showed that charge order is spatially anti-correlated with the presence of oxygen defects in $HgBa_2CuO_{4+\delta}$ [1]. Despite the name, these oxygen inhomogeneities are not randomly-distributed; on the contrary, they have a certain degree of mesoscopic correlation, and are thus referred to as "quenched disorder". This study suggested that charge density waves could be affected by phenomena taking place at the mesoscale and reinforced the idea that the secrets of superconductivity could lie in this length scale. Following this result, this work studies how charge order is affected when CuO_2 planes are confined to nano- and micro-metric dimensions in samples that maintain their superconductive properties unaltered. These unique samples have been grown and fabricated at the Microtechnology and Nanoscience Department of Chalmers University of Technology (Göteborg, Sweden).
In chapter 1 I will give an introduction to high temperature superconductivity and charge density waves in cuprates, reviewing their main phenomenological aspects and briefly discussing some new advances concerning their theoretical interpretation. I will present a chronological review of the most important discoveries concerning charge order, together with a summary of similarities and differences in its manifestation among cuprate materials. In particular, I will focus on YBCO, since it will be the material studied in this master thesis.

In chapter 2 I will present Resonant X-Ray Scattering, the technique which has been used in this work. Starting with a general introduction to the physical mechanism at the basis of the technique, I will then report the modern theoretical description of the resonant scattering process. Finally, I will also describe the layout of UE46-PGM1, the beamline of Bessy II synchrotron facility where we have performed the experiments. I will briefly explain how the undulator, the optics and the diffractometer work, reporting some critical figures.

In chapter 3 I will present the first part of experimental results, regarding charge order in nanopatterned samples of YBCO. In section 3.2 I will describe the

characteristics of the samples used and give some details on how the experiment has been performed practically. Section 3.3 will report the experimental results, which show a clear reduction of charge order signal far greater than the reduction in sample surface, meaning that charge density waves are suppressed by some kind of effect. Finally, in section 3.4 I will critically discuss the results presented in the previous section, comparing them with some numerical simulations performed on Matlab. I will show that this decrease in signal is compatible with the presence of a "dead zone" at the edges of the sample which does not favour the presence of charge order. This hypothesis could be partially justified referring to the article of Campi et al., supposing that, for some reasons, oxygen patches have a stronger correlation there.

Chapter 4 will be dedicated to the study of charge order in a-axis oriented films. First, I will review some issues encountered in the previous analysis of nanopatterned structures, mainly related to the presence of edges and lateral surfaces of the dots; I will then explain how the use a-axis films effectively solved these problems. Section 4.2 will give a brief explanation of how these unique samples have been realised, and will again give some details about how the measurements have been performed. The next section (4.3) presents the results, which confirm what had been found on YBCO nanodots: charge order signal is suppressed when the lateral dimensions of a-b planes are shrunk down to some hundreds of nanometres. Moreover, they also show that waves directed along the non-constrained b axis give still appreciable signal.
Future work will surely involve the use of RIXS, to see whether this reduction affects Charge Fluctuations [2] too.

Finally, I have inserted an appendix about some preliminary results regarding $PrBa_2Cu_3O_{7-\delta}$ (PBCO), a non-superconducting material with the same crystal structure of YBCO. These have been obtained during the measurements on a-axis films, because PBCO was used as a seed layer in the samples. In particular, we have detected a strong superstructure peak located at an incommensurate value of H and some temperature-dependent peaks, which seem to suggest the presence of an unidentified phase transition around 60 K. These preliminary measurements will deserve further investigation.

Chapter 1

Charge Order in Cuprates

1.1 High Temperature Superconductivity

High-critical Temperature Superconductivity has been one of the hottest and most intriguing topics in physics for the last 30 years. It still remains probably the biggest unsolved problem in condensed matter physics due to the complexity of its phenomenological aspects: as of now, no theory exists capable of explaining these properties at a microscopic level. Even if there are other compounds which exhibit non-conventional superconductivity, such as Ruthenates and heavy fermion superconductors, HTS are surely the most famous ones: this is not only for the importance of the topic *per se*, but also because of their possible technological applications.

Among all of materials that superconduct above the common assumed Bardeen-Schrieffer-Cooper (BCS)-limit of 40 K, in this thesis we focus on cuprate perovskites, which can achieve the highest critical temperatures ever recorded (if we exclude the conventional superconductor H_2S, which needs extreme pressures to reach the superconducting state) but have been paradoxically the first one to be discovered.

1.2 Brief introduction to the physics of cuprate perovskites

The BCS theory elaborated in the late '50s provided an excellent explanation of all the conventional superconductors that were discovered until that moment. The main idea behind that theory is that superconductivity is caused by the condensation of electron-electron pairs, also called Cooper pairs, whose formation is driven by a rather small attraction that binds them. The "glue" that holds them together and (partially) wins the strong Coulomb repulsion is due to phonons: by interacting with the positive ions of the lattice, electrons bind into states with lower energies. In particular, a rather simple calculation [3] shows that two free (zero-energy with respect to Fermi surface) electrons that are coupled by a constant, two-particle potential can form a state with (negative) energy directly proportional to ω_D, the Debye frequency of phonons (the so called "Cooper instability"). However, the value of this energy is reduced by an exponential factor and is thus much smaller

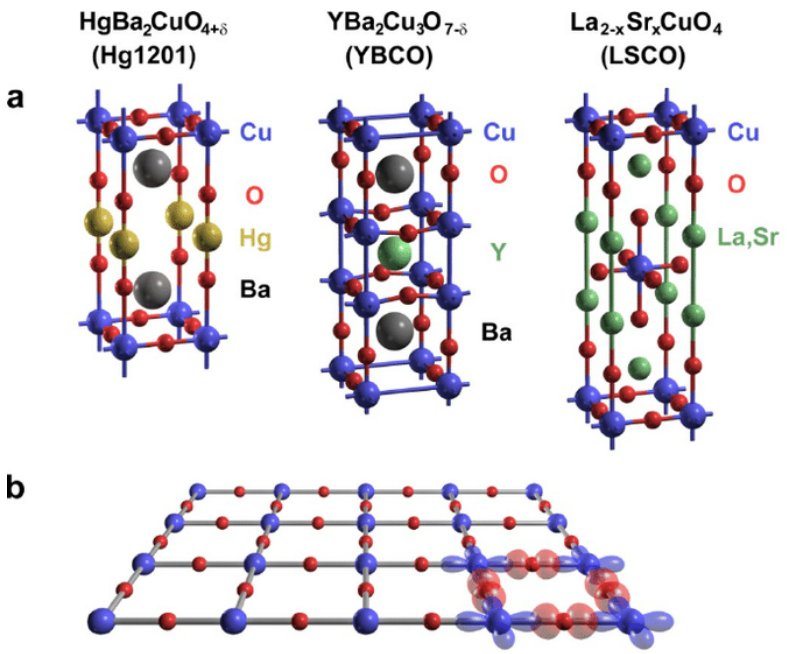

Figure 1.1: Crystal structures of some selcted cuprates: monolayer Hg1021, YBCO, LSCO. (a) shows the unitary cell, while (b) shows a CuO_2 plane, highlighting the $3d$ and $2p_{x,y}$ orbitals of Cu and O involved in the bonding. Taken from [5].

than the phonon energy: for this reason, it was believed that no superconductors could be found with a critical temperature higher than 30 K, since this small gap is easily destroyed by thermal energy. This belief was proved false in 1986, when Bednorz and Muller [4] discovered that the Lantanum - based copper oxide perovskite $La_{2-x}Ba_xCuO_4$ became superconductive at 35 K, well above all the previous known materials. Shortly after, many more superconducting cuprates were discovered, with record critical temperatures reaching 90 K in 1987 (YBCO) and 165 K in 1994 (HgBaCaCuO under pressure).

Despite having different chemical composition, the crystal structures of these materials have some strong similarities (see figure 1.1. The unitary cell is rather complex with one (or more) 2-D planes composed of CuO_2 plaquettes, separated by some electronically inert buffer layers, which contain oxygen and one or more heavy atoms (like Hg, Ba, or rare earths). The core of a cuprate are the above mentioned CuO_2 planes, where superconduction takes place. The orbital configuration of these planes is shown in figure 1.1. X-Ray Absorption (XAS) experiments reveal that each Copper atom is in a $3d^9$ state [6] and has thus one hole in the d subshell. The polarization dependence [6] of the L3 absorption edge of these Cooper atoms, which gets greatly depressed when polarization axis is parallel to c, suggests that the hole occupies the $3d_{x^2-y^2}$ orbital, which has intuitively higher energy since it is coordinated with oxygen $2p_x$ and $2p_y$ filled orbitals. Despite having an integer odd number of holes per unit cell, these planes are, at least in the parent compounds (i.e. non doped cuprates), highly insulating and are described in terms of a (Charge-Transfer) Mott insulator [7]: the high hopping barrier U, which is the cost of having two electrons occupying the same orbital, prevents any tunnelling between atoms

and the resulting gap is of the order of 2 eV [8]. Also, a single hole means that each Cu atom has a 1/2 spin: the virtual hopping of these spins, which would be impossible if they were all aligned in the same direction (due to the Pauli exlcusion principle), produces a Néel antiferromagnetic state.

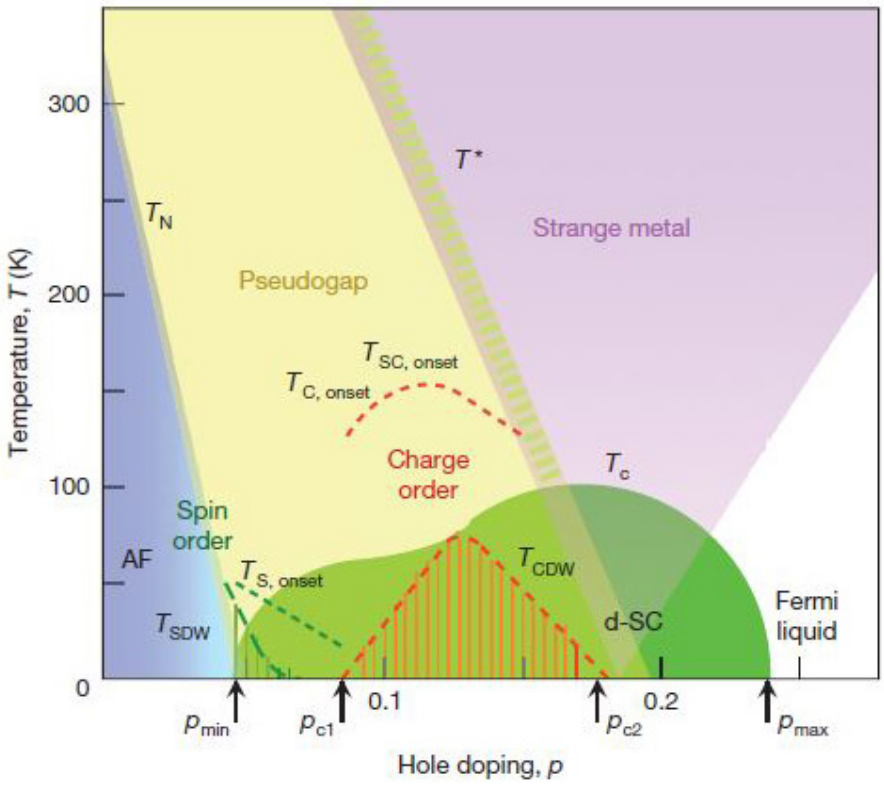

Figure 1.2: Phase diagram of a generic cuprate as a function of doping and temperature. Green part of the figure is the superconducting dome. T_{SC}, T_C and T_S are the onset temperatures of superconductive, charge and spin correlations. Arrows indicate Quantum Critical Points for charge order and superconductivity. Taken from [8].

The fascinating properties of cuprates manifest themselves, however, as doping is introduced. These materials can be doped either by adding or removing electrons from CO_2 planes; however, since this thesis deals primarily with YBCO, we will limit ourselves to the description of what happens in hole doped materials. Doping is introduced in two primary ways: in some cuprates, like in the 214 family, through the chemical substitution of a certain fraction of the heavy element (for example, in LSCO Lantanum is substituted with Sr or Ba); in other, like the 123 family, through the addition of oxygen atoms ($YBa_2Cu_3O_{6+\delta}$) [9]. These new anions populate the buffer layers between the superconducting CuO_2 planes. At low dopings, they randomly form CuO_4 "ribbons" sharing two vertices, while at higher dopings they aggregate into stripes which act as charge reservoirs, and holes start to be injected in CuO_2 planes. As can be seen from figure 1.2, this terribly complicates the phase diagram of cuprates. When doping p is increased, the antiferromagnetic order is rapidly suppressed; however, due to a strong magnetic coupling ($J \approx 140$ meV), spin fluctuations survive also in the non-magnetic state in the form of paramagnons [10].

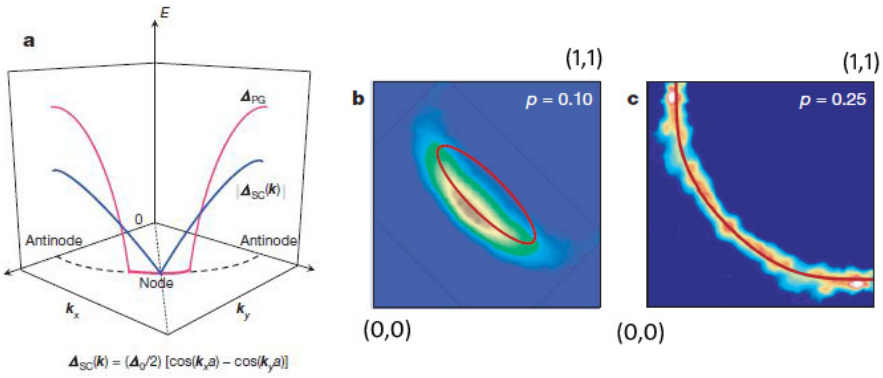

Figure 1.3: Fermi arcs and superconductive pseudogap. (a) shows both gap in superconductive regime (blue figure) and Fermi arcs (red curve). (b) shows Fermi arcs as measured with ARPES in Na-CCOC at p=0.1. (b) shows FL Fermi surface measured in Ti-2201 at p=0.25, where pseudogap phase is suppressed. Readapted from [8] and [13] (figures in (b) and (c) come from experiments by K. Shen and A. Damascelli, respectively).

As doping is increased to a certain p_{min} which depends on the material ($p_{min} \approx 0.05$ in YBCO), the superconducting state sets in. In particular, as shown in figure 1.2, the critical temperature (T_c) increases with p until a maximum is reached, and then decreases back to zero after a certain p_{max}. Compounds with a doping lower and higher than the optimum one are called underdoped or overdoped, respectively. It is nowadays more or less established that, contrary to conventional superconductors which exhibit a singlet s-wave pairing, HTS show a d symmetry (i.e. it changes sign upon a rotation of 90°) [11, 12]. Another striking difference with respect to. Low-Temperature Superconductors (LTS) is the existence of gapless excitation which reveal that cuprate are not fully gaped [8].

As the temperature is raised above T_c in the underdoped regime, cuprates enter the so called "pseudogap" regime. This is a unique state of matter which is not common to any other strongly correlated electron system, characterized by a strong suppression of electron density of states near the edges of the 2-D Brillouin zone. As said, also in the superconducting regime the gap shrinkes to zero in the nodal region (along the diagonal, where the d wavefunctions vanish) and is described by the simple law shown in figure 1.3. However, upon entering pseudogap state, a larger region around the nodal one becomes gapless, and as a result the Fermi surface becomes discontinuous [14]: a spectrum of these features, obtained through Angle-Resolved Photoemission Spectroscopy (ARPES), is present in figure 1.3. This strange "Fermi arcs" grow when doping is increased, until they occupy the entire momentum space. To complicate the situation, this phase of cuprates is enriched by a great amount of competing orders. Magnetic [10] and superconducting [15] fluctuations are indeed present below temperatures T_S and T_{SC}; moreover, as will be deeply explained later, also charge fluctuations (as a precursor of the static Charge Order) are present below an onset temperature T_{CDW}, which is ≈ 150 K for YBCO, depending on doping [16]. In some cuprates of the LSCO family, charge and spin order even coexist in the form of the so called "stripes" [17]. Finally, nematicity has also been observed [18] in this phase: this is zero-Q breaking of

the point symmetry of the structure, which remains translationally invariant but which goes from C_4 to C_2 point group [8]. Some of these orders are expected to cause a reconstruction of the Fermi surface in what have been called "Fermi pockets": these strange features have been predicted to explain the low frequency oscillations measured in Quantum Oscillation (QO) experiments [13]. Finally, when temperature is raised again above the so called T^* and doping is high enough, pseudogap phase evolves in the so called "Strange Metal" state: this is not a unique feature of cuprates and it is found also in other highly correlated electron materials. While becoming a conductor thanks to the doping, the conductivity is about 2 orders of magnitude lower than it should be in a system ruled by the Fermi liquid (FL) paradigm [8, 19]; also, its frequency and temperature dependence are different from those of normal metals. For example, resistivity retains a linear behaviour even at temperatures high enough that l (electron mean free path) becomes smaller than λ (the de-Broglie wavelength of the electron) [8], in principle violating Heisenberg's principle. Optical and thermal conductivity and other physical quantities also show unexpected behaviours: for example, optical conductivity follows a non-Drude-like $\propto 1/\omega$ behaviour [19, 20]. Finally, in the strong overdoped regime, these materials go back to a rather normal FL state with $1+p$ electrons per (2-dimensional) unit cell. This "Strange Metal" phase is so poorly understood and so important that some argue that any theory aiming to explain high-temperature superconductivity should be able to reproduce these results first [21]. Many theories have been proposed to explain these strange phenomena, but two of them have received greatest attention: the Resonating Valence Bond theory and the Marginal Fermi Liquid. We will just briefly introduce the latter, because there Charge Density Waves play a fundamental role. This framework moves from the unexpected simple result that all strange macroscopic features of the "strange metal" phase (optical and thermal conductivity, resistivity, and so on) can be accounted for by introducing a phenomenological charge polarizability with an anomalous form [19]. One of the most famous ideas to give a microscopic justification to this strange polarizability function is to suppose that, in the phase diagram of cuprates, there exist an instability ending in a Quantum Critical Point at zero temperature (i.e. a second order transition at zero temperature driven by a certain parameter, such as doping). At non-zero T, this would create long-ranged and long-lived (low energy) excitations which mediate a strong momentum-independent electron-electron interaction, and thus a scattering mechanism possibly destroying the Fermi Liquid character of the quasiparticles (and maybe binding them in Cooper pairs). One of the candidates for these excitations are, indeed, Charge Density Fluctuations [2, 20] (see section 1.3.3).

1.3 Charge Density Waves

Charge order is defined as a particular phase of matter in which electrons self-organize into a periodic pattern, thus breaking the normal translational symmetry of the underlying lattice. Due to the fact that the modulation is (more or less) sinusoidal, charge order also takes the name of Charge Density Wave. Like other types of symmetry-breaking phases, charge order is found in highly-correlated electron systems. In these materials, the strong Coulomb repulsion felt by electrons

in d or f orbitals can easily overcome the reduction of kinetic energy driven by hopping, and thus forces the material to find new ways to lower its total energy, often by breaking of translation or rotational symmetry. Charge order manifest itself in several different ways in HTS, depending on the cuprate family. Additionally, in some cuprate superconductors this phase even coexists with Spin Density Waves in the from of the so called "stripes", and in all of them (at least for some values of doping) it even coexists with superconductivity, despite competing with it, as will be explained in a while.

1.3.1 Chronological review

Stripe order in LSCO

Charge order in cuprates has been first detected in the from of stripe order in the 214 family, i.e. in Lantanum-based perovskites of the form $La_{2-x}A_xCuO_4$, where A can be an alcali atom (such as Sr or Ba) or a rare earth (such as Eu or Nd) and is used to dope the material. This is an ordered phase in which charge and spin order coexist, as will be explained in the following. Since the first probe used to study HTS were neutrons, which strongly interact with magnetism, the spin ordering was discovered first [22]: it manifested itself as a set of four incommensurate peaks (1/2 $\pm\delta_S$, 1/2, 0) and (1/2, 1/2 $\pm\delta_S$) around the normal AF wavevector (1/2, 1/2), with the parameter $\delta_S \approx$0.125 being doping dependent. Stimulated by theoretical simulations, which predicted the intertwining between spin and charge order, Tranquada et al. found evidence of both type of peaks in La_2NiO_4 and in a LNSCO [17] sample with $p \approx 0.125$, and shortly after Yamada et al. resolved the doping dependence of the incommensurability vector δ [23]. The fact that stripe order was first detected in LNSCO rather than in LSCO is not a coincidence: being a 1-D modulation, stripe formation is favoured by the breaking of the fourfold rotational symmetry of CuO_2 planes; the substitution of some La atoms with Nd indeed breaks the tetragonal symmetry of the lattice. Such a difficulty in observing charge-related peaks comes from the fact that neutron are not sensible to charge, and can reveal modulations of electron density only indirectly through the subsequently induced lattice distortion. The set of peaks measured by Tranquada is shown in figure 1.4: apart from the already mentioned four magnetic peaks, they found also two charge-related peaks split from the Bragg reflection (0,2,0) by an amount $\delta_{CH} = 2\delta_S$. Moreover, Yamada found that, at least when $p < 0.125$, the spin incommensurability follows the simple rule $\delta_S = p$; after that value, it somewhat saturates. This suggested the structure presented in figure 1.4: doped holes segregate into charge "rivers" which separate undoped antiferromagnetic domains; the period of such a structure depends on the number of holes available, and thus on doping. This, along with the fact that the doping p = 0.125 plays a special role, has been explained theoretically in the framework of strong real space correlations: extra holes tend to organize in half-filled stripes, and what varies is the spacing between them. After $p = 0.125$, however, the structure remains the same and extra holes tend to occupy the existing stripes. For this reason, this type of order is still regarded as commensurate to the lattice.

The most interesting part of the experiments, however, was the relation between

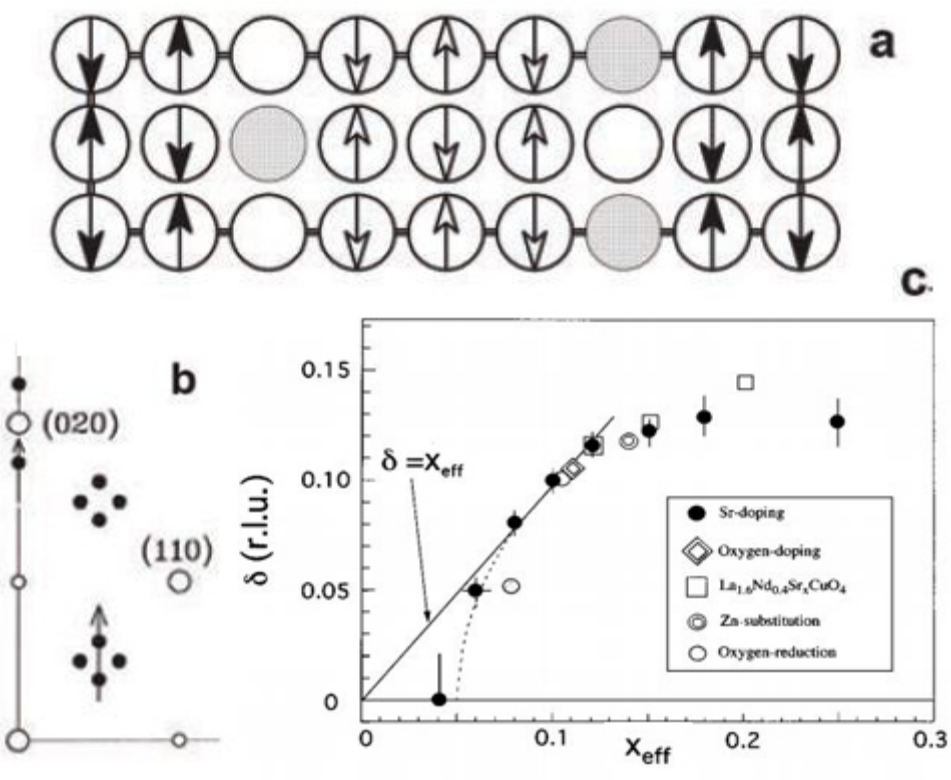

Figure 1.4: Panel (a) shows the real space structure of a stripe for $p = 0.125$. Circles are Cu atoms, while the Arrows indicate direction of spins. Grey circles show the position of holes. Panel (b) shows a scheme of the peaks detected by Tranquada through INS: white dots are Bragg peaks, while black ones are charge and spin order peaks (Note how the discommensuration for charge is two times the one of spin). Panel (c) shows the doping dependence of the spin order discommensuration δ for the effective doping x. Readapted from [17] and [23].

stripe order and superconductivity. Analysing the width (in reciprocal space) of the stripe order peaks, Yamada found that it was anomalously small at the usual p=0.125, meaning that the correlation length of stripes is higher. At the same time, other experiments had revealed that the superconducting $T_c(p)$ had a depression at that precise value, though suggesting a competition between stripe order and superconductivity. Moreover, the minimum dopings required to observe stripes and superconductivity coincided, with a value around $p \approx 0.08$, thus deepening the intertwining between thee two phenomena.

Charge order in Bi-compounds: real and reciprocal space

The next cuprate family in which charge order was discovered was the Bismuth one. In these particular perovskites, the relative weak interaction between adjacent BiO planes makes it possible to obtain plain surfaces through cleavage. This, in turn, allows to study these materials through real-space sensitive techniques such as Scanning Tunnelling Microscopy (STM) and Scanning Tunnelling Spectroscopy (STS). In particular, the current flowing through a nanometric tip put very close

to the sample (at a distance of some Å) is recorded as a function of the position over the sample's surface; by changing the voltage between tip and sample it is also possible to obtain information about the Density of States (DOS) of the material (applying an electric potential roughly means shifting the energies of the electronic states). In 2002, Hoffman et al. [24] discovered charge order in Bi2212 under the application of a magnetic field. In particular, they applied a 5 T field,

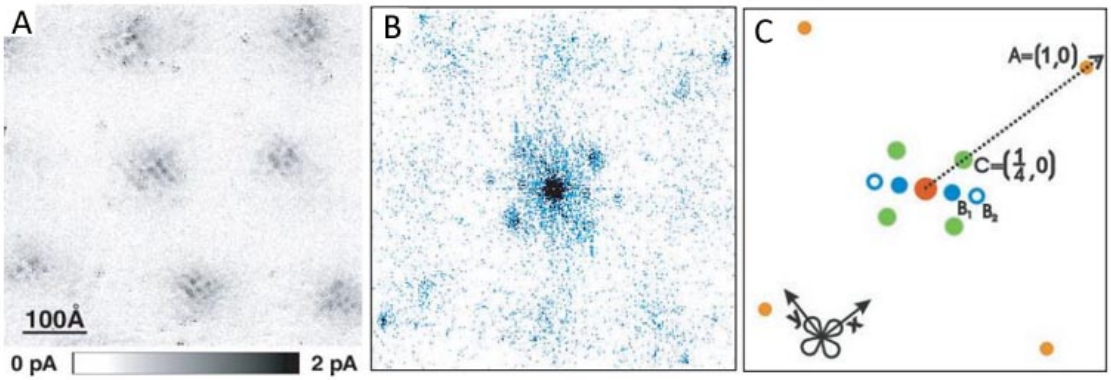

Figure 1.5: STM images of Bi2212 under the application of a 5 T magnetic field. Panel (A) shows the real space image of differential conductance dI/dV. Magnetic vortexes are evident, with a dimension of ≈ 100 Å, along with a modulation of electronic density. Panel (B) is the power spectrum of the Fourier Transform of panel (A), and panel (C) is a schematic of the peaks visible in (B). A set of four peaks around (±0.25,0) and (0,±0.25) appears, indicating a modulation with period $4a_0$, shown in green in panel (C). Orange dots are Bragg peaks, while blue ones represent a supermodulation independent from magnetic field. Readapted [24].

higher than the lower critical field H_{C1} of the material, thus creating vortices in the superconducting phase. Inside these regions, they found evidence of a period-4 modulation of electron density directed along Cu-O bonds, shown in figure 1.5, with a typical "checkerboard" pattern. The Fourier transform of the real space signal is shown in the same figure: a set of four peaks in (±0.25, 0) and (0, ±0.25) is detected only with a magnetic field B present (the other small peaks are remnants of a supermodulation present even without B). By fitting a Lorentzian function to these features, the authors estimated a FWHM $\sigma \approx 0.011$ Å^{-1} which corresponds to a very small correlation length of ≈ 30 Å in real space. Moreover, they discovered that the position of these peaks was completely insensible to the applied voltage, thus ruling out any involvement of quasi-particle interference effect. Moreover, the fact that this type of order was detected only inside the non-superconductive vortexes again suggested a competition between these two phases.

Incommensurate Charge Order in YBCO

While charge order had been found in La-based, Bi-based and Ca-based cuprates, no clear evidence of it had been found in 123-family before 2012. Some hints of the presence of a periodic modulation of the charge were first given by measurements of the Hall resistance R_H in very high magnetic field and very low temperatures,

which revealed a Fermi surface reconstruction compatible with a density-wave phase [22]. Subsequently, NMR measurements on UD YBCO at 28 T signalled a change in the ^{63}Cu(2) line at a temperature similar to the critical one: such a splitting was probably due to a periodic change in electronic density in the Cu-O planar bonds. Finally, the development of RIXS enabled the detection of CDW in the 123 family at zero magnetic field: a work by the group of G. Ghiringhelli and L. Braicovich [25] showed the clear presence of static charge order in a broad range of doped YBCO and UD $Nd_{1+x}Ba_{2-x}Cu_3O_7$, which is structurally equivalent to the more common YBCO (the only difference is that oxygen chains are fully oxygenated, and doping is controlled through the ratio of Nd and Ba compositions). In particular,

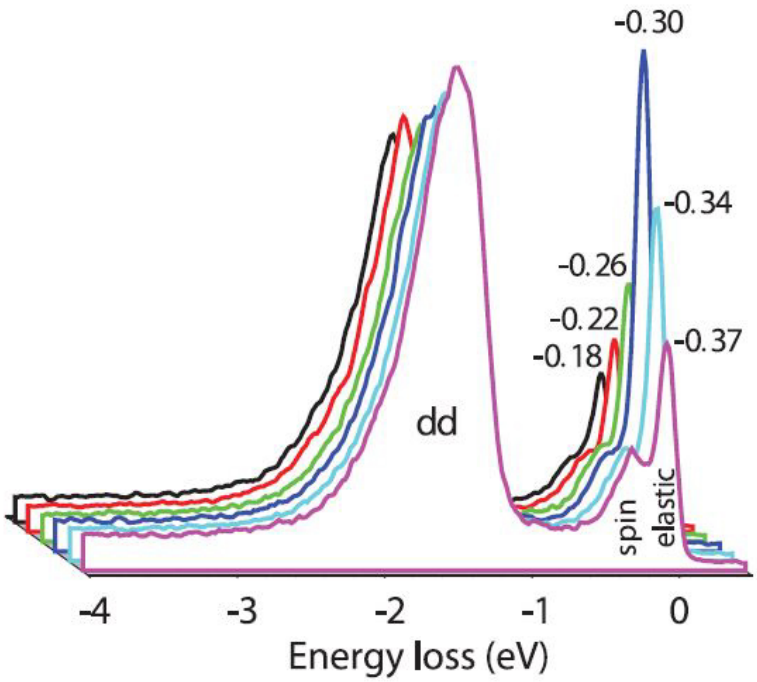

Figure 1.6: Waterfall plot of RIXS energy scans for various H values in reciprocal space (units in r.l.u.). As can be seen, a strong enhancement of the quasi elastic signal is present for $H = 0.31$ r.l.u. . Readapted from [25].

using energy-resolved RXS (RIXS) on NBCO with $p \approx 0.11$ they detected a strong increase of the quasi-elastic signal around a wavevector (0.31,0) in reciprocal space when using σ polarized (perpendicular to scattering plane) radiation: many aspects proved that it was related to a purely static charge order. First, signal was greatly reduced with the use of π polarization (lying in the scattering plane), which can be explained with geometrical considerations: π polarization has a component also along c, which clearly does not probe charge order in a-b planes. Secondly, the subsequent use of a polarization analyser for the outcoming radiation revealed that the peak disappeared when beams were cross polarized ($\sigma\pi'$ configuration), meaning that no spin flips (and thus no spin order) is present (at least in the accessible part of the Brillouin zone). Moreover, the fact that RIXS is a resonant process means that it can selectively excite phenomena involving the atoms for which the absorption edge has been tuned: in this case, CDW were only observed when the incoming beam resonated with Cu(2) L3 edge, while they were absent

for Cu(1) edge. This clearly demonstrate that charge order is a feature of CuO_2 planes, and not, for example, of Copper atoms residing in oxygen chains. Finally, temperature dependence showed again a direct competition with superconductivity, while doping dependence was similar to Bi-compounds and completely different from LSCO (see figure 1.11b). Such a measure is important for two main reasons. First, because the modulation found has a periodicity completely incompatible with the underlying lattice. While someone has tried to reconcile this with the more traditional commensurable stripe order of La-cuprates suggesting the presence of discommensurability regions throughout the sample [26], this picture seems quite unreasonable and doesn't find any simple connection to experimental data [27]: CDW in YBCO are now widely believed to be truly incommensurate, with a period of 1.23 nm which corresponds to 3.2 real lattice parameters. Secondly, the fact that the modulation involves only charge, and not spin, makes it radically different from stripe order (this will be discussed in the next section). The direct

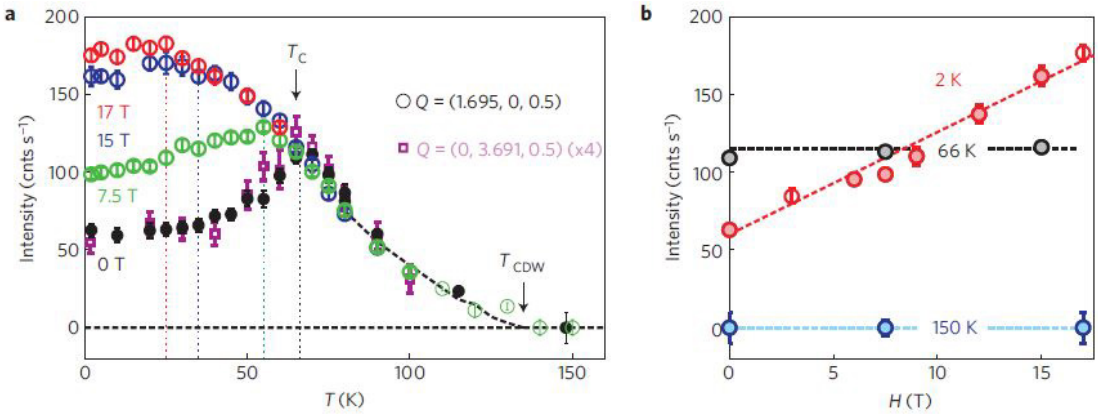

Figure 1.7: Competition between charge order and superconductivity measured by Chang et al. Panel (a) shows the temperature dependence of charge order peak for various magnetic fields: 17 T (red), 15 T (blue), 7.5 T (green) and 0 T (black and purple). Panel (b) shows clearly that intensity if affected by H only when $T < T_c$. Taken from figure [28].

competition between charge order and superconductivity in YBCO was observed the same year in another work by Chang et al. [28] using X-Ray Diffraction (XRD). They analysed the intensity of charge order peak in magnetic fields B up to 17 T. They found that while the intensity is unaffected by the presence of B above the critical temperature, it greatly increases with B below T_c (see figure 1.7): they therefore concluded that this enhancement is only due to the suppression of superconductivity. The width followed a similar (but opposite) trend, being still insensitive to B above superconducting transition and decreasing (signalling an increase in the real-space coherence length) with B below T_c. In addition, they were able to measure charge order peak both along a and b direction, although with different experimental resolutions. This prevented them from establishing whether the peaks came from a bi-directional modulation in real space (checkerboard pattern), or from a random disposition of unidirectional "stripe-like" modulations. Charge order in $YBa_2Cu_3O_{6+x}$ was further (and deeply) explored by Blanco-Canosa et al. [29] in 2014 using REXS. They measured charge order in broad range of

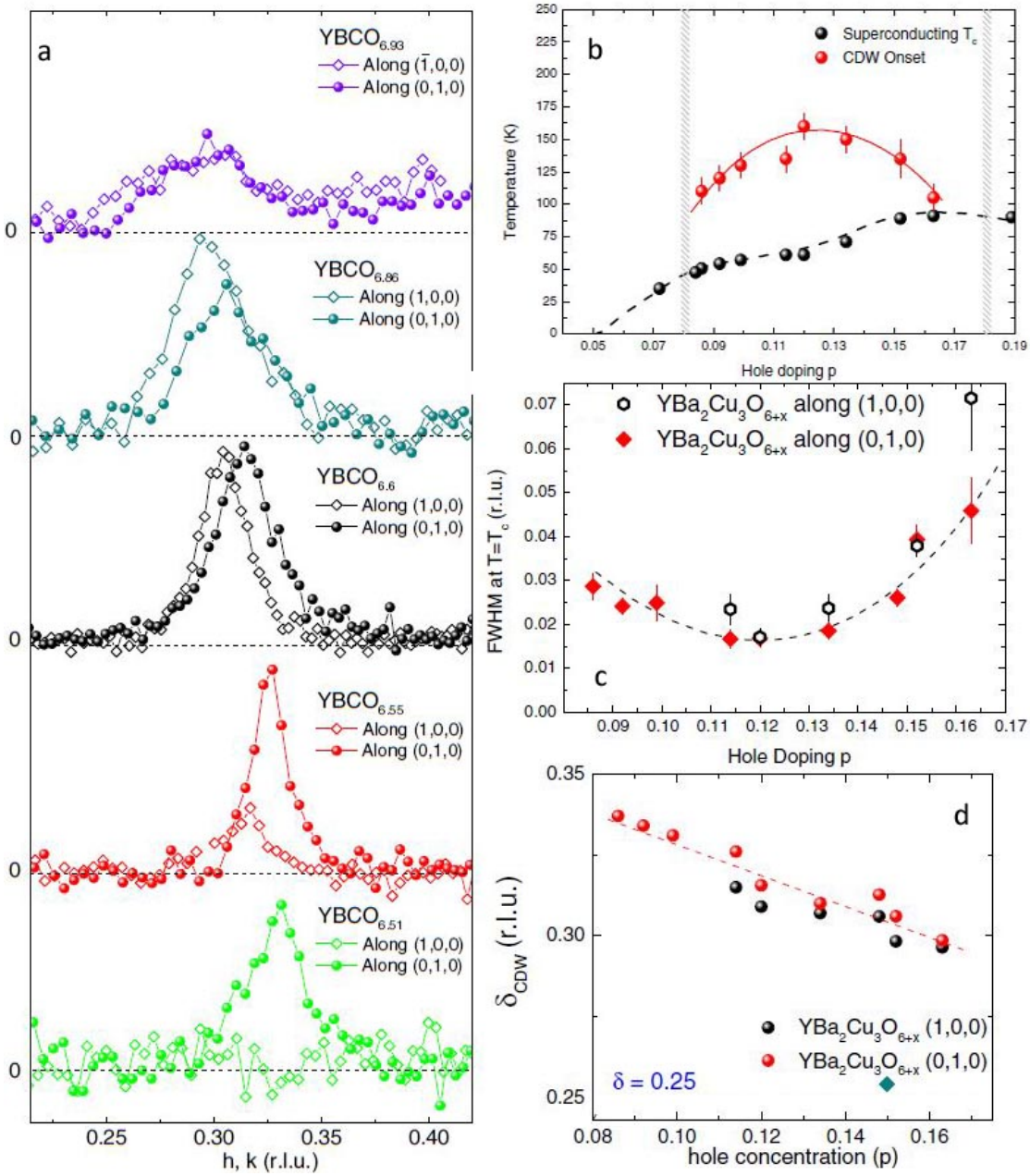

Figure 1.8: Panel (a) shows charge order peak along h and k for various dopings: as can be seen, there's a clear anisotropy. Panel (b) shows T_c and the onset temperature of CDW. Panel (c) shows the FWHM as a function of the doping, revealing a minimum at $p = 0.12$. Panel (d) highlights the doping dependence of charge order wavevector. Readapted from [16].

oxygen content $6+x$ between the strongly underdoped and the optimally doped, at different temperatures and along both the two in-plane directions. While they confirmed all the previous results (incommensurate wavevector, competition with superconductivity, enhancement in a magnetic field below T_c), they were also able to explore the doping dependence of CDW onset temperature, wavevector and intensity, and also to detect an anisotropy between h and k peaks. Their findings are summarised in figure 1.8. Charge order intensity is highest at a doping value $p \approx 0.12$, and it is absent (along k) when $x < 0.45$ ($p < 0.08$) or $x > 0.99$ ($p > 0.189$). Correspondingly, the correlation length ξ is maximum at $p = 0.12$ and decreases elsewhere, demonstrating that at this doping charge is indeed stronger. Interestingly, this p value is also associated to a plateau in the critical temperature, as shown in figure 1.8. Additionally, the peak along h seems to be present for a smaller range of dopings ($0.114 < p < 0.189$) and a slightly lower wavevector, revealing a clear anisotropy in charge order. Its intensity follows a strange pattern, being lower than the k-peak one for $x < 0.6$ ($p = 0.12$) and larger for $x > 0.6$: this is interesting, because the doping at which charge order is strongest ($p = 0.12$) seems to have almost-isotropic charge order compatible with checkerboard pattern, while at higher and lower dopings the anisotropy increases suggesting a "stripe-like" modulation. While one would be tempted to associate this anisotropy to the commensurate order of the additional oxygen atoms in CuO stripes (see figure 1.1), the authors rule out this possibility by noting that the anisotropy increases for $x<0.55$, but the coherence length of this oxygen order decreases in this doping range.

CDW in Hg-family

The only remaining cuprate families in which charge order had not been yet observed were the Hg family and in the electron doped cuprates (NCCO). In 2014, following some Quantum Oscillation measurements that revealed a Fermi surface reconstruction [5], Tabis et al. [30] found evidence of CDW in monolayer Hg1201 using both RIXS and REXS, with a peak located at $H \approx 0.28$ r.l.u. in momentum space and again in the quasi elastic part of the energy spectrum. Width of the peak pointed towards a correlation length in real space of just approximately 5 lattice constants, similar to what measured for Bi-compounds. Temperature dependence of the peak revealed an onset near $T \approx 200$ K, which is very close to T^{**}, the temperature at which the material transits from a pure pseudogap phase to a state more similar to ordinary Fermi-liquids (at least in transport measurements), like explained in [5, 30]. Moreover, the fact that only resonant techniques were capable of detecting CDW means that the effect is very small, and this can be considered another hint of CDW-superconductivity competition, since Hg-family has the highest T_c among all cuprates. However, this could be also due to the fact that Hg-family has a pristine tetragonal unit cell, and thus possess highest symmetry among other compounds.

Electron doped cuprates

Finally, charge order was found in electron-doped NCCO the next year by da Silva Neto et al. [31] after (again) Quantum Oscillation studies which revealed a

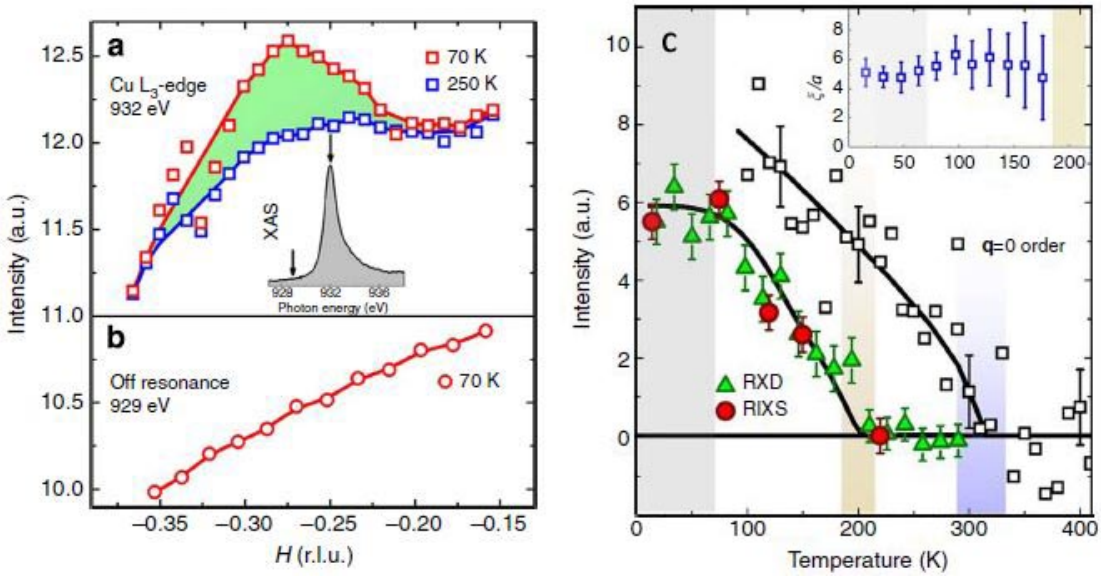

Figure 1.9: CDW in Hg1201 measured by Tabis et al. Panel (a) and (b) show two H scans taken with RXS at Cu L3 edge and off resonance, respectively. Panel (c) shows the temperature dependence of charge order peak intensity (green triangles and red dots) and $q = 0$ antiferromagnetic order (white squares). The brown and blue region indicate T^* (pseudogap onset temperature) and T^{**} (pseudogap-FL transition temperature). Inset shows that CDW correlation length has no temperature dependence. Readapted from [30].

Fermi surface reconstruction at doping $p \approx 0.15$. In particular, they found a broad charge order peak using Resonant X-Ray scattering around H=0.25 r.l.u. and estimated a very short real-space correlation length of approximately 2 nm, similar to Bi-based cuprates. The big difference with respect to hole-doped cuprates was in the temperature dependence: here, charge order seems to build up from a very high T of $\approx$ 340K: this is much higher than what expected and rules out the possibility of a connection between charge order and emerging of the pseudo gap phase (at least in this system) (figure 1.10). Instead, this temperature is compatible with the onset of AF fluctuations.

To conclude, all these findings reveal that charge order is an ubiquitous phenomenon in cuprates, and is now widely believed to be an intrinsic instability of CuO_2 planes. Moreover, charge order seems to compete with superconductivity in all of these systems, meaning that the two phenomena have similar energy scales. Despite these similarities, however, striking difference remain in doping and temperature dependence, wavevector associated to the modulation and connection to magnetism (stripe vs pure charge order). We will now present a brief summary of what has been said until now, and we will proceed in analysing and the latest findings in this field.

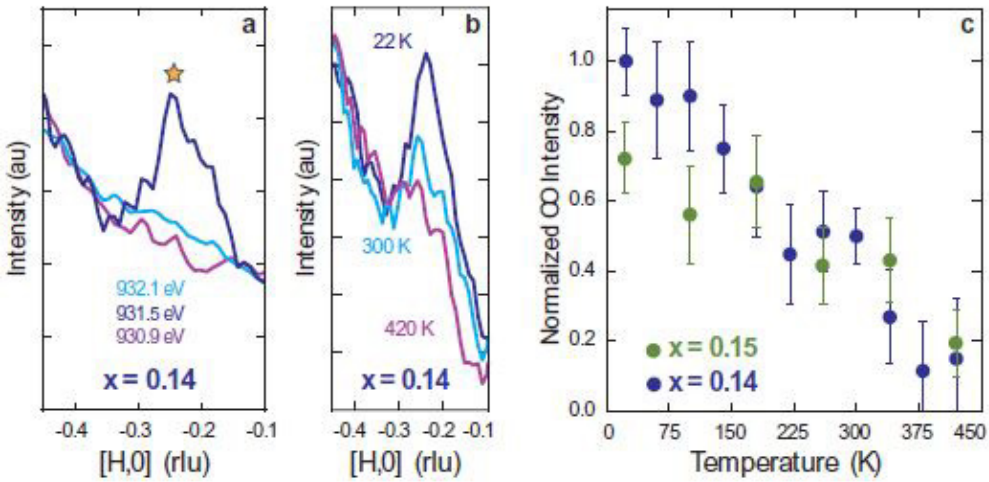

Figure 1.10: Charge order detected in electron doped NCCO. (a) is an H scan at different photon energies, and shows that a charge order peak is detectable only at Cu(2) L3 edge. (b) shows scans at different temperatures, and (c) compares peak height with temperature. Readapted from [31].

1.3.2 Summary: doping, temperature and wavevector

The next figures (1.11a and 1.11b), taken from [22], are a summary of the properties of charge order among all different cuprate families. Starting with the doping dependence of charge order wavevector, we see that two major trends are visible (figure 1.11b): for La-based compounds, where charge and spin order are present simultaneously, position of CDW in reciprocal space reaches the commensurate value of 0.25 r.l.u at $p = 1/8$ and saturates; instead, for the 123-family and Bi-based systems, wavevector has a more monotonic behaviour and decreases at higher doping values. For other compounds, such as Hg-family, electron doped and Ca-based compounds, further investigation is required to confirm any trend. These differences, however, do not surprise too much given the completely difference type of order shown in La-compounds (stripes) with respect to purely charge order. For what concerns the doping dependence of the onset CDW Temperature, in almost every HTS family it reaches a maximum for a doping near $p \approx 0.12$, with coincides with the magical doping of 1/8 of stripe order (figure 1.11a). This particular value is also connected to a suppression of T_c for all cuprates (with the exception of Hg-family, in which the superconducting dome is lowered around $p \approx 0.09$ [30]). However, remarkably, the cuprate families which have the higher onset temperature seem to have also a lower strength charge order, which is maximum for La cuprates, intermediate for YBCO and smallest for Hg and Bi compounds [22]. At the same time, the reduction of T_c is higher for stronger charge (or stripe) order (in some La-based cuprates, it even decrease to zero at $p = 0.125$). While this latter behaviour is easily explained in a competition between charge order and superconductivity, the former seems quite counter-intuitive. Also, it is not clear why charge order should be stronger at $p = 0.12$ also in YBCO and Bi-family, where such vector does not have any particular meaning. Another interesting fact is that T_{CDW} seems to decrease to zero at some particular doping values.

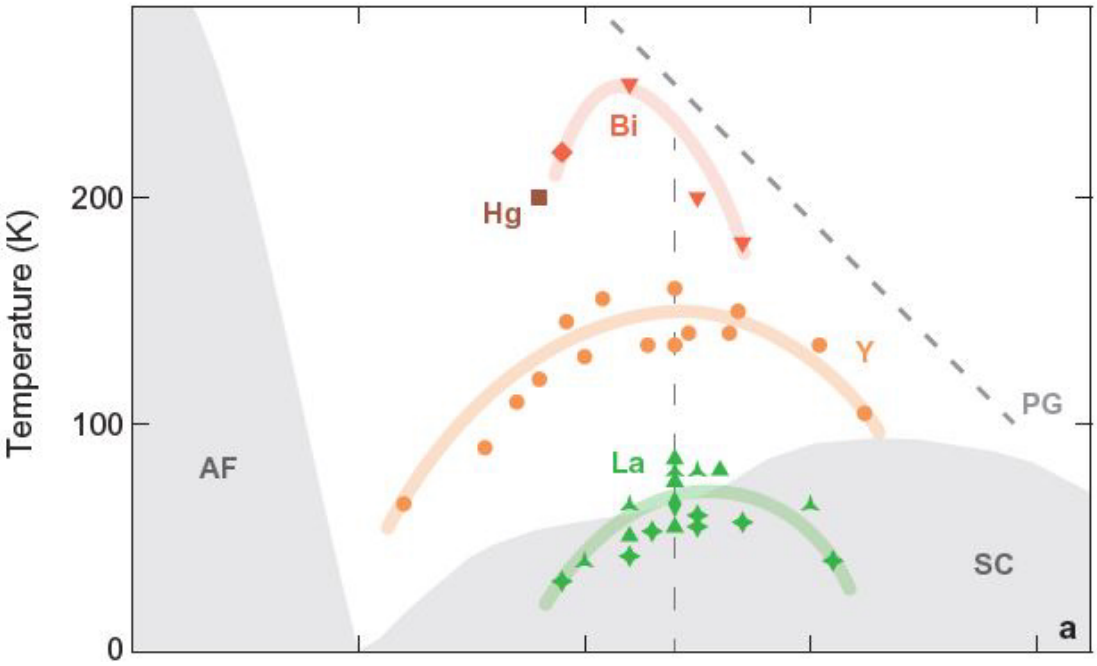

(a)

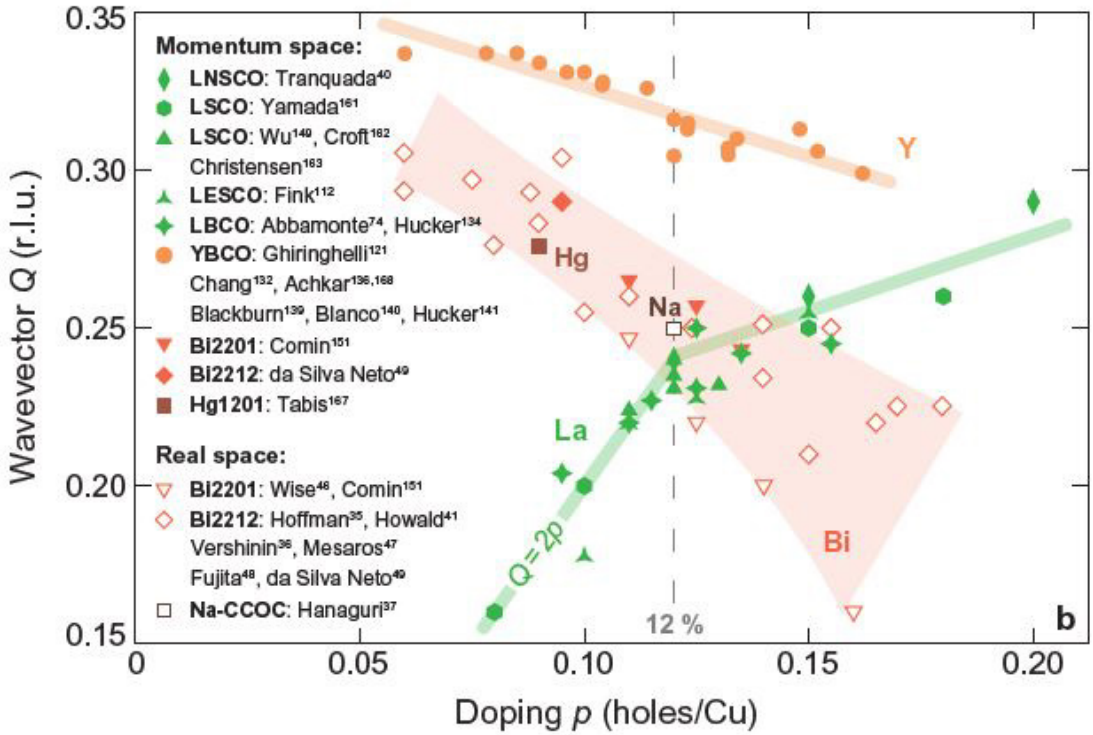

(b)

Figure 1.11: Panels (a) and (b) summarize the doping dependence of the charge order wavevector and onset temperature, respectively, for different HTS compounds, as determined in several experiments. Taken from [22].

For what concerns the theoretical interpretation of CDW, much is still unknown. One of the main questions is: where does the wavevector of charge order come from? While this has received an answer for stripes in LSCO family, where it has been related to the *real* structure of a stripe, we still lack a theory for cuprates characterised by an incommensurate modulation (such as YBCO). As of today, some experimental hints exist only for Bi-compounds, where we have direct access to ARPES data. In particular, a work from da Silva Neto et al. [32] which combined

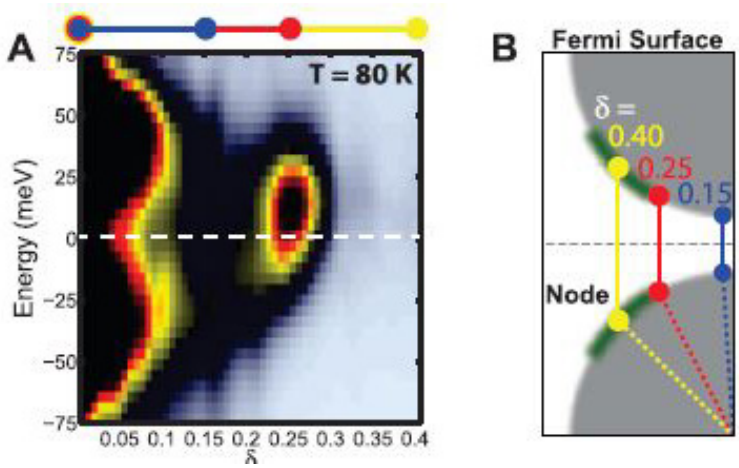

Figure 1.12: Comparison between charge order wavevector and the nesting vector connecting edges of the Fermi arcs in Bi2212. Readapted from [32].

STM and RXS study of Bi2212 showed that charge order's wavevector is related to the so-called *nesting vector*: this is a vector in reciprocal space which connects parallel regions in the Fermi surface (see figure 1.12). Such vectors are "special", in the sense that they provide a strong source of elastic scattering for electrons near the Fermi surface. However, this interpretation of the origin of CDW has not received a general consensus.

1.3.3 Recent Findings

Three dimensional CDW

The fact that charge order intensity increases when cooling the sample, but then this trend stops when the superconducting phase sets in, suggested that in situations where superconductivity is destroyed by other means than temperature (e.g. magnetic fields) one should observe an even stronger (and possibly different) CDW. This spurred an intense research to discover how charge order changes with the application of very high magnetic fields. In 2015, Gerber et al. [33] performed a new type of X-Ray scattering experiment using FEL (Free Electron Laser) radiation and strong magnetic fields. In particular, they created millisecond-lasting pulses of very high B (up to 25 T) in order to suppress superconductivity. At the apex of the pulse, a 50 fs X-Ray pulse provided information on charge order through ordinary scattering. Their findings are summarised in figure 1.13. First, they compared the scans at 0 and 20 T across different temperatures: as expected, an enhancement of CDW peak is obtained only below T_c: this is because this enhancement is

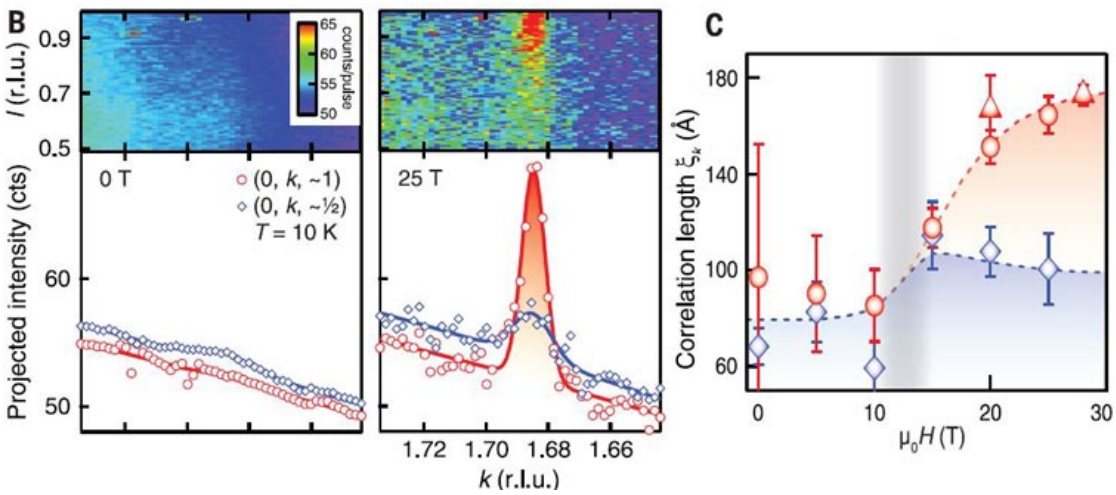

Figure 1.13: Evidence of 3D charge order in high magnetic field. (A) shows scans at 0 and 20 T at three different temperatures: note how charge order at zero field disappears when superconducting phase sets in, while at high field (no superconductivity) it grows in intensity. (B) shows K and L scans at 10 K, for two different B: K position remains the same, while the peak becomes sharp around $L = 1$ r.l.u.. (C) is the correlation length for "peak" at $L = 1/2$ (blue) and $L = 1$ (red). Readapted from [33]

only indirect and is due to the absence of superconductivity. Subsequently, they performed an L dependence of charge order peak at various magnetic fields at a temperature of 10 K. When B is low (0-10 T), the usual [22, 25] flat behaviour is obtained, indicating a 2-D character of the instability; however, after 15 T, a peak starts growing at $L = 1$ r.l.u. and at the same K value as normal charge order. The fact that the peak becomes sharp also along L means that this type of charge order in 3-dimensional and is thus a distinct phase of the system. Moreover, following the peak heights and the correlation lengths at $L = 0.5$ and $L = 1$, they concluded that both types of charge order are simultaneously present, although their relation is still unclear. These results also agree with other NMR measurements performed two years before [34]. The importance of this new phase of charge order is in the fact that it spans a region of the phase diagram which, at zero T, ends at two dopings: $p \approx 0.08$ and $p \approx 0.16$ for YBCO. Since these two points mark a phase transition at zero temperature, they are called Quantum Critical Points (QCPs, shown in figure 1.2 at the beginning of the chapter as p_{c1} and p_{c2}).

CDW and Oxygen defects

Usually, the picture used to interpret charge order consists of uncorrelated islands of unidimensional charge modulations. Since the correlation length of such isles is of the order of the 10 nm (which is the maximum value usually measured in YBCO), one would assume that charge order is affected by effects which take place on a length scale of some nanometers. This is, however challenged by an experiment from Bianconi et al. As already explained before, charge order intensity, position in reciprocal space and onset temperature all heavily depend on the doping

of the material: in the 123 family, this in turn means that it will depend on concentration of oxygen interstitials. The group of Bianconi used XRD with a micrometer spot-size (Scanning μXRD) to study the spatial relation between CDW and presence of oxygen chains on Hg1201 at optimum doping (p =0.12), which is the monolayer cuprate with the highest T_c. They found indeed a very inhomogeneous

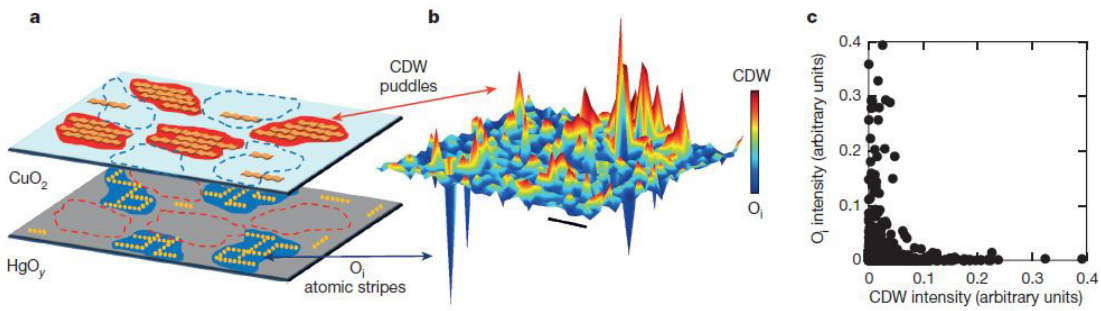

Figure 1.14: Spatial anticorrelation of oxygen puddles and CDW found by Campi et al. in Hg1201. As can be seen, measured intensities of oxygen stripes and of charge order are spatially anticorrelated: points where the former is strong show a lower intensity of the latter, and vice versa. (a) is a scheme of deduced real space configuration, (b) shows a map of measured intensity (red for CDW and blue for oxygen stripes). In (c), each point represent a position in real space scanned by μXRD. Readapted from [1].

pattern of charge order, with an average length of 4.3 nm but with sizes that could reach 40 nm. Moreover, their Probability Density Function (PDF) had a very "fat" exponential tail, which the author claims to be indicative of self-organization near a critical point. Then, they studied the spatial distribution of oxygen interstitials, which organize into stripes directed along a and b, and form streaks that connect Bragg peaks in reciprocal space. They obtained two major results: first, CDW and oxygen defects are spatially anticorrelated (figure 1.14). This is expected, since a higher presence of oxygen increase the doping, which in turn does not favour the formation of charge order. However, they also found that the distribution of interstitials was not completely random as believed before, but exhibited a form of "quenched disorder", which has a mesoscale distribution. This result could imply that also CDW could also be sensitive to effects (as spatial confinement, which is the main topic of this master thesis) which have a characteristic length of hundreds of nm of even μm. Moreover, it indicates that even in cuprates with very ordered crystal structure a mesoscale phase separation remains, and superconductivity will be non-uniform.

Charge Density Fluctuations in RBCO

As explained before, one of the proposed paradigms to explain the anomalous properties of HTS in the normal state is that the FL state is destroyed by strong scattering between the quasiparticles, mediated by fluctuations of some incipient order. After the discovery of 3D CDW, which ends in a QCP (Quantum Critical Point) at $p \approx 0.16$, it would then seem reasonable to identify this quasi-critical

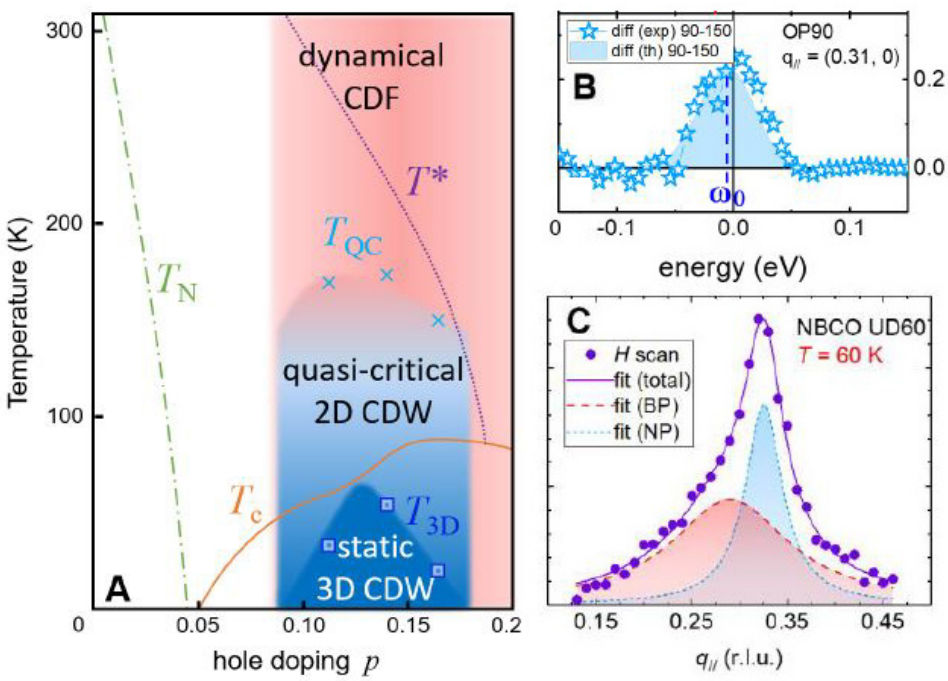

Figure 1.15: Characteristics of Charge Density Fluctuations. (a) shows the new phase diagram proposed after the discovery of CDF. (b) shows the energy peak which gives rise to CDF: as can be seen, it is not centred atzero energy loss. (c) shows the shape of the measured Broad Peak in reciprocal space. Readapted from [2].

order to Charge Density Fluctuations, thought as a precursor to truly static charge order. In 2019, a work by Arpaia et al. [2] possibly has found this type of dynamical excitation using high-resolution RIXS. By measuring the charge order in under-doped (T_c=60 K) and Optimally-doped (T_c=90 K) (Y,Nd)$Ba_2Cu_3O_{7-\delta}$ thin (50 nm) films, they found that the actual peak observed around $H = 0.31$ r.l.u is actually made up by two different peaks: a narrow one (NP), which is the usual CDW peak with a FWHM of ≈ 0.05 r.l.u., and a broader one (BP), with a FWHM of ≈ 0.2 rl.u. (figure (c) of 1.15). The fact that this peak is not related to some sort of intrinsic sample disorder, and is instead due to some sort of "different" charge order comes from many hints. First, it is centred at a similar reciprocal lattice point of the narrow peak and it is not present along other directions. Secondly, it is present only in samples that are superconductive, while it is absent in non-superconductive AF samples. Finally, it appears only when incoming photon energy matches Cu L3 resonance. Its characteristics are, however, very different from the narrow peak usually observed in RXS experiments. It shows a quasi-flat temperature dependence both below and above T_c, meaning that it does not compete (or at least very weakly competes) with superconductivity. Moreover, it is still present at $T = 250$ K and beyond, far above the onset temperature of normal charge order in YBCO: this suggests a new YBCO phase diagram as the one depicted in figure (a) of 1.15. Finally, by taking differences between spectra taken at $H = 0.31$ r.l.u. at 150 K (where narrow peak is almost zero) and 250 K, the authors show that the peak (in energy) which gives rise to the BP is not exactly centred at 0 eV, but it is better

fitted by a curve centred around 15 meV (figure (b) of 1.15. This would mean that the broad peak is associated with a non-static, dynamical excitation. While being an extremely interesting result, further experiments are needed to verify whether this feature is present also in other cuprate families, and to establish the true temperature dependence of its intensity.

Chapter 2

Resonant X-Ray Scattering

In this chapter, we will introduce the experimental technique which has been used in the experiments outlined in the next chapters. Sometimes, features common to both Resonant Inelastic X-Ray Scattering (RIXS) and Resonant X-Ray Scattering (RXS) will be presented, as both techniques share an equivalent physical mechanism. We will then briefly introduce the theoretical formulation of resonant scattering, and finally we will describe the experimental setup of beamline UE46-PGM1 at Bessy II, where we have performed the experiments.

2.1 RXS process and properties

2.1.1 Excitation process

We will start describing qualitatively the physical process at the basis of resonant scattering, underlining the common properties and the differences with respect to RIXS and other spectroscopy techniques; we will present the formal theory in the next section. While being a scattering process, RXS is radically different from ordinary X-Ray Diffraction (XRD) or Inelastic Neutron Scattering (INS), because it is a two-step process. First, a core electron is excited in an higher state above the Fermi level through the absorption of a photon with momentum $\mathbf{q}$, frequency ω and polarization $\boldsymbol{\epsilon}$. This state is highly unstable and rapidly (≈ 1 fs) decays back to a lower energy state: a fraction of these events will be radiative and another photon $\mathbf{q}'$, ω', $\boldsymbol{\epsilon}'$ will be emitted; figure 2.1 shows the scheme of such a process. When $\omega = \omega'$, no energy is given to the sample and thus the scattering is elastic. When instead $\omega \neq \omega'$, some energy (and momentum) are transferred to the material and the process is inelastic. Assuming that initially the system is in the ground state, one can write two simple conservation laws:

$$\hbar\omega = \hbar\omega' + E_{\text{exc}}$$
$$\hbar\mathbf{q} = \hbar\mathbf{q}' + \hbar\mathbf{q}_{\text{exc}}$$

where the subscript *exc* stands for the excitation triggered by the scattering. An additional law regards the polarization of incoming and outgoing photons, which can transfer angular momentum to the material. The momentum transferred to

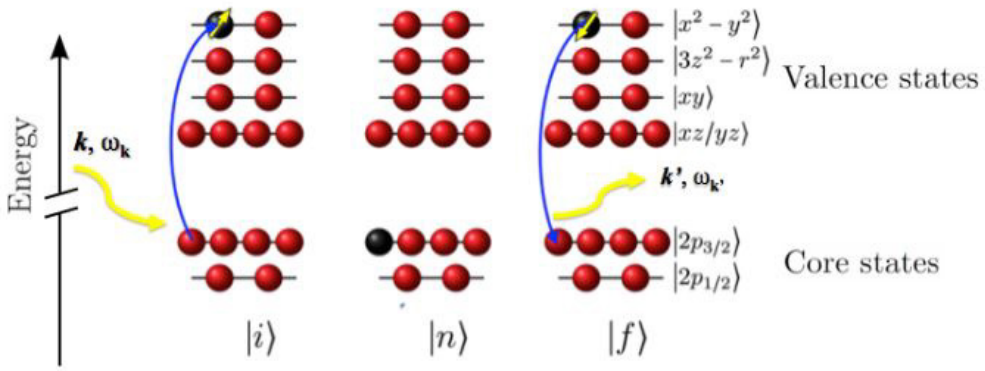

Figure 2.1: Schematic of RXS two-step process, showing the case of Cu L3 edge. From left to right: initially $|i\rangle$, intermediate $|n\rangle$ and final $|f\rangle$ states are shown. Red and black spheres represent occupied and unoccupied states, respectively. Arrows denote the spin, which is a good quantum number only in $3d$ shell. Taken from [35].

the materials is non-negligible for soft (and of course hard) x-rays: when $\hbar\omega = 930$ eV, $\lambda = 13$ Å which is comparable to an average lattice constant.

The choice of the absorption edge involved in the first part of the excitations is crucial for the experiment, since it determines which type of excitations will be observed. For example, a common choice for HTS cuprate is the L3 edge of Copper: this triggers the transition $2p_{3/2} \rightarrow 3d$ of a Cu electron, where 3/2 represents the total angular momentum. Other edges have been explored during the last years, such as oxygen K edge [36] and M edges of rare earth atoms [37] (such as M_5 of Praseodymium, which will play a role in chapter 4).

2.1.2 Properties of RXS

The main advantage of RXS over non-resonant techniques such as high energy XRD, is indeed the resonant enhancement, which allows to detect even very weak excitations or orders. In a pioneering work, Abbamonte et al. [36] used Resonant Soft X-Ray Scattering (RSXS) to study stripe order in LBCO around (0.25, 0, L). They concentrated both on the oxygen K ($\sim$ 530 eV, corresponding to the $1s \rightarrow 2p$ transition) and on the Cu L3 edges ($\sim$ 933 eV, corresponding to the $2p_{3/2} \rightarrow 3d$ transition). They were able to calculate the resonant enhancement of the scattering at the O edge, estimating it to be 82 electrons/holes: this means that each doped hole scatters, at resonance, as 82 electrons in non-resonant scattering. This is the main reason why resonant x-ray scattering (both with and without energy resolution) has become one of the primary tools to study charge order in bulk materials. Radiation in non-resonant processes (as high-energy diffraction) scatters with equal amplitude from every charge in the material, and so CDW intensity (involving just a fraction of electrons per each atom) is totally overwhelmed by Bragg reflections. Indeed, XRD is able to detect charge order only where it is a strong effect, like in La-compounds or in the 123-family close to $p \approx 0.12$ [28].

RXS has also *in principle* access to a pletora of different excitations. The

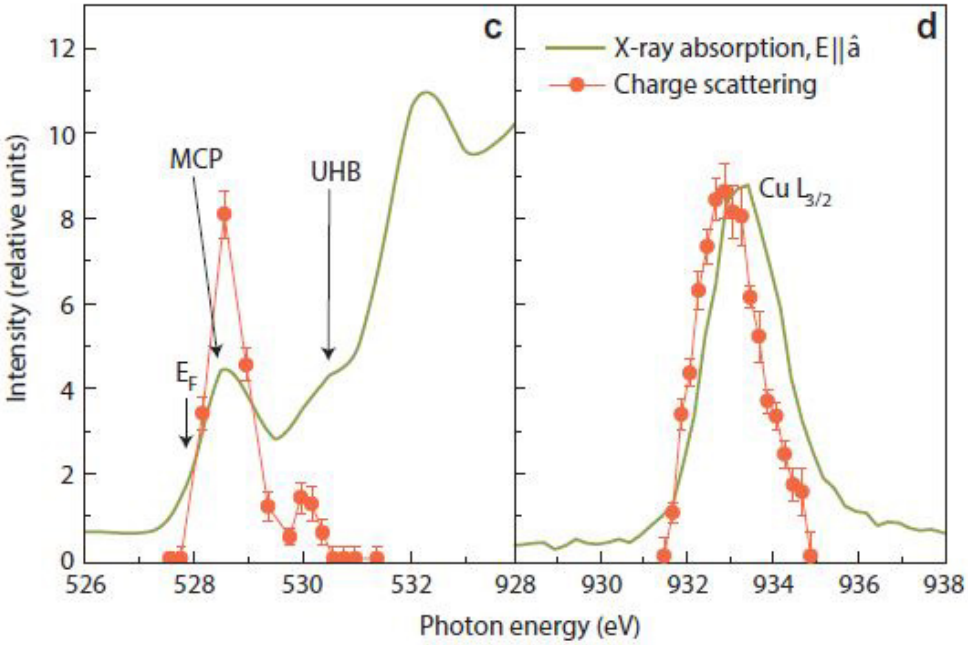

Figure 2.2: Resonant enhancement of RXS, measured by Abbamonte et al. [36] in LBCO. On the left, the intensity of charge scattering (orange dots) is compared to the X-Ray Absorption (XAS) profile around oxygen K edge (green solid line). MCP denotes the mobile carrier peak, corresponding to transitions into the doped hole levels; UHB stands for upper-Hubbard band and the peak is produced by electrons excited to empty d states of Cu atoms. Right panel shows a similar graph at Copper L3 edge. As can be seen, the scattering peak intensity is enhanced in the vicinity of edges. Taken from [36].

fact that the scattering involves a two-step process even allows to easily observe dipole-forbidden transitions, like dd excitations which have $\Delta L = 0$. In particular, the scattered radiation contains components coming from charge scattering (Bragg peaks and CDW), phonons, orbital and magnetic excitations. However, the fact that RXS has no energy resolution severely limits the capability of observing such excitations and one has to resort to the more advanced RIXS to effectively detect them. Correspondingly, RXS has been mostly used to detect charge order in the last years (at least in cuprates), which has a very sharp dependence in momentum-space and can easily be identified in an energy-integrated spectrum. Other applications involve the coupling of charge and magnetic order in ferroelectric materials: a list of works involving RXS and XAS at Bessy beamline can be found for example in [38].

Another advantage of the resonant character is that it provides not only element and orbital sensitivity, but also *site* sensitivity. It is known, indeed, that the absorption edges of atoms are influenced by the chemical environment. Since the resolution of incoming photons is usually very high at synchrotron facilities (< 1 eV in the soft x-ray regime), RXS allows to discriminate between atoms with different oxidation states and coordination. As an example, in the 123-family RXS allows to

discriminate between Cu atoms in CuO stripes and CuO_2 planes [25].

Being a photon-in photon-out spectroscopy, no charge leaves the sample. This means that RXS preserves the neutrality of the system, unlike many other spectroscopy techniques such as direct and inverse photoemission. This is crucial, for example, in experiments involving insulators in order to avoid possible charging problems.

Another important feature of RXS is the spatial "multi-scale" sensitivity, which makes it extremely versatile. The penetration depth of soft x-rays at normal incidence goes from $\sim$ 100 nm to almost 1 μm when $\hbar\omega \rightarrow 1.5$ keV [35]: this makes RXS sensitive to bulk materials, as opposed to other techniques (such as STM) which are only sensible to the surface of materials. At the same time, this penetration length is still much shorter than the one achievable with Inelastic Neutron Scattering, which can reach some cm due to the very weak interaction between neutrons and matter. Correspondingly, while INS needs large samples with a volume of several cm^3, x-rays can work with much smaller crystals, even micrometric ones. Moreover, sensitivity can be tuned by changing the geometry of the experiment: for example, the use of a grazing incident angle allows to reduce the probed depth of a factor $\sin\theta_i$, and thus even thin films (with just a few nm thickness) can be easily investigated [25, 27].

Finally, RXS is a *fast* process: absorption and radiative decay usually last approximately $\tau \sim 1$ fs. This allows to detect small energy excitations of the system, since it does not average out fluctuating signals with a characteristic time bigger than τ. A result is that RXS can detect fluctuating charge order at much higher temperatures than other techniques such as NMR (see for example [28] and [39]).

Finally, as already mentioned before, RXS can transfer a non negligible momentum to the material. For example, in a typical cuprate at Cu L3 edge it is possible to span more or less half of the first Brillouin zone (FBZ) along H direction. While this is clearly better than optical spectroscopies (in which photons carry a negligible momentum), it has the drawback that the maximum transferable momentum is tied to the energy of the resonance. Correspondingly, not all the points of FBZ can be accessed at a given absorption edge: this is a disadvantage with respect to XRD or INS, where instead there are no energy constraints.

So far, we have outlined common properties of RIXS and RXS (or REXS). The difference between them is in what happens *after* the scattering process. While the latter simply detects all the radiation scattered by the sample, RIXS performs an energy (and polarization) analysis of the scattered x-rays. This is a huge improvement since it allows to discriminate between all the different excitations, while RXS simply detects the sum of such elastic and inelastic components. Correspondingly, it is not possible to exactly reconstruct the origin of the observed features. That is the reason for which REXS is often used in combination with RIXS (for example in [25, 30]), or when there is no ambiguity in what is being detected [16, 32]. Sometimes, RXS is also called Resonant *Elastic* X-Ray Scattering, since one is usually interested in the elastic part of the signal. However, as explained above, this is a bit improper, since there's actually no energy resolution. Another disadvantage is that backgrounds are the sum of a huge number of different process, and thus often they have their own (weak) momentum and temperature dependences. This complicates the procedure of taking differences between scans acquired, for example,

at different T, as will be explained in chapter 3. Moreover, even when inelastic components do not vary over the momentum scans and thus form a constant background, signal-to-noise ratio can be even 20 times lower than in RIXS [25]. On the other side, REXS has also some advantages with respect to RIXS. First of all, the overall intensity is higher and less time is required to achieve statistical significance. A REXS momentum scan usually takes just around 5 minutes, while a RIXS one with same number of points in reciprocal space can take some hours. Then, the experimental apparatus is much simpler, as will be explained in the following: correspondingly, also alignment procedures require a smaller amount of time.

2.2 RXS theory

Since RXS is based on the scattering of photons, its theory develops from to the radiation-matter interaction Hamiltonian. While in principle one should start from the full relativistic Dirac equation, even with the use of synchrotron radiation it is usually possible to expand the Hamiltonian for low fields and retain the magnetic, linear electric and quadratic electric terms. Such an approach can be justified by two simple considerations [40]. One can imagine that, in order to avoid Quantum Electrodynamics (QED) effects:

- The velocity of the electrons which enter in the Hamiltonian should be small compared to c. This is more or less always satisfied: for example, when dealing with HTS, one usually excite electrons of Copper atoms. Even for 1s electrons, which should have the highest kinetic energies, one can estimate: $v_{1s} \approx \hbar Z/ma_0 \approx 0.21c$, using Heisenberg principle and supposing that they are confined in a box of more or less a_0/Z size. For such a value of v_{1s}, we have $\gamma \approx 1.02$, and thus relativistic effects are negligible.

- The energy associated with the electric fields should be much lower than the minimum required to create electron-positron pairs ($2m_ec^2 \approx 1$ MeV). This is usually satisfied even in synchrotron radiation, but could break down with the advent of new Free Electron laser facilities, which are expected to reach fields of $E \approx 10^{16}$ V/m.

The calculations shown here closely follow the one reported in [22], with the difference that we use SI units instead of CGS system. Moreover, some formulas and/or justifications have been taken from [40]. Out starting point will be the following Hamiltonian:

$$\begin{aligned} H_{tot} &= \sum_j \left\{ \frac{1}{2m} \left[\boldsymbol{p}_j - e\boldsymbol{A}(\boldsymbol{r}_j, t) \right]^2 + V(\boldsymbol{r}_j, t) \right\} + \sum_{j \neq k} \frac{e^2}{4\pi\epsilon_0 |\boldsymbol{r}_j - \boldsymbol{r}_k|} + H_{EM} \\ &= H_{\text{crystal}} + H_{EM} + H_{\text{int}} \end{aligned} \tag{2.1}$$

where j, k run over all the electron in the system, $\boldsymbol{A}$ is the electromagnetic vector potential (function of space and time), V is the scalar potential associated to the crystal and H_{EM} is the energy of the electromagnetic field, expressed (in second

quantization) through the use of creation and annihilation operators for photons as $H_{EM} = \sum \hbar\omega_{\boldsymbol{q}}\Big(a_\nu^\dagger(\mathbf{q})a_\nu(\mathbf{q}) + 1/2\Big)$. Since it will be used soon, it is worth to remember that $\mathbf{A}$ is written, in terms of these operators, as:

$$\mathbf{A}(\mathbf{r},t) \propto \sum_{\mathbf{q},\nu} \Big[e^{i\mathbf{q}\cdot\mathbf{r}-i\omega t}\ a_\nu^\dagger(\mathbf{q}) + h.c.\Big]\boldsymbol{\epsilon}_\nu \tag{2.2}$$

where ϵ_ν is the polarization vector of the polarization state ν. As can be seen, vector potential is a linear combination of creation (and annihilation) operators. The relevant term in the total Hamiltonian is H_{int}, the interaction term, which can be expressed as (in Coulomb gauge):

$$H_{\text{int}} = -\frac{e}{m}\sum_j \boldsymbol{p}_j \cdot \boldsymbol{A}(\boldsymbol{r}_j,t) + \frac{e^2}{2m}\sum_j \boldsymbol{A}^2(\boldsymbol{r}_j,t) \tag{2.3}$$

As can be seen, the interaction Hamiltonian contains both a linear and quadratic term in the vector potential. To obtain the cross sections, it is necessary to calculate the transition probability associated to the various excitations. Since such an Hamiltonian cannot be exactly diagonalized, the rest of the derivation now proceeds using a time-dependent perturbative approach, for which it is necessary to exactly define the wavefunctions of the unperturbed system. They can be written as $|\Psi_M\rangle = |\psi_m\rangle_{el} \times |\phi_{n_{\boldsymbol{q},\nu}}\rangle_{EM}$, where $|\psi_m\rangle_{el}$ is the electron many-body wavefunction and $|\phi_{n_{\boldsymbol{q},\nu}}\rangle_{EM}$ is the phonon state described (in second quantization formalism) by the occupation numbers $n = \{n_{\boldsymbol{q}_1,\nu_1}, n_{\boldsymbol{q}_2,\nu_2}, ...\}$, where $\boldsymbol{q}$ is the wavevector and ν is the polarization. The transition probabilities between two generic states $|\Psi_{M_i}\rangle$ and $\Big|\Psi_{M_f}\Big\rangle$ can then be expressed *exactly* through a generalization of Fermi's golden rule:

$$w_{i\to f} = 2\pi|\left\langle\Psi_{M_f}|T|\Psi_{M_i}\right\rangle|^2\ \delta(E_f - E_i) \tag{2.4}$$

where $E_{i,f}$ are the initial and final energies of the whole system (electrons + EM field), ad T is an operator defined as:

$$T = H_{\text{int}} + H_{\text{int}}\frac{1}{E_i - H_0 + i\eta}H_{\text{int}} + H_{\text{int}}\frac{1}{E_i - H_0 + i\Gamma}H_{\text{int}}\frac{1}{E_i - H_0 + i\Gamma}H_{\text{int}} + ... \tag{2.5}$$

with Γ being a parameter responsible for the finite lifetime of the state. Of course, such an infinite series is not tractable: the real approximation consists in truncating it after the first two terms (i.e. retaining just the terms linear and quadratic in H_{int}). Being this a scattering process, we can make some important simplifications: since we expect to have the same (total) number of photons in the initial and final states, the matrix element $\langle\Psi_i|T|\Psi_f\rangle$ will be non-zero only if the operator inside the bracket contains terms like $a_\nu^\dagger(\mathbf{q}_f)a_\nu(\mathbf{q}_i)$, which annihilate a photon but create a new one (possibly with different $\mathbf{q}$ and ω. This can happen in two ways: the linear term in equation (2.3) through the quadratic term in (2.5), or the quadratic term in (2.3) through the linear term in (2.5). These produce two different transition

probabilities which (after some passages) can be written as:

$$w^{(1)}_{i\to f} = 2\pi \left| \frac{e^2}{2m} \langle \Psi_f | \sum_j \mathbf{A}^2(\mathbf{r},t) | \Psi_i \rangle \right|^2 \tag{2.6}$$

$$w^{(2)}_{i\to f} = 2\pi \left| \left(\frac{e}{m}\right)^2 \sum_M \frac{\langle \Psi_i | \sum_j \mathbf{A}(\mathbf{r}_j,t)\cdot \mathbf{p}_j | \Psi_M \rangle \, \langle \Psi_M | \sum_k \mathbf{A}(\mathbf{r}_k,t)\cdot \mathbf{p}_j | \Psi_f \rangle}{E_i - E_M + i\Gamma_M} \right|^2 \tag{2.7}$$

where Ψ_M is a generic intermediate state characterized by the quantum numbers $\{m, n\}$, with energy E_M and lifetime $\hbar/\Gamma_M$ (due to the non radiative-processes not accounted for in this equation). In the particular case of elastic scattering, which means that $\omega_{\text{in}} = \omega_{\text{out}} = \omega$, we have that $|\psi_f\rangle = |\psi_i\rangle$. Moreover, in our case this would be *exact*, since charge order is a static charge modulation (as described in chapter 1) and thus associated with an elastic scattering. To calculate the first term, we notice that $\mathbf{A}$ can be expanded as $\mathbf{A} \propto \exp[i(\mathbf{q}' - \mathbf{q})\cdot \mathbf{r}]\; a^\dagger_\nu(\mathbf{q}')a_\nu(\mathbf{q})$. For the matrix element to be non-zero we must then assume that $a^\dagger_\nu(\mathbf{q}')a_\nu(\mathbf{q})\,|\phi_i\rangle_{EM} \propto |\phi_f\rangle_{EM}$. For the second term, we know $E_i = \epsilon_{GS} + (n_{\mathbf{q}_{in},\nu_{in}}\hbar\omega_{\mathbf{q}} + 1/2)$ and that $E_M = \epsilon_m + (n_{\mathbf{q},\nu_{in}}\hbar\omega_{\mathbf{q}} + 1/2 - 1)$. Putting all together, we finally obtain the expressions for the two transition probabilities:

$$w^{(1)}_{i\to f} \propto |\langle \psi_f | \sum_j e^{-i\mathbf{Q}\cdot\mathbf{r}_j} | \psi_{GS} \rangle|^2 \propto |\langle \psi_f | \rho(\mathbf{Q}) | \psi_{GS} \rangle|^2 \tag{2.8}$$

$$w^{(2)}_{i\to f} \propto \left| \sum_M \sum_{j,k} \frac{\langle \psi_f | e^{i\mathbf{q}_{in}\cdot\mathbf{r}_j} \boldsymbol{\epsilon}_{in}\cdot \mathbf{p}_j | \psi_M \rangle \, \langle \psi_m | e^{i\mathbf{q}_{out}\cdot\mathbf{r}_k} \boldsymbol{\epsilon}_{out}\cdot \mathbf{p}_j | \psi_{GS} \rangle}{\varepsilon_g - \varepsilon_m + \hbar\omega + i\Gamma_M} \right|^2 \tag{2.9}$$

where $\rho(\mathbf{Q})$ is the Fourier transform of the electron density operator, which in real space is defined as $\rho(\mathbf{r}) = \sum_j \delta(\mathbf{r} - \mathbf{r}_j)$. As can be seen, we have dropped a lot of terms: this is due to the requirements on creation and annihilation operators on photons. The two "channels" of scattering involve two very different physical processes. The first one does not involve any intermediate state, and its transition probability depends on the electron density. This is the so called "Thomson scattering", which is a non-resonant effect: it is responsible for Inelastic x-ray scattering and, at zero energy loss, for the normal XRD signal. The second type of transition instead involves the formation of an intermediate state $|\psi_m\rangle$, and thus of a core hole. This excited state then decays back to the ground state (at least in an elastic scattering), and a photon is re-emitted. This term is the one associated with RXS, and the reason why this technique can provide so much information about the physics of materials relies indeed on the formation of this core hole: before decaying, it can induce many collective excitations such as phonons, magnons and *dd* excitations [40]. The resonant character of these process is contained in the presence, at the denominator, of the quantity $\varepsilon_{GS} - \varepsilon_m + \hbar\omega$: when the photon frequency exactly matches an absorption edge of the material (i.e. when it matches the energy required to excite a state ψ_m), $w^{(2)}$ gets greatly enhanced (of a factor ≈ 1000) [36]. When the photon frequency is instead very far from the material resonances (i.e. $\gtrsim 100keV$), this term becomes very small (but not infinitely small, thanks to the presence of $i\Gamma$), and everything is governed by Thomson scattering. However, even at resonance, the fact that the scattering is governed by a second

order process make the cross sections inherently small: this is why RXS and RIXS need the high brilliances and photon fluxes of synchrotron facilities. Figure 2.3 shows a graphical representation of the two scattering processes.

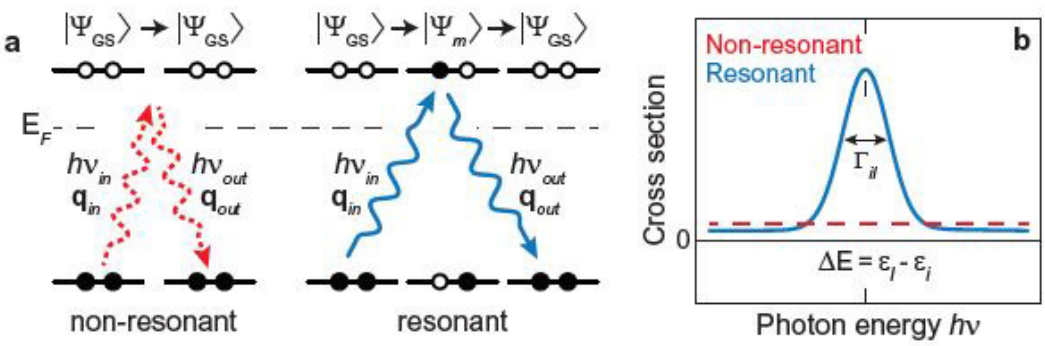

Figure 2.3: Panel (a): schematics of resonant and non-resonant scattering processes. Panel (b) shows instead the cross section for the two types of scattering. Taken from [22].

To simplify the notation, it is useful to define the dipole operator D:

$$\mathcal{D} = \frac{1}{im\omega_{\mathbf{q}}} \sum_j e^{i\mathbf{q}\cdot\mathbf{r}_n} \epsilon \cdot \mathbf{p} = \boldsymbol{\epsilon} \cdot \mathbf{D} \tag{2.10}$$

This name will be justified shortly. To obtain the effective cross section, differential in both energy and momentum, we have to sum over the all possible compatible final states, divide for the incident flux and multiply for the density of photon states in a solid angle $d\Omega$ $(= \mathcal{V}|\mathbf{q}'|/2\pi^3)$. The final RIXS cross section is [40]:

$$I(\omega, \mathbf{q}, \mathbf{q}', \epsilon, \epsilon') \propto \omega_{\mathbf{q}'}^3 \omega_{\mathbf{q}} \sum_f |\mathcal{F}_{f,GS}(\mathbf{q}, \mathbf{q}', \epsilon, \epsilon', \omega_{\mathbf{q}}, \omega_{\mathbf{q}})|^2 \tag{2.11}$$

$$\times\, \delta(\varepsilon_{GS} - \varepsilon_f + \hbar\omega) \tag{2.12}$$

with

$$\mathcal{F}_{fg} = \sum_m \frac{\langle\psi_f|\mathcal{D}'^{\dagger}|\psi_m\rangle \; \langle\psi_m|\mathcal{D}|\psi_g\rangle}{\varepsilon_g - \varepsilon_m + \hbar\omega_{\mathbf{q}} + i\Gamma_m} \tag{2.13}$$

where we have introduced $\mathcal{F}_{fg}$, the scattering amplitude. While this holds for RIXS, for REXS we cannot resolve all these information. To obtain the REXS signal, it is then necessary to integrate in energy and to sum for the possible outgoing polarizations. The energy range measured by REXS is determined by the slits put before the detector, which filter the energies more than ≈ 20 eV beyond the elastic signal.
This equation is also closely connected to the XAS signal, which can be shown to be:

$$I_{\mathrm{XAS}}(\epsilon, \omega_{\mathbf{q}}) \propto \mathrm{Im}[\mathcal{F}_{gg}(\epsilon, \epsilon, \omega_{\mathbf{q}})] \tag{2.14}$$

Since we are dealing with REXS, and thus we are mainly interested in the elastic part of the signal, we can set $|\psi_f\rangle = |\psi_g\rangle$. Moreover, formula 2.9 can be further simplified assuming that the x-ray excitation is local, in the sense that the hole

excited is strictly localized on one atomic orbital: this means that the absorption process produces just a single electron transition from one orbital to another. This allows to make three approximations:

- $\psi_m \approx \chi_l^{(n)}(\mathbf{r} - \mathbf{R}_n)$, where the latter is an electron wavefunction localized at site $\mathbf{R}_n$;
- All the scalar products $\left\langle \chi_i^{(n)} \middle| \mathbf{p} \middle| \chi_l^{(m)} \right\rangle$ are zero $\bigvee i, l$ whenever $m \neq n$ (i.e. electrons are localized on two different lattice sites);
- the phase factor in eq. 2.9 is approximated by $\exp(i\mathbf{q}_{in,out} \cdot \mathbf{R}_n)$: that means neglecting phase variations of the incoming photons over the size of the electron wavefunction. This is called the *dipole limit*.

Using this definition, we are left with the so called *form factor* f_{pq}, where p and q indices denote x,y and z components:

$$f_{pq} = \sum_{i,l} \frac{\langle \chi_i^{(n)} | p_q | \chi_l^{(n)} \rangle \cdot \langle \chi_l^{(n)} | p_q | \chi_i^{(n)} \rangle}{\hbar\omega - (\varepsilon_l^(n) - \varepsilon_i^(n)) + i\Gamma_{il}} \tag{2.15}$$

which is a tensor depending on photon energy and lattice site, but neither on $\mathbf{Q}$ nor on the polarization. Using this definition, RXS cross section becomes:

$$I(\mathbf{Q}, \hbar\omega_{\mathbf{Q}}) \propto \left| \sum_{p,q} (\epsilon_{in})_p \left[\sum_n f_{pq}^{(n)} e^{i\mathbf{Q}\cdot\mathbf{R}_n} \right] \cdot (\epsilon_{out})_q \right|^2 \tag{2.16}$$

$$= \left| \sum_{pq} (\epsilon_{in})_p \cdot F_{pq} \cdot (\epsilon_{out})_q \right|^2 \tag{2.17}$$

where the scattering tensor $F_{pq}(\omega_q)$ is no more a local quantity since is a sum over different lattice positions. Again, in RXS (as opposed to RIXS) experiments no information is acquired on the energy or polarization of the scattered light, and so the total intensity should be integrated over $\partial\omega_{\mathbf{q}'}$ and summed over the polarizations. This last formula is useful when dealing with the insulating parent compounds or localized excitations such as *dd* excitations, because it avoids working with many-body wavefunctions and methods.

2.2.1 The experimental scheme

Before describing in detail the structure of Bessy UE46-PGM1 beamline which has been used for our experiments, we will briefly outline which is the general experimental geometry used in RXS experiments (both RIXS and REXS), limiting ourselves to the reflection configuration. Figure 2.4 shows some schematics of what will be explained here. The sample is usually placed on a mobile holder as depicted in figure 2.4. We have called a,b and c the three real-space orthogonal basis of an orthorhombic system (like YBCO and other cuprates), where a and b are directed along Cu-O bonds. We will assume now that c is lying on the scattering plane perpendicular to sample surface, since it is the case in most of the experiments (but not in the one outlined in chapter 4, for example). The x-ray beam will impinge

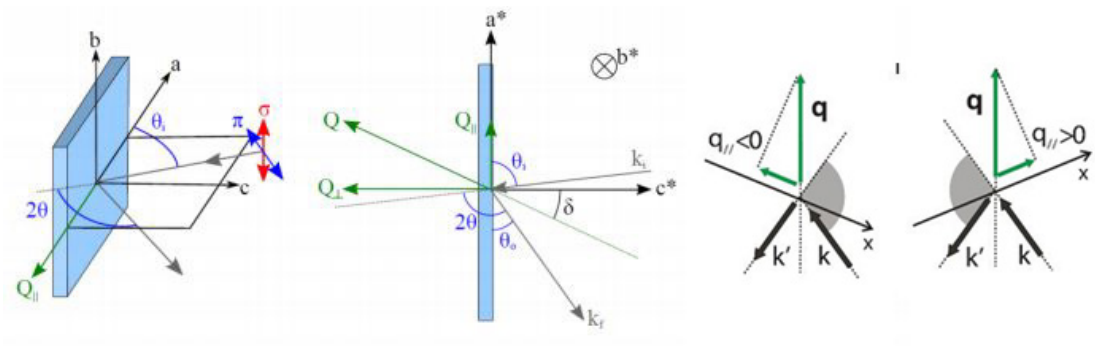

Figure 2.4: Scheme of the experimental geometry used in RXS for a generic orthorombic material. Also shown is the incoming polarization of photons. Right panel shows the convention for positive and negative $Q_{\|}$. Readapted from [25] and [41].

on the sample with energy $\hbar\omega$ and momentum $\mathbf{q}$, with $|\mathbf{q}| = 2\pi/\lambda$, and will be scattered in $\mathbf{q}'$, $\hbar\omega'$ (although the information on the energy of the outgoing beam is lost in REXS). The momentum transferred to the material is called $\mathbf{Q} = \mathbf{q} - \mathbf{q}'$. The two principal angles of the experiment are called (with a little abuse of notation) θ and 2θ: the former is the angle formed by the surface of the sample and the x-ray beam (along the positive direction), while the latter is the angle formed by the direction of the incident beam and the scattered one. In general, motors mounted on the holder allow to change the orientation of the sample by rotating the θ, χ and ϕ angle, all shown in the figure (in Bessy beamline no motor for χ exists, however, and ϕ can only be moved by hand). Another quantity which is often used when calculating the components of transferred momentum is δ, which is defined as the angle between the transferred momentum $\mathbf{Q}$ and the line perpendicular to sample surface (the c-axis, in the figure): $\delta = \theta - 2\theta/2$ (where of course $2 \cdot \theta \neq 2\theta$, except for specular reflections). Through all these angles, it is possible to express the components of the transferred momentum along the reciprocal axis of the sample (i.e. the Miller indices (H,K,L) of $\mathbf{Q}$). We will assume an orthorhombic unit cell and $\phi = 0$:

$$|\mathbf{Q}| = 2|\mathbf{q}_{in}| \sin(2\theta/2) \tag{2.18}$$

$$H = (|\mathbf{Q}|/a^*) \sin(\delta) \tag{2.19}$$

$$K = (|\mathbf{Q}|/b^*) \cos(\delta) \sin(\chi) \tag{2.20}$$

$$L = (|\mathbf{Q}|/c^*) \cos(\delta) \cos(\chi) \tag{2.21}$$

From these formulas it is evident that the maximum $\mathbf{Q}$ that can be given to the sample is fixed by 2θ, while θ, ϕ and χ control the projections of it along the material axes. Moreover, as it is obvious in reflection geometry, L can never be made equal to zero, but can be reduced rotating angle χ to almost 90°: this will become useful in chapter 4. While positive and negative direction of the in-plane directions are equivalent in the material, spectra measured along H and $-H$ are not: this is because the geometries used to reach positive and negative values are different. The usual convention is to assign positive H values to almost normal-in grazing-out configuration, and negative values to the grazing-in normal-out one

(both shown in figure 2.4).

2.3 UE46-PGM1 at Bessy II

We will now dedicate a section to the UE46-PGM1 beamline, which has been used for the two experiments analysed in this Thesis. We will briefly summarize how x-ray beams are produced in a synchrotron facility, and then we will explain how the beamline works with the help of some important figures.

2.3.1 Synchrotron radiation and Bessy II

As we said before, the advent of synchrotron radiation facilities greatly enhanced the possibility of experimental techniques. With respect to conventional x-ray sources like tubes and Compton sources, synchrotrons can provide much higher brilliance (up to a factor of 10^9) and monochromaticity, smaller spot size and naturally defined polarization.

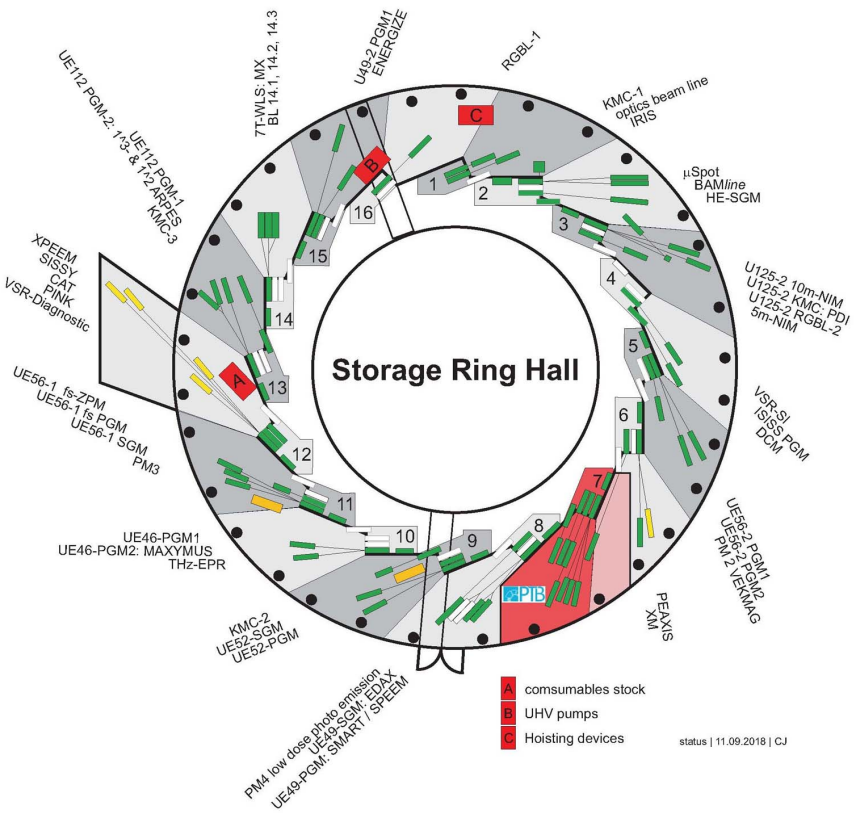

Figure 2.5: Scheme of the top view of Bessy II. LINAC and Microtron are located inside the inner circle and are not shown here. Taken from [42].

A synchrotron is basically a large ring in which electron bunches are accelerated to produce EM radiation. Initially, electrons are produced and accelerated with an electron gun in a Linac (linear accelerator); then they enter a small ring called *microtron*, where they are further accelerated to a nominal E value. Finally, they

are injected in the main ring, which in the case of Bessy has a circumference of approximately 240 m. Here, they are kept at constant speed by means of radio-frequency cavities, which provide the necessary acceleration through strong electric fields. Moreover, fields are oscillating in time at a known frequency, and thus the resulting electron bunches are synchronized. In Bessy II, about ~ 400 different bunches travel simultaneously, separated by a distance of 2 ns. Their curved trajectory along the ring is imposed by the use of very strong electromagnets, which change their direction thanks to the Lorentz force and also keep the beam focused. These magnets alternate with straight sections where *insertion devices* like *wigglers* and *undulators* are placed: these are the devices used to effectively produce radiation for all the different beamlines. Bessy II has a total of 32 deflecting magnets and 16 straight region, 14 of them being equipped with insertion devices. All in all, Bessy II has 46 different beamlines and can produce x-rays with energies ranging from the soft regime (< 1 keV) up to 150 keV.
To minimize the decay rate of the current inside the main ring due to collisions between electrons and other atoms, everything is kept in Ultra-HIgh Vacuum. In Bessy II, electrons in the main ring have a 1.7 GeV energy and create a ring current of approximately 250 mA. Unlike other synchrotron facilities like ESRF, Bessy II works in top-up mode: this means that new electrons are periodically (more or less every 10 minutes) injected in the main ring to mantain the current as constant as possible. While this allows to directly compare measures taken at different times without the need for complex normalizations, the injection produces a peak in photon flux: as a result, periodic spikes are observed in the measurements.

2.3.2 Undulator UE46

The core of soft x-ray beamlines are the so called *undulators*. They are composed by an array of magnets with alternating direction of magnetic field, which forces the particles into a sinusoidal trajectory transverse to longitudinal axis. The acceleration imposed on the electrons results in the emission of radiation tangent to their trajectory (and thus to the storage ring). The undulator of UE46-PGM1 beamline is called UE46 and is shown in figure 2.6. In the frame moving with the beam, the oscillating electron is equivalent to a dipole, and thus the emitted wavelength will be given by the period of the magnets. This is usually in the order of 10 mm: relativistic contraction of distances and Doppler effect then make sure that the measured wavelength is reduced by a factor $\approx 2\gamma^2$, where γ is the Lorentz factor; for example, the UE46 undulator has a period of 46.3 mm. Moreover, wavelengths can be finely adjusted by slightly varying the distance between the magnets (the gap, in the order of some cm too), which in turn modifies the magnitude of the magnetic field acting on the electrons. UE46 can produce energies between 120 and 2000 eV, in the soft x-ray regime. This range is enhanced by the fact that also odd harmonics of the chosen frequency are produced: for example, the Cu L3 edge (≈ 930 eV) is reached with a third harmonic [44]. A special design of the undulator, called APPLE II, can also produce light with precise polarization, linear or circular. This is obtained by using two different groups of magnets arranged in four rows (as depicted in figure 2.6). Two opposite rows can be moved simultaneously, and this changes the phase between the two components of the magnetic fields. This

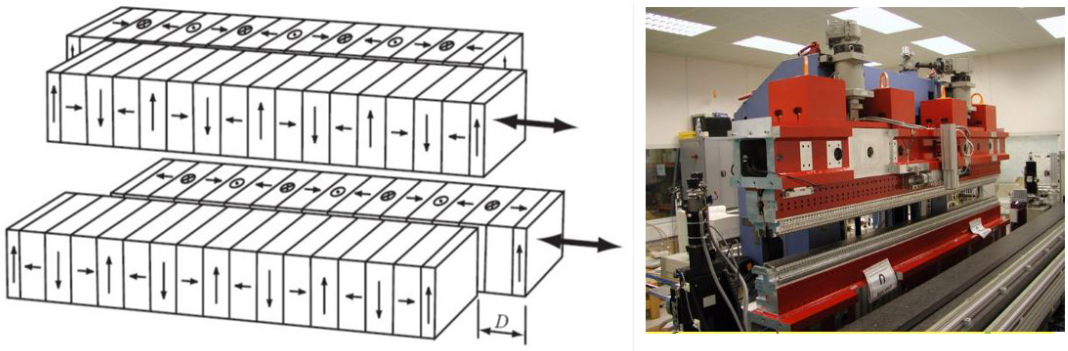

Figure 2.6: Left panel shows a scheme of an APPLE II undulator. Arrows indicate the direction of polarization of permanent magnets. Right panel is a photograph of UE46 undulator at Bessy II. Taken from [43] and [42].

forces an elliptical motion of the electrons, and thus this type of undulator is called "elliptical". UE46 is indeed an APPLE-II undulator. The energy resolution of these devices is determined by the number of periods and it is possible to show [45] that it roughly corresponds to $\Delta E/E = 1/nN$, where N is the number of periods and n is the harmonic. UE46 has $N = 70$, and thus we can estimate $\Delta E \approx 4$ eV at the Copper L3 edge (since we use the third harmonics to reach 930 eV in vertical polarization).
The light emitted by an undulator is not collimated, but has a certain degree of divergence. Relativistic mechanics show that light emitted by an accelerating particle moving (instantaneously) at velocity v, is confined to a cone with small angular aperture $\Delta\theta = O(1/\gamma)$. Since at $E = 1.7$ GeV we have $\gamma \approx 3200$, the angular aperture is very narrow: this is the main reason for the high brilliance of synchrotron sources.

2.3.3 Beamline optics

UE46-PGM1 is one of the two beamlines served by the UE46 undulator. It is specialized in REXS, XAS and XMCD (X-ray Magnetic Circular Dichroism) measurements in the soft x-ray regime and it has been used in dozens of scientific articles, some of them cited in this thesis [16, 25, 29, 32, 46]. The information about the beamline has been taken from [42, 44]. It has a total length of ≈ 31 m, which is quite small compared to other RXS and RIXS beamlines (as an example, ID32 beamline at the ESRF is 120 m long). Correspondingly, its design is quite simple and a scheme is presented in figure 2.7. The core of the optical setup is a Plane-Grating Monochromator (PGM). This is a necessary step, since the light coming out from the undulator has an non-negligible spread in energy (see section above). Plane gratings for soft x-rays are very complex objects, whose quality is quite critical for the good working of the entire beamline: they represent the only alternative to Bragg crystals, which can be used only for hard x-rays. A diffraction grating is basically composed by a huge number of equally spaced lines realized through optical lithography. In the soft x-ray regime, there are usually between 800 and 1200

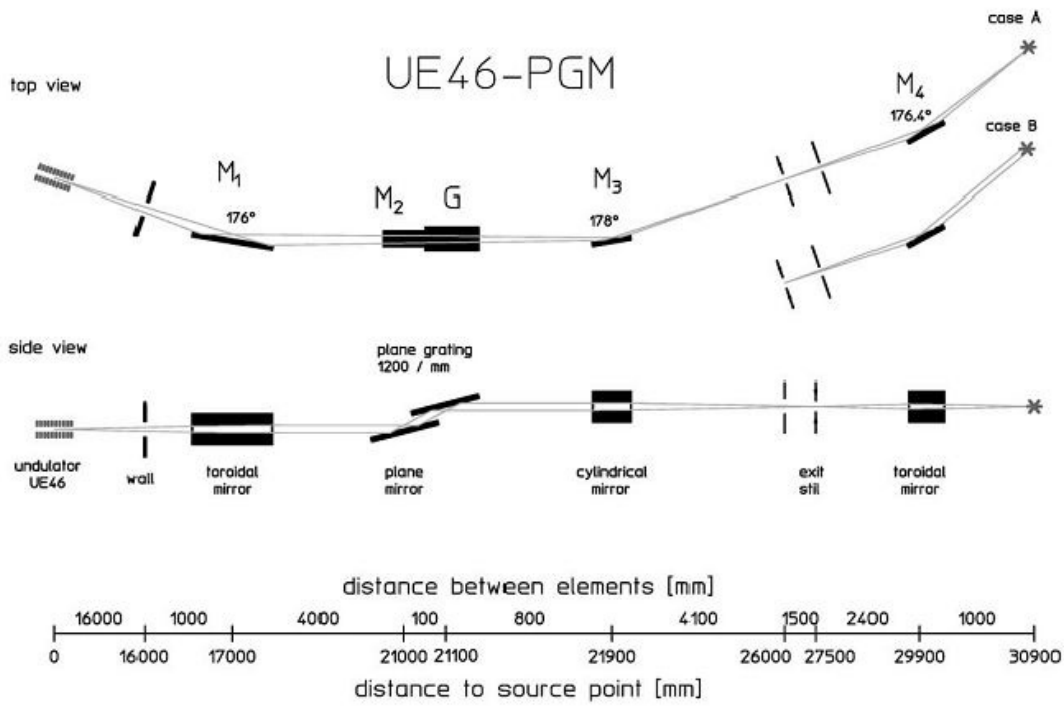

Figure 2.7: Scheme of the UE46-PGM1 beamline in Bessy II.

lines/mm, with a spacing $d \approx 833$ nm. Because of interference, incident radiation will be spatially separated in its spectral component: in particular, incident light with wavelength λ, forming an angle α with the grating's surface will be scattered at an exit angle β (again with respect to grating surface) having:

$$\cos(\beta) = \cos(\alpha) - \frac{n\lambda}{d} \tag{2.22}$$

where d is the spacing between lines and n is the diffraction order. To select the proper spectral range, an exit slit is put after the monochromator, effectively filtering out all non-required wavelengths. Before the grating, a toroidal mirror and a plane one are used to collimate the beam right after the undulator. This step is useful for two reasons: first, because it allows to change independently the angle α and β of the grating (i.e. angles formed by the grating's surface with the ingoing and outgoing beam, respectively). Secondly, because it allows to use a fixed slit (used to select the resolution) after the monochromator [47]. Indeed, in a diffraction grating using divergent light the real and virtual positions of the source satisfy the relation:

$$r' = -r \cdot \frac{\cos^2 \beta}{\cos^2 \alpha} \tag{2.23}$$

where r and r' are the distances between the grating and the real/virtual monochromatic source, respectively. This means that, when changing the incoming photon energy, the virtual position of the monochromatic source will change and thus the spot size at the exit slit. This is a big issue, because it requires a moving slit to select the proper spectral range at all energies. A collimated beam, however, remains so even after the PGM and thus a simple mirror is needed to focus it onto the exit

slit, which can now stay fixed. Moreover, as can be seen, all the incidence angles are grazing to maximize the reflectivity. The maximum resolution achievable is 10000, which means that the beam impinging on the sample has a minimum energy range of approximately $\approx$ 100 meV. Of course, a clear trade-off exists between transmitted photon flux and resolution: the more one shrinks the passband, the more the beam will be attenuated. A final toroidal mirror focuses the beam onto the sample: the spot size is usually 100 μm x 50 μm, which can be shrunk down to 40 μm x 10 μm adjusting the slits and mirrors. All in all, UE46-PGM1 beamline is able to provide a photon flux of approximately 10^{12} photons/second in the energy range covered by the undulator.

2.3.4 XUV diffractometer

The XUV diffractometer is one of the two endstations attached to the PGM1 beamline: the other is instead a high field diffractometer, which is used to measure RXS and XAS in high magnetic (fields up to 7 T). Since we have not used it in our experiments, we will concentrate just on the XUV diffractometer. This is a

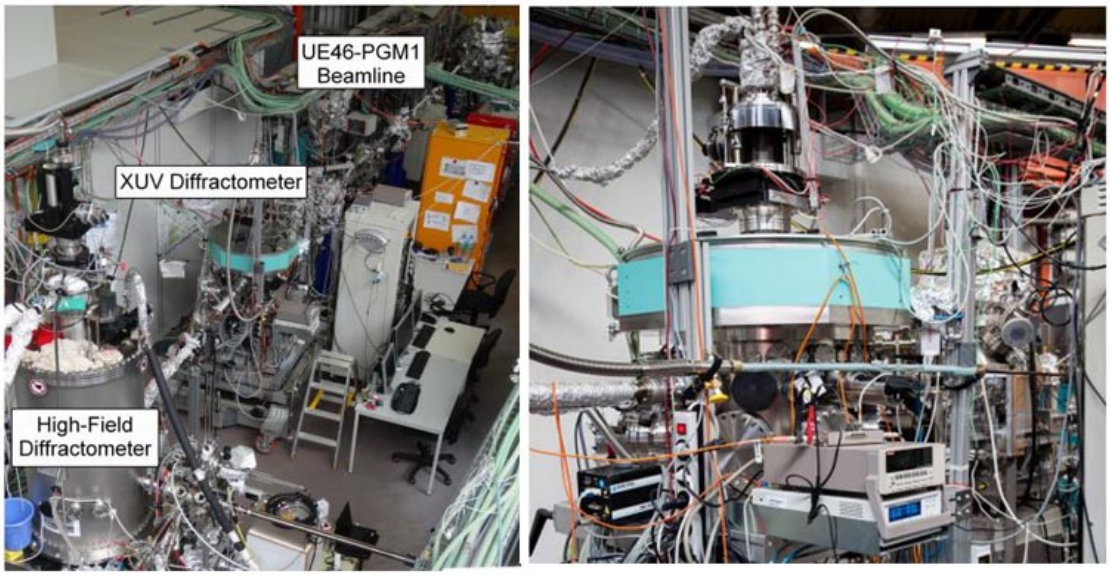

Figure 2.8: Left: PGM1 beamline with its two endstations (XUVr and high-field diffractometers). Right: close up of the two-circle XUV diffractometer which has been used in our experiments. The sample holder is located in the middle of the detector disk. Both the elements can move independently. Figure taken from [42].

standard two-circles diffractometer, meaning that detector and sample are mounted on two disks which can be moved independently. The sample holder has 4 motors controlling x,y, and z position in real space as well as θ, the angle between the sample surface and the beam. The external disk (shown in figure 2.8), on which the detector is mounted, can then rotate around its axis to change the value of 2θ. The rotation angle is unlimited, meaning that the diffractometer can rotate of 360°. Differently from other beamlines, there is no motor controlling χ, and the fine alignment of the sample is obtained equivalently by moving the detector

in z direction (the one perpendicular to the scattering plane). Moreover, angle ϕ has to be moved manually *in situ*. In order to perform measurements at low temperature, the sample holder inside the diffractometer is directly attached to the liquid-He-flow cryostat: this allows to obtain temperatures down to 4 K. Since in REXS no additional monochromator is used to resolve the spectra of the scattered beam, no other optics is required before the detector. This is, in particular, a silicon photodiode (AXUV100-type). It is placed behind a set of changeable slits which can be used to adjust the energy resolution.

Chapter 3

CDW in nanopatterned YBCO structures

This chapter describes the experimental results taken at Bessy II in January 2019, during the experiment 182-07152 performed at the beamline UE46_PGM-1. The main goal of these experiments was to investigate how spatial confinement affects the charge order signal in intensity and width. In the following, we outline the analysis of these data and we compare the results with some numerical simulations performed on Matlab.

3.1 Motivation of the experiment

As already outlined in the first chapter, the effective relation between the CDW instability and the superconducting state remains still a partially open question. It is indeed still unclear whether charge order is a dynamical process intertwined with HTS, or simply an epiphenomenon which arises on top of a fundamental non-Fermi-Liquid behaviour building below p^*, the doping at which the pseudogap crossover temperature vanishes [39]. Over the years, new experiments have thus been designed to understand how these two phases of matter are affected when some conditions are altered. The main idea of the experiment was to study how superconducting and charge order state are affected when the dimensions of a cuprate material are shrunk to micrometric and nanometric size. Although some experiments on ultra-thin c-axis oriented YBCO films have already been carried out ([22]) once more showing that usual charge order is a purely 2D instability of Cu2 planes), confinement in a-b planes is potentially much more interesting and challenging to study. As known from dozens of previous experiments [22, 25], charge density waves have a correlation length of more or less 10 nm, which is just some dozens of lattice parameters. It would then seem reasonable to think that any confinement effect on the intensity of this signal would arise in nanostructures with a dimension comparable to this length scale. However, an experiment on Hg1201 [1] and some unpublished results of the group of Prof. Floriana Lomabrdi at Chalmers, in collaboration with Prof. Ghiringhelli and Prof. Braicovich [27] seem to challenge this conclusion.

In the paper of Bianconi et al. [1], authors have used different XRD techniques on

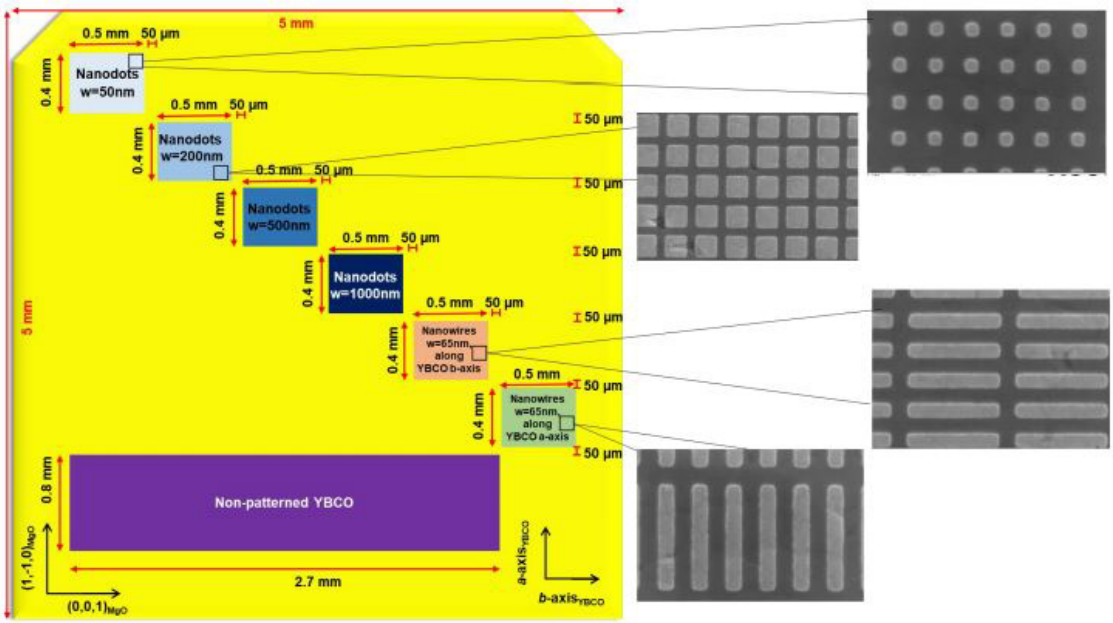

Figure 3.1: A scheme of the slabs from 1 to 10 used during the experiments, with a 50 nm Au cap layers to protect the dots. Slabs 11-14 were similar, but with a thinner Au cap layer of 30 nm and structures underdeveloped by 50 nm (and thus no 50 nm dots). Adapted from the experiment proposal to Bessy II.

$HgBa_2CuO_{4+y}$ to measure both the charge order signal and the spatial distributions of Oxygen defects (i.e. Oxygen interstitials which aggregate into stripes). They found that the two signals are spatially anticorrelated; moreover, since oxygen defect distribution is not completely random, but has a mesoscopic correlation, this could imply that also charge order feels effects whose length is in the mesoscopic range.

The unpublished results mentioned before regard an experiment performed at ESRF in May 2017, which is presented in [27]. There, nanodots with sizes ranging from 200x200 μm^2 to 50x50 μm^2 as well as elongated nanostripes were probed with RIXS to search for possible CDW presence. During the experiment, no sign of a dispersive signature around (0.31, 0, L) was found, not even in the dots whose lateral dimensions were still about $\approx$ 20 times the maximum CDW correlation length. On the contrary, a CDW signal with the same characteristics as the bulk was found in structures whose dimension was in the micrometer-scale. This result called for further investigation, and the experiment described in this chapter is the logical continuation.

3.2 Samples and experiment

3.2.1 Samples

The core of the experiment is given by YBCO samples patterned with nanostructures with various sizes and doping. An usual problem, when working with

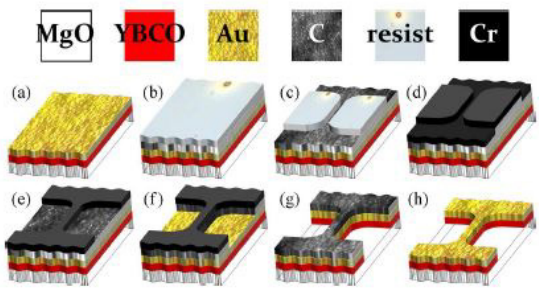

Figure 3.2: Brief description of the nanopatterning process used by Chalmers' group to grow the samples (in this case, the patterning of a nanowire is shown, but the steps are exactly the same as for our case). (a) Au/YBCO bilayer is grown on the substrate, (b) a carbon layer acting as a hard mask is evaporated and then a double layer resist is spun, (c) the resist is developed after the e-beam lithography, (d) a chromium layer is evaporated on top, (e) the mask is defined after Cr is lifted-off, (f) uncovered C is removed by oxygen plasma etching, (g) chip after ion-beam etching, (h) the nanowires are achieved after oxygen plasma removal of the residual C. Taken from [51].

cuprate nanostructures is, however, that they usually degrade their superconductive properties because of the etching process [48–50]. This experiment was instead made possible by the samples prepared by the group of Prof. Floriana Lombardi at Chalmers University. The way this unique samples have been prepared is presented in [51, 52], and described in figure 3.2. In particular, a 50 nm YBCO film is deposited onto the substrate through a standard PLD technique and immediately covered with an Au capping to prevent oxygen outdiffusion, which otherwise would be very severe during several steps of the nanopatternign procedure (i.e. baking of the resist, Ar+ and oxygen etching). After that, the nanodots are shaped using a combination of Electron Beam Lithography and Ar^+ ion milling, with the use of a 100 nm thick amorphous carbon hard mask. Since the interaction between YBCO and the ions can modify the stoichiometry of the material and severely affect transport properties, this last step is made as "gently" as possible, using an acceleration voltage close to the threshold of 300 V, below which no etching is obtained [53]. Finally, to assess the quality of the nanostructures, transport measurements are carried out [51, 54]. First, the resistance vs T measurements reveal that the T_c is equal to the one of the bulk. Secondly, the critical current, determined via Current-Voltage characteristics, is very close to the depairing limit, i.e. the maximum critical current which can be carried by YBCO according to the theory. The efficiency of this patterning procedure in preserving pristine properties, representative of the material when is shrunk to the nanoscale, has been demonstrated over last years in different types of nanostructures, as in nanowires [55–57] and nanorings [58], and on different cuprate materials [59].

The samples probed were similar to the one used in the previous ESRF experiment ([27]). We had two different groups of slabs, which had a 50 nm and 30 nm Au capping layers respectively. For each group, we had samples with different dopings: since we were expecting a weak signal, only UD YBCO structures were prepared

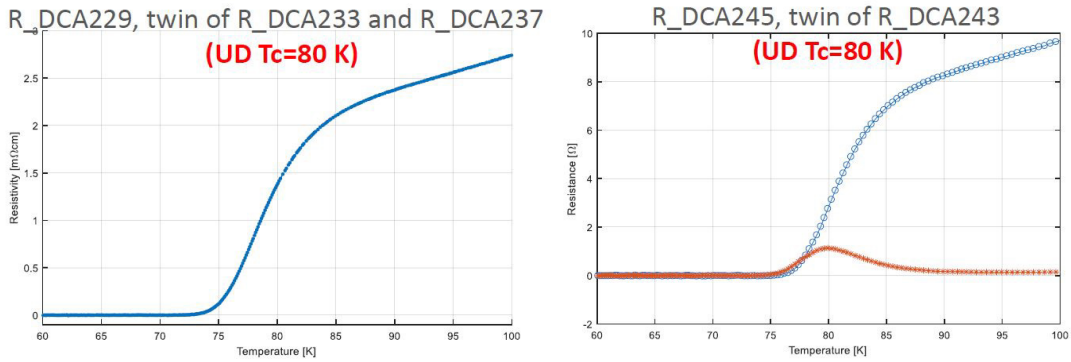

(a) (b)

Figure 3.3: R(T) curves for samples DCA237 and DCA243 (3.1). As can be seen, superconducting transition is quite sharp, with a $T_c \approx 80$ K in both samples. The red curve of figure (b) is the derivative of the resistance and its maximum is taken to be T_c.

(discarding OP ones), with doping p close to 0.125 and T_c between 60 K and 80 K. All the samples probed had $SrTiO_3$ substrates, which produce twinned films. Each slab contained a non - patterned region (used as a reference) and islands of nanostructures with different size: dots with 50, 200, 500 and 1000 nm size and nanostripes elongated in one direction which were not probed also due to short time schedule. The thickness of all the nanostructures was 50 nm. Also, the distance between the nanostructures was kept constant and equal to 100 nm. The batch with 30 nm Au cap layer was however a bit underdeveloped due to not-optimized EBL doses, and had nanostructures whose sides were shorter by 50 nm (and consequently the 50 nm dots disappeared). As described above, the quality of these structures is assessed through R(T) and J_c measurements, which were carried out on twin samples: the R(T) is shown in figure 3.3. The scheme of a slab is presented in figure 3.1, and a summarizing table is shown right here:

Sample	T_c [K]	Nanostruct. probed [nm]	Au thick. [nm]	Notes
DCA237	80	1000, 500, 200	50	-
DCA243	80	950, 450, 150	30	Non optimized EBL dose

Table 3.1: Summary of samples used in this experiment.

The fact that the distance between nanostructures is kept constant means that the filling factor of the islands, defined as the ratio between the area occupied by dots of the same size and the total area of the island, diminishes as the lateral dimension of the dots reduces. In particular, a straightforward derivation shows that:

$$FF = \frac{A_{dots}}{A_{island}} = \frac{l^2}{(l+b)^2} \tag{3.1}$$

where l is the size of the dots, b is the distance between them, A_{dots} is the total area of the YBCO structures of the same size, and A_{island} is the total surface covered by those structures, comprising also the exposed substrate (i.e. the coloured rectangles in figure 3.1). Since the intensity of CDW signal obviously depends on the fill factor, it is fundamental to estimate it for all the different structures. The results are shown in the following table:

Sample	Dot size [nm]	b	FF
DCA237	1000	100	0.8264
DCA237	500	100	0.6944
DCA237	200	100	0.4444
DCA243	950	150	0.7459
DCA243	450	150	0.5625
DCA243	150	150	0.25

Table 3.2: Filling factors for the structures probed in the experiment, calculated used formula (3.1).

3.2.2 Experimental details

This time, session was carried out at the beamline EU46 in Bessy II, Berlin. While REXS technique has surely some disadvantages with respect to RIXS, the main one being that it's impossible to distinguish between elastic (which is the interesting part in this experiment) and inelastic contribution to the signal, there are also some advantages. The biggest one is that scans are much faster, and this allows to take more points in q-scans as well as to investigate more samples, temperatures and incoming photon energies. Since we only had time to probe films over STO substrates, all the scans have been acquired along H direction in reciprocal space, since in twinned films a and b directions are equivalent. The chosen L point was 1.45, away from Bragg reflections, and the corresponding 2θ was 166°. Since "normal" charge order is a purely 2D phenomenon, θ scans rather than H scans were chosen in order to save time (H scans require motion also of the motor controlling 2θ). During the experiment, also scans along (H, H) direction were acquired to establish the presence of Charge Density Fluctuations: UE46 Beamline doesn't have a motor for angle ϕ, so a manual control was the only option. This was however not problematic or risky, since any direction far from peaks in $(0.31, 0)$ and $(0, 0.31)$ is in principle good (at least approximately).

3.3 Data Analysis for Narrow Peak

First part of the experiment was dedicated to follow the behaviour of the Narrow Peak (proper Charge Density Waves) with the shrinking of lateral dimension of CuO_2 planes. Samples used were DCA237 and DCA243: both were Under Doped 50-nm-thick YBCO nanopatterned structures over STO substrates, with $T_c = 80K$

and a doping $p \approx 0.125$ (table 3.1). The only difference between the two was the thickness of the Au capping, which was 50 nm for DCA237 and 30 nm for DCA243. Also, as said before, structures in the latter were underdeveloped by 50 nm and thus effective dimensions of dots were 950 x 950, 450 x 450 and 150 x 150 nm^2 (with no 50x50 nm^2). For each "island", wide and dense scans along H were acquired (with more or less 90 point between $H = 0.2$ and $H = 0.4$ $r.l.u.$) at both low (60K) and high temperature (180K), of course after careful re-alignment of the sample after each heating.

Since the results obtained for the two slabs are different, we present them separately, starting with DCA237 (50-nm Au cap). Since REXS integrates signal coming from all types of excitations, each scan at low temperature is made up by several contributions and will not be a simple peak on a flat background. To isolate the effect coming from charge order, two ways are possible. The first one is to simply fit a low - T scan with the sum of a nth order polynomial, used to approximate the background, and a lorentzian function centred around $H = 0.31$ $r.l.u.$, which is the relevant information. This method is surely fast but lacks physical meaning, since the background is arbitrarily fitted by a smooth function: it is usually meaningful only when the relative intensity of the peak is big and the shape of the background is not too complex. The other way is to use a scan at high temperature, where charge order is no more present, as a reference: since the maximum CDW onset temperature is more or less $T = 160$ K at the doping of $p \approx 0.125$ [22, p. 22], a safe value of 180 K was chosen. This scan must then be subtracted to the one at low temperature: ideally, the only remaining contribution should be the lorentzian peak of charge order. However, to problems could remain:

- The two scans differ by a certain constant. This happen more or less always, but it can be easily solved by vertically translating them to make the "tails" far from the peak match (This means just adding a constant value to one of them before taking the subtraction). This is equivalent to adding a constant to the lorentzian function used subsequently for the fitting.

- Sometimes (and this happened especially with the smallest nanodots, due to some problems described later) the shape of the low- and high-T scans away from the peak is not the same: the slope at high (or low) H values is different. This is a major problem for the fitting, since the subtraction will no more be a simple lorentzian function, but will have also a linear (or even quadratic) contribution.

The way we have solved this problem has been re-scaling the high-T scans using a multiplicative factor, chosen to make the curves alike at the extremes of the H interval (i.e., away from the CDW peak). In detail, the actual polynomial we have used to reproduce the background was:

$$f_{scaled} = \alpha \cdot f_0 + \beta \tag{3.2}$$

where α and β have been calculated as the number minimizing the following loss function, which is the usual Residual Squared Error used in least-square fitting:

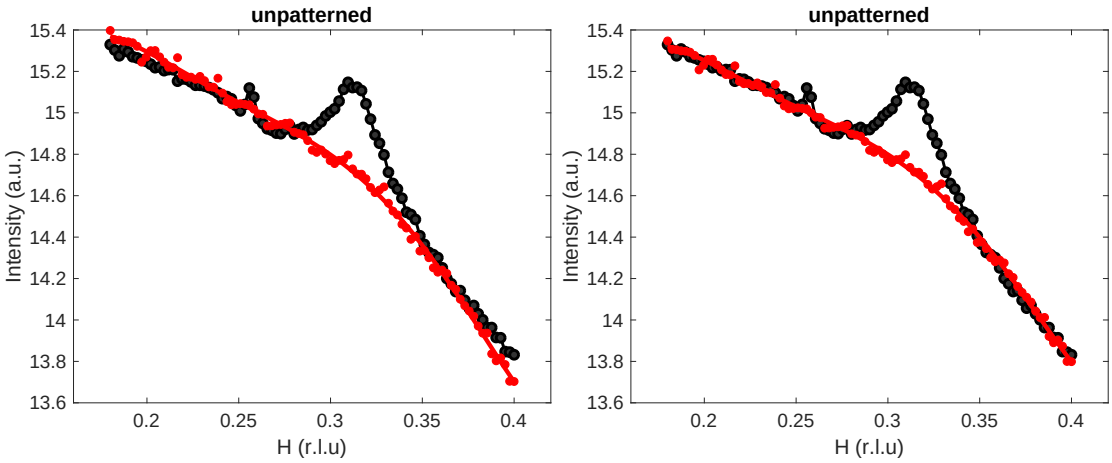

Figure 3.4: Example of re-scaling procedure used for the high-T scans (on the unpatterned region, in this case). Left figure shows a simple vertical translation of the scan: as can be seen, the slope is different at the extremes of the interval. The second one involves also a multiplication, and eliminates this difference in slope.

$$L = \frac{1}{2} \sum_{extremes} \Big(s_{60K}(h_i) - \alpha \cdot f_0(h_i) - \beta \Big)^2 \tag{3.3}$$

This "extreme" values of H have been chosen to be 0.25 $r.l.u.$ and 0.36 $r.l.u.$: this is because the expected HFHM of the Narrow Peak is around 0.15 $r.l.u.$, and thus CDW signal gives no contribution after those points. This technique has greatly helped the fittings especially for small dots: an example is shown in figure 3.4. However, it is important to notice that the "strongest" value of α used (which means, the value of α furthest from 1) was 0.92, less than 10% different from one: this is to underline that the necessary re-scaling was never too harsh.

We are now ready to present the experimental result. In order to have more statistical significance, both negative and positive H direction were explored: according to calculated cross-sections, one should expect a stronger charge-related peak in the negative part of the Brillouin Zone [25], and thus we present those scans first. Figure 3.5 shows the comparison between the scan at high and low temperature for four different structures: unpatterned region (normal YBCO film), and nanodots with sizes equal to 1000, 500 and 200 nm. The high temperature scans have been re-scaled using the procedure outlined before.

As can be seen, the shape of the background is similar for the first two structures, but changes completely for the 500 x 500 and 200 x 200 nm^2 dots. The reason for this is maybe a greater exposure of the substrate, or the fact that a greater portion of the beam probes the lateral sides of the nanostructures. The intensity of the peak clearly diminishes as the dimension of the nanostructures shrinks, and for the 200 nm dots, no CDW peak is visible. What is to be checked is whether the reduction in intensity is stronger than the reduction in the filling factor. Figure 3.6 shows the peak obtained subtracting the scans. The shape of the peak is clearly lorentzian, and no superimposed linear or quadratic behaviour is present, which means that re-scaling the high-T scans indeed worked for all the scans. For each of

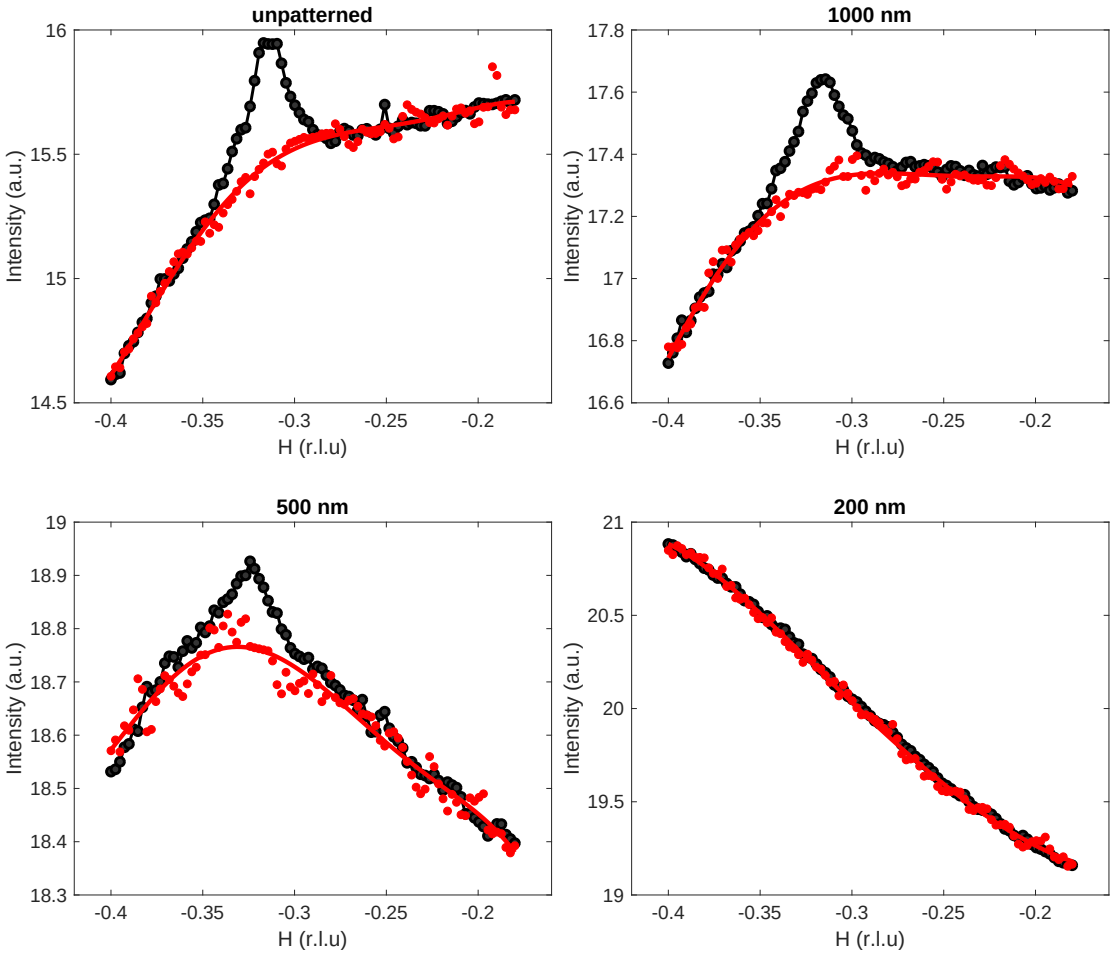

Figure 3.5: Raw scans for sample DCA237 (YBCO UD 80K, 50-nm Au cap) at negative H. Black points represent scan at low T, while red ones are the scans at high T. Solid red curve is the polynomial fitting of the background curve. High temperature scans have been re-scaled using the procedure outlined previously.

them, a lorentzian curve was fitted to extract information on the intensity, with results presented in the bottom table.

Two additional trends are here visible: peak position seems to softly shift toward higher (in absolute value) values of H and FWHM of the peak increases as the dimension of the dots decreases. The latter could possibly be associated with a reduction in the correlation length of the CDW, while it is difficult to find an explanation for the former. To determine whether this a measurement artefact or not, we repeated the same analysis on the positive part of the Brillouin Zone using exactly the same procedure. We show directly the result of the subtraction and the lorentzian parameters (3.7). Peak completely disappears when the sides of the structures narrows down to 200 nm like in the previous scans. Position slightly decreases going from the dots to the unpatterned region, but in this case no appreciable difference between 1000 nm and 500 nm structures (at least within error). Widths increases too, but the data of the 1000 nm dots has a strange bump after the peak which artificially increases the width and thus it is not reliable.

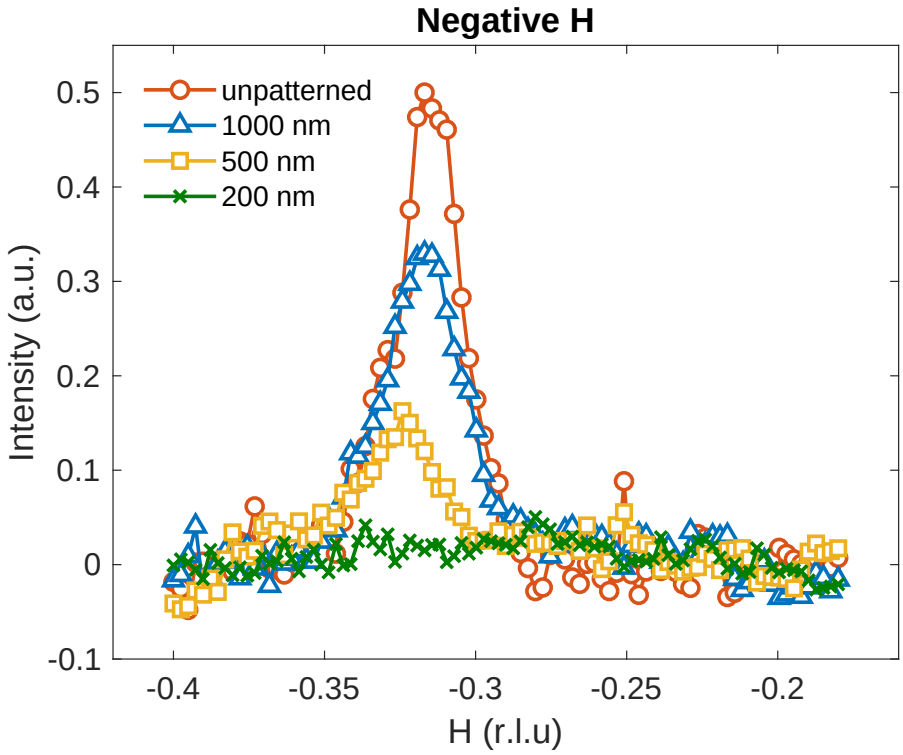

Structure	Intensity [a.u.]	q_c [r.l.u.]	FWHM [r.l.u.]	R^2
unpatterned	0.535	-0.315	0.023	0.962
1000 nm	0.353	-0.317	0.029	0.963
500 nm	0.146	-0.325	0.032	0.825
200 nm	-	-	-	-

Figure 3.6: Peak obtained subtracting high-T scan from low-T scan for the unpatterned region and the 1000, 500 and 200 nm dots (negative H). Bottom table shows parameters derived from a lorentzian fitting of the curves, along with the R^2 coefficient.

Also, overall intensity is lower than for the negative H scans as expected from cross-sections [25].

Figure 3.8a shows the evolution of the CDW peak with the lateral size of the dots, as obtained from data without any type of normalization. Before proceeding with the analysis, however, it's necessary to note that the decrease in the peak height is, at least partially, due to the change in the fill factor: since the beam spot size is constant and the distance between the dots is the same for all the islands, the effective probed area of YBCO decreases when shrinking the dimension of the structures. To account for this behaviour, intensities of the peak have been divided for the corresponding fill factors (table 3.2): the results are shown in figure 3.8b for negative H scans (but for positive H scans the result is almost identical). As can be seen, this effect alone cannot account for the observed reduction in signal: the discussion regarding the interpretation of this data is given in the next section.

Before going to the model used to interpret the data, we present the group of data acquired from the sample DCA243 (3.1), which surprisingly are a bit different

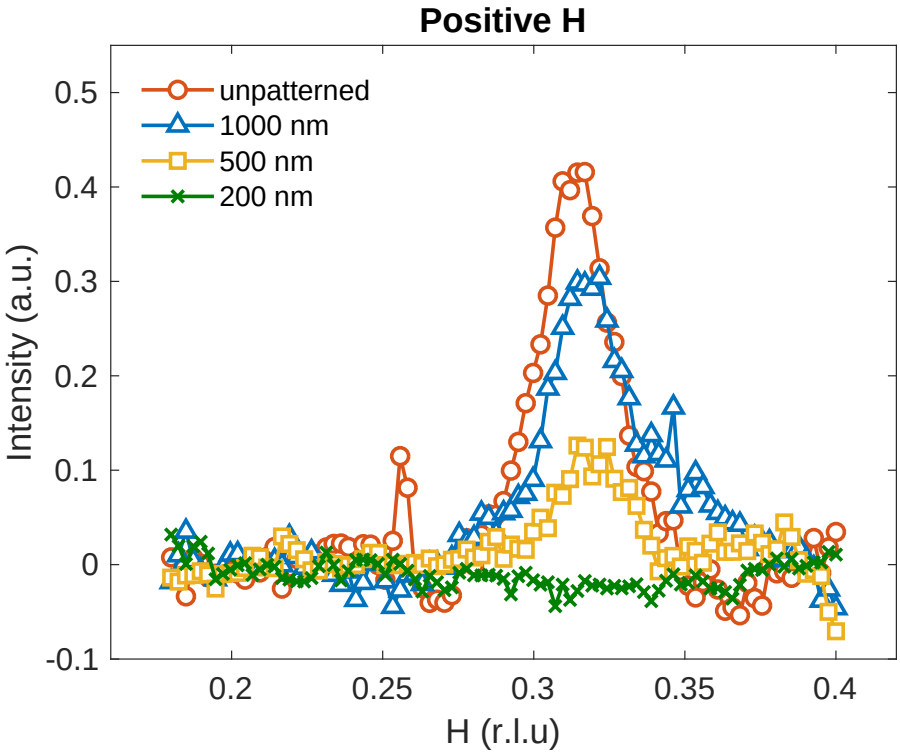

Structure	Intensity [a.u.]	q_c [r.l.u.]	FWHM [r.l.u.]	R^2
unpatterned	0.459	0.314	0.025	0.938
1000 nm	0.3142	0.319	0.034	0.933
500 nm	0.125	0.319	0.026	0.795
200 nm	-	-	-	-

Figure 3.7: Peak obtained subtracting high-T scan from low-T scan for the unpatterned region and the 1000, 500 and 200 nm dots (positive H). Bottom table shows parameters derived from a lorentzian fitting of the curves, along with the R^2 coefficient.

from the one outlined before for sample DCA237. Everything was analysed in the same way: even in this case it proved necessary to re-scale the high-T scans to match the curves at the extremes of the interval. The results of the subtraction between low- and high-T scans is shown in figure 3.9, for negative and positive H scans. Two major differences are present:

- The unpatterned region produced a weaker peak than the nanodots region, but only in the positive scans, while it is comparable to it in the negative ones.
- Now, even in the 150 nm dots a peak is detected, while before no bumps were present even in the 200 nm structures.

These are unexpected results. The fact that the CDW peak in the unpatterned region is weaker than in the 1000 (and also 500) nm structures is instead difficult to explain. A hypothesis is that the non-optimal EBL doses changed the doping of the

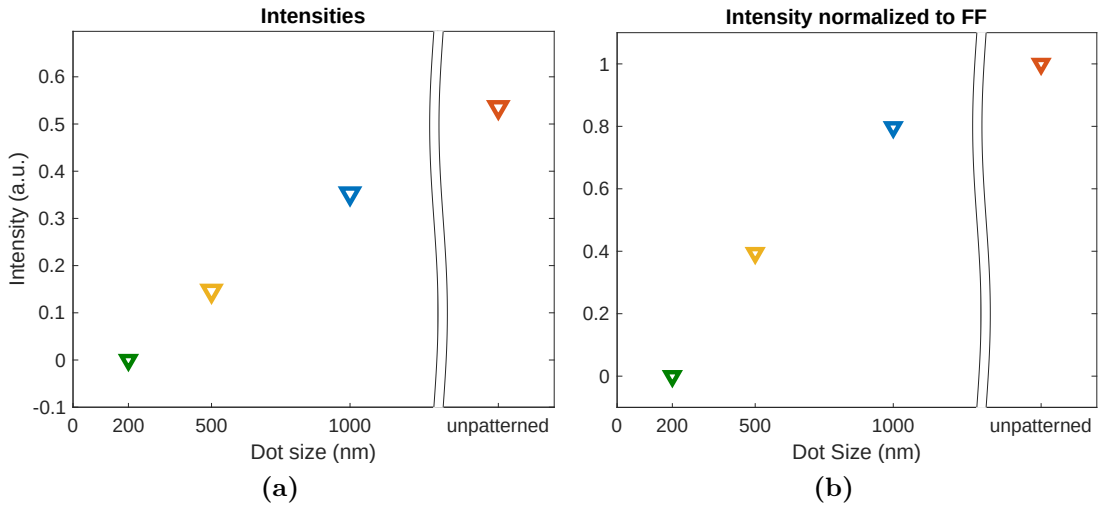

Figure 3.8: (a) Intensities obtained from dots with different sized in sample DCA237, negative H scans. (b) Intensities normalized to fill factor: as can be seen, there's still a strong reduction.

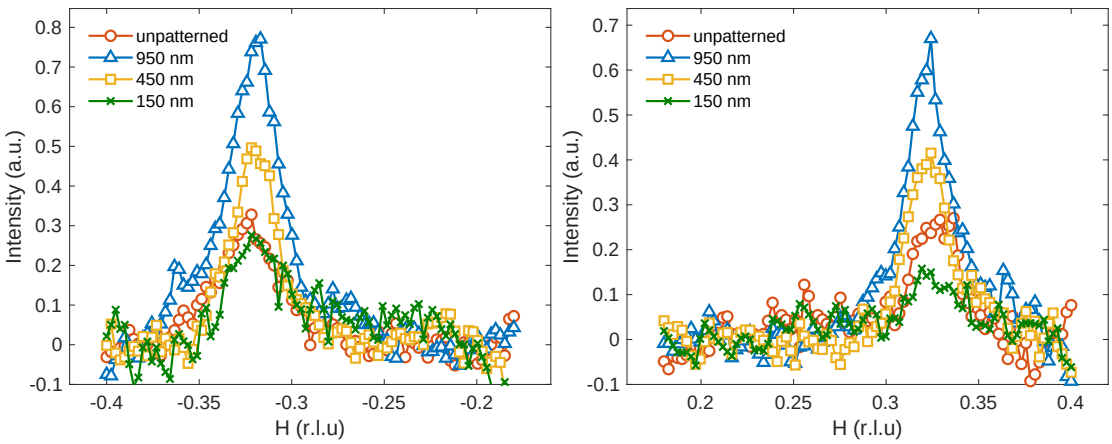

Figure 3.9: Result of the subtraction between low-T and high-T scans for sample DCA243, for both negative (left figure) and positive (right figure) H scans.

nanodots, but left the one of the non-patterned one unaltered: a lower doping could then result in a stronger intensity of the CDW peak; also, the fact that the lateral sides of the dots were exposed to a higher dose of ions could have changed their chemical properties. The fact that this is observed only for negative scans could be explained by the difference in the two experimental geometries needed to realize the scans. Indeed, as explained in the previous chapter (2), negative $q_{\|}$ is reached with a grazing in - normal out configuration (approximately), while positive $q_{\|}$ is reached with a normal in - grazing out one. In our case, this means that in negative H scans also the lateral sides of the dots receive a significant portion of the beam, while for the positive H scans only the top part of the dots is probed. Due to all these problems, data regarding this sample has to be carefully handled, keeping in mind that it's probably not reliable.

3.4 Simulations

We now describe the simple phenomenological model which we have used to interpret the experimental data. As already explained before, the reduction in the fill factor alone cannot explain the observed reduction in the peak intensity. We have therefore devised a very simple model that accounts for this behaviour: we first describe how the model works, and then we try to give it some physical meaning.

Out starting point is the usual interpretation of 2D charge order in cuprates as being composed by uncorrelated 'islands' of CDW, whose dimension corresponds to the correlation length [22]. We have imagined that there is a certain area within each dot in which CDW cannot nucleate at the border of every dot. In particular, we have supposed that charge order is present only in a smaller square inside the dots, whose distance from the real side of the nanostructures we have called d. Taking this into account, the effective area f of YBCO in which we can hope to find charge order changes. To calculate it, we imagine that the beam spot size is a square with side L much greater than the dimension of the nanostructures (which is surely true in Bessy II, since it is of the order of some hundreds of μm): we then make little error in supposing that an exact number N^2 of dots is contained inside the probed area, with:

$$N = \frac{L}{b+l} \tag{3.4}$$

where, as before, b is the distance between the dots and l is the their lateral size. We have then that:

$$\begin{aligned} f(l,b,d) &= \frac{N^2(l-2d)^2}{L^2} = \frac{L^2}{(b+l)^2} \cdot \frac{(l-2d)^2}{L^2} \\ &= \left(\frac{l-2d}{b+l}\right)^2 = \left(1 - \frac{b}{b+l} - 2 \cdot \frac{d}{b+l}\right)^2 \end{aligned} \tag{3.5}$$

which of course becomes equal to the formula for the fill factor when $d = 0$.

It seems intuitive that signal coming from charge order will be proportional to the area occupied by CDW (or, better, the area in which one expects to find CDW), so that:

$$I_{CDW} \propto \left(\frac{l-2d}{b+l}\right)^2 = \left(1 - \frac{b}{b+l} - 2 \cdot \frac{d}{b+l}\right)^2 \tag{3.6}$$

To verify this, we have performed some simulations using Matlab. We have modelled our sample as a square with size 1000 nm (to keep the problem computably tractable). We then have fitted dots of different size l inside this region, chosen so that each time there was an integer number of them in the region: 950 nm, 450 nm and 150 nm, with a distance between the structure equal to 50 nm. The fact that this situation does not resemble exactly the samples used in the experiment was not an issue: our aim was just to verify that formula 3.6 works. Inside each dot, we imposed that only in the central square of size $l - 2d$ charge order could be present. The way we have modelled CDW follows exactly the idea described

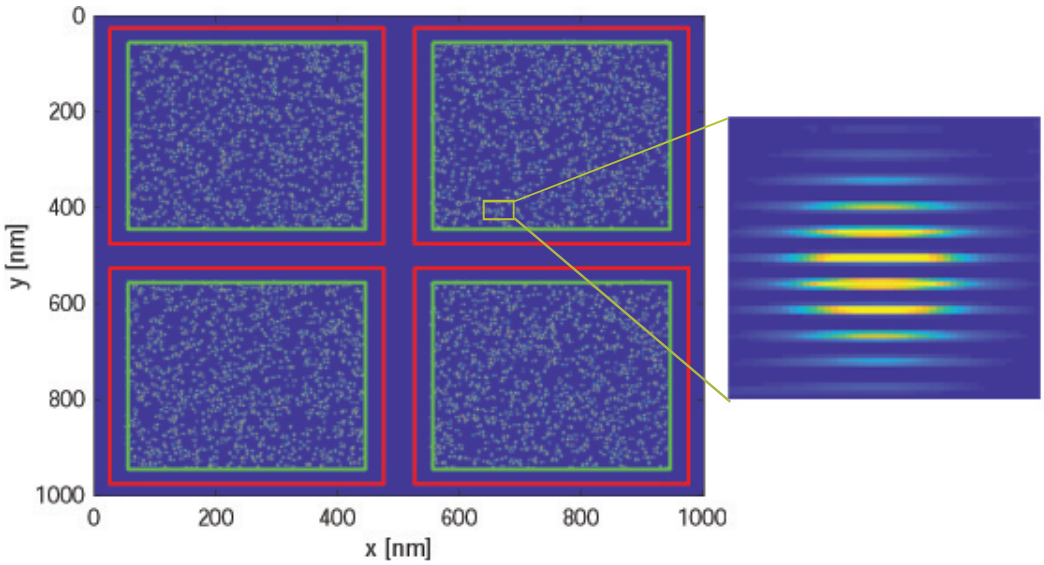

Figure 3.10: Real order parameter *psi* used in simulations. Red squares are the nanodots, green ones the region in which CDW can nucleate: the distance between the two squares is d, while the distance between dots is b. In this case, b = 50nm, d = 30 nm and the whole region is a square with size L = 1000nm. The inset is a zoom around one of the sinusoidal modulation.

above: each wave is a 1-D sinusoidal perturbation, with wavevector $q = 0.31$ r.l.u., with sizes equal to the correlation lengths derived by scattering techniques [25]. In particular, we used two different lengths along x and y to describe the partial anisotropy revealed by experiments [22]. Since their exact values didn't seem to be crucial in this type of simulations (the size of the dot is still much larger) we chose two safe values of 10 nm (parallel to the direction of the modulation) and 8 nm (perpendicular to it), which are compatible the one measured in YBCO at the magical doping $p = 1/8$ and at T_c [22, 25]. Instead of "cutting" sharply each CDW in a rectangle with sized equal to $\xi_{\parallel}$ and $\xi_{\perp}$, which would create strange artefacts in the Fourier space, we put each modulation inside a 2-D Gaussian envelope. To cope with the randomness of their disposition and orientation, we partially followed some ideas outlined in [27]. we introduced two random sparse matrices of "1"s and "0"s: each "1" represented the centre of a modulation. We then convoluted this sparse matrices with two sinusoidal functions directed along x and y respectively, whose sizes where 3.5 times the $\sigma_{x,y}$ of the Gaussian envelopes (to be sure that the two functions were zero at the edges).

Finally, we summed them: the result is a matrix representing a 2-D region, containing random sinusoidal modulations with a Gaussian envelope: an example is shown in figure 3.10 for 4 dots with size equal to 450 nm. After having defined the order parameter in real space, we took the Fourier transform of it using the FFT algorithm: the result is a set of four broadened peaks which correspond to the two different orientations of the modulations (along x and y). Since the peaks are in principle all equivalent, we chose the positive-H one and fitted it with a 2-D Gaussian, to extract the value of the intensity. This procedure is then repeated for the three different sized of the dots, and for different values of d. Note

that we are considering the absolute value of the spectrum, and not the squared modulus (which is the real physical quantity measured in experiments): this is just to make calculations easier. Indeed, if equation 3.6 holds, then indicating the Fourier transform with $\mathcal{F}(\psi)$:

$$|\mathcal{F}(\psi)| \propto \sqrt{I_{CDW}} \propto \left(1 - \frac{b}{b+l}\right) - \frac{2d}{b+l} \cdot l = a + b \cdot d \tag{3.7}$$

which is a simple linear relation in l. All the simulated intensities and the corresponding linear fittings are presented in figure 3.11: as can be seen, the relation is perfectly linear, as expected. Calculating the ratio between the polynomial coefficients, one finds a result very similar to the one expected, finally demonstrating that 3.6 holds.

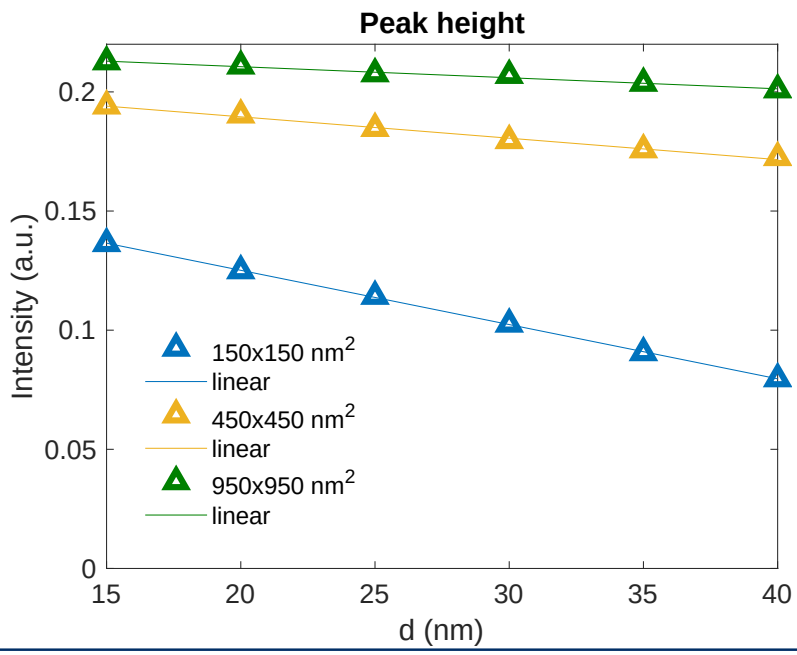

Dot Size [nm]	a	b	a/a_{950nm}	theoretical	b/b_{950nm}	theoretical
950	0.17071	-0.00228	1	1	1	1
450	0.20864	-0.00095	0.951	0.947	2.167	2
150	0.21930	-0.00044	0.778	0.789	5.197	5

Figure 3.11: Simulated Intensities for different d and l values, along with their linear fittings. As can be seen, the relation between them is perfectly linear. In the bottom table we report the calculated coefficients of the straight lines.

The next has been trying to fit the experimental intensities using formula 3.6. A way could have been to set:

$$I_{CDW} = I_0 \cdot f(d) = I_0 \cdot \left(1 - \frac{b}{b+l} - 2 \cdot \frac{d}{b+l}\right)^2 \tag{3.8}$$

which has two parameters: I_0 and d. This, however, would probably cause a great overfitting since we have just 4 experimental points (intensities on the

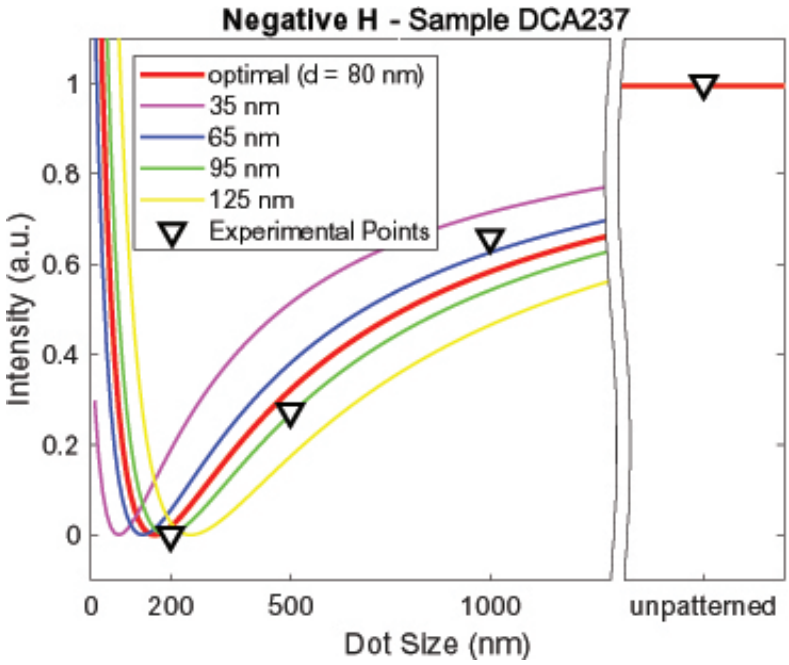

Figure 3.12: Intensities of charge order (normalized to the value in the unpatterned region) in dots with different sizes, fitted by the curve 3.5, for negative H scans. Also shown are other curves with different values of d.

unpatterned, 1000 nm, 500 nm and 200 nm dots). However, f can be interpreted as the ratio between the intensity of the CDW peak in a set of dots of size l separated by a distance b (and characterized by a parameter d) and the intensity in the unpatterned region. This means that if we normalize the intensities to the unpatterned region (which is used as a reference) we can use this function to fit the experimental data and obtain an estimation of d, which remains the only parameter. We thus sacrifice an experimental point, but in return we get rid of I_0. We present the results in figure 3.12 for negative H scans (for positive one, the situation is almost identical). Even if we have just three "experimental points", the curve resembles their behaviour, and the calculated value for $d \approx$80 nm is similar for negative and positive scans.

The physical interpretation of this "dead" layer in which CDW cannot nucleate is not easy. However, it could be related to the oxygen quenched disorder found by Campi et al. [1], described at the beginning of the chapter. If, for some reason, the oxygen patches become stronger at the edges of the sample, then this higher oxygen concentration does not favour the formation of charge order, which then could be present only in the inner part of the dots.

To sum up: we found a strong reduction in the intensity of charge order signal even in dots (1000 and 500 nm) whose size was much bigger than the correlation length of CDW. Moreover, signal completely disappears in the 200 nm dots. This decrease is incompatible with a reduction in the fill factor, and so we elaborated a simple phenomenological model that is based on the presence of a "dead" layer without CDW at the edge of the dots. This model seems to reproduce the experimental data, at least in this sample (DCA237). This result required, however, further investigation. As said, the experiment faced different problems:

- We can rely only on the data coming from one sample. Therefore, at the moment, we cannot check the reproducibility both of the experimental results and of the model used to fit it.
- Exposure of lateral side of the dots, which changes the effective area probed by the beam between negative and positive H scans (and also inside a single scan, as θ varies)
- Presence of Au capping, with absorbs part of the incoming beam, thus reducing the intensity of the signal measured.

These issues required devising another solution, different from nanodots. The solution has been found using a-axis oriented YBCO films, and the experiment regarding them is presented in the next chapter.

Chapter 4

Charge Order in a-axis oriented YBCO films

This section covers data acquired during a second experiment, complementary to the one described before on YBCO nanostructures. Here, we focused on searching CDW in a-axis oriented YBCO films, where the (100) direction is perpendicular to the film. This configuration presents some advantages with respect to the nanodots, but also some problems which will be described later. Experimental data has been acquired at the beamline UE46_PGM-1 in Bessy II during experiment 191-08109, performed in May 2019. To our knowledge, this has been the first resonant X-ray scattering experiment aimed at investigating the charge order signal in a-axis oriented YBCO films.

4.1 Motivations

As already explained in the previous chapter, the experiment of YBCO nanopatterned structures provided some very strong results, but suffered from intrinsic problems related to geometry which prevented them from being conclusive. First of all, the effective area probed by the beam depended strongly on θ, which is the angle formed by the beam and the sample surface: this is due to the fact that both upper and lateral surfaces of the nanodots were exposed. Also, the edges of the samples surely suffered from inhomogeneities, and at the same time such small structures were more prone to be damaged by the X-Ray beam (even if the fluence of the beam in Bessy is much lower than at ESRF). Finally, backgrounds changed heavily when taking scans along the diagonal: this made difficult to perform the analysis on CDF, where is necessary to subtract the scans along (H,H).

The use of a-axis oriented films solved most of these issues. Since they are non-patterned epitaxial films without edges, no problems in the homogeneity of the surfaces exposed were present; also, the area probed in the experiment remained the same during the scans. Finally, no Au capping is present, and thus the beam is not attenuated before reaching the sample. Despite all of these advantages, however, the use of these films created a few additional problems. The first one is that it's difficult to grow epitaxial structures with thicknesses intermediate between the nanoscale and the bulk material (around 1μm), where the CDW signal is

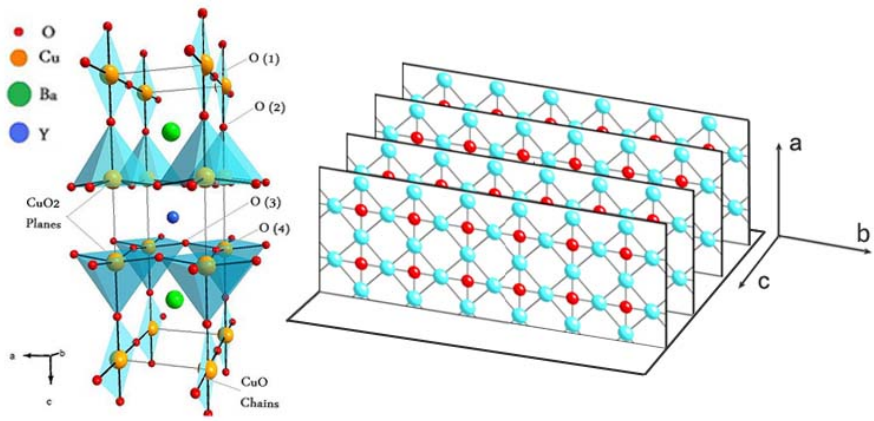

Figure 4.1: Left figure shows the crystal structure of YBCO. Right figure shows a simple scheme of an a-axis film, with the Cu_2 planes confined along direction a. The electronically inert layers between them are not shown.

expected to develop according to the previous experiment. Also, a buffer layer of $PrBa_2Cu_3O_{7-\delta}$ (PBCO) is necessary to grow films with good superconducting properties: this material, as it will be explained in the next paragraph, is extremely active in X-Ray scattering experiments because of Praseodymium, and thus its presence complicates the interpretation of the results.

4.2 Samples

The unique samples that have made this experiment possible have been realized by the group of Prof. F. Lombardi at Chalmers University of Technology. Although a-axis oriented films of cuprates have been grown since the 90's, only few groups have achieved, in the last years, the capability to obtain epitaxial systems which maintain good superconducting properties. The technique used by Chalmers' group involves depositing a $PrBa_2Cu_3O_{7-\delta}$ (PBCO) buffer layer onto a $SrGaLaO_4$ (SLGO) [100] through rf-sputtering at high temperature (800 °C), and then a YBCO film through standard PLD at 790 °C [60]. PBCO is a non-superconducting cuprate with the same structure as RBCO 123-perovskites and very similar lattice parameters, shown in table 4.1: Its presence is necessary, since depositing YBCO directly on

Material	a [nm]	b [nm]	c [nm]
YBCO	3.81	3.89	11.67
PBCO	3.865	3.916	11.688
LSGO	3.843	3.843	12.68

Table 4.1: Lattice parameters of YBCO, PBCO and LSGO.

SLGO (100) would result in inhomogeneous YBCO films, with a mixture of a/b-axis oriented and c-axis oriented islands; the thickness of this seed layer is 90 nm.

In our experiment, we measured samples in the slightly Under Doped and Under Doped regime (with critical temperatures going down to 65K) with thicknesses

ranging from 10 nm to 300 nm. In particular, we concentrated on three of them: a slightly UD 300 nm-thick YBCO with $T_c = 85$ K, an UD ($T_c = 65$ K) 50 nm-thick one and a pure 90nm-thick PBCO film, which we used to study the effect related to Praseodymium. An overview of the sample used is presented in table. 4.2.

Sample	YBCO Thickness [nm]	PBCO thickness [nm]	Doping	T_c [K]
19-36	300	90	UD	85
19-39	300	90	UD	80
19-31	50	90	UD	65
19-35	0	90	-	-

Table 4.2: Table showing main properties of the samples studied.

The samples have been characterized by measuring the electrical resistance along both in-plane directions (which now are b and c) as a function of the temperature: this is a direct measure of T_c, and the sharpness of the transition allows to test the quality of the films. Figure 4.2a and 4.2b show R(T) curve for sample 19-36 and 19-31, respectively. As already explained before, the main problem of this

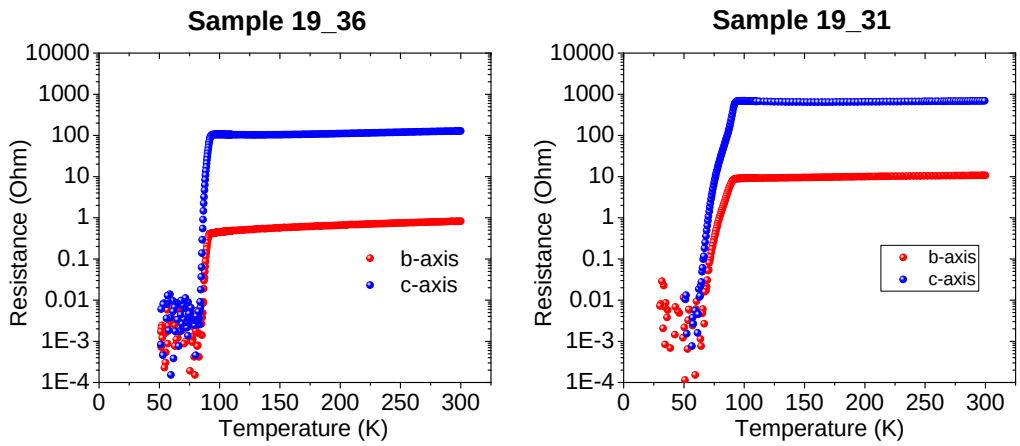

(a) (b)

Figure 4.2: R(T) for sample 19-36 (YBCO a-axis UD 85K, 300nm) and sample 19-31 (YBCO a-axis UD 65K, 50nm), respectively. Superconducting transition is very sharp, an indication of the good quality of the samples.

technique (at least for what concerns X-ray scattering studies) is indeed the PBCO layers itself. Praseodymium has indeed an M_5 line which lies just 3eV before the Cu L_3 edge. This means that an incoming beam with a bandwidth of 1eV or more will produce also excitations coming from Pr ion in addition to the ones coming from CU_2 planes (such as CDW). This effect is of course more evident in ultrathin YBCO films, since X-rays at 930 eV have a penetration depth which is of the order of 100 nm.

4.2.1 Experimental details

As said at the beginning of the chapter, the experiment has been performed at the UE46-PGM1 beamline at Bessy II. Like before, we probed Cu L3 edge: $E \approx 931.3$ eV, with a corresponding $\lambda = 1.33$ nm . Two different geometries have been used: we will here outline the first one, and we will leave the discussion about the (more unconventional) second one to the next section. The orientation of the

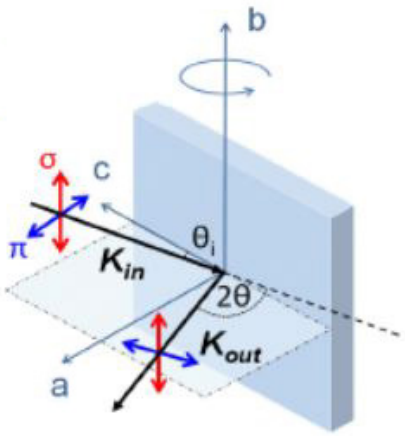

$$H = (|\mathbf{Q}|/c^*)\cos(\delta)\cos(\chi)$$
$$K = (|\mathbf{Q}|/b^*)\cos(\delta)\sin(\chi)$$
$$L = (|\mathbf{Q}|/a^*)\sin(\delta)$$

Figure 4.3: Schematic of a-axis geometry. Note the unconventional position of crystal axis w.r.t. to incident and scattered wavevectors. On the right, corresponding formula for H, K and L. Readapted from [41].

three sample axes is radically different with respect to the one outlined in the previous chapter and is shown in figure 4.3. Now, a lies in the scattering plane but is perpendicular to the sample surface, while b is perpendicular to the scattering plane. This of course changes the angles used to reach the point (0.31, 0, L), where one expects charge order to be. In particular, equations (2.21) for $Q_{\parallel}$ and $Q_{\perp}$ have to be interchanged, as reported in figure 4.3. As can be seen, only positive (or negative, depending on the convention) values of H can be probed. We searched CDW both at 1.45 r.l.u. and 1 r.l.u., since they are sufficiently far from Bragg reflections. The corresponding angles were $2\theta^{L=1.45} = 160°$ and $2\theta^{L=1} \approx 103°$, fixed by the total momentum $\mathbf{Q}$, and $\theta^{L=1.45} \approx 140°$ / $\theta^{L=1} \approx 101°$. The first choice corresponds roughly to a grazing-in normal-out configuration, while the second one to normal-in grazing-out. To perform the H scans, we again varied θ keeping 2θ fixed, to minimize the motion of motors. Moreover, we still used vertical (σ) polarization since it was still lying in CuO_2 planes along Cu-O bonds (see figure 4.3).

Since we were expecting a weak signal, we maximized the incoming photon flux by adjusting the exit slit. This worsened a bit the resolution on the incoming light, which was now ≈ 1 eV. While this is usually not a problem for charge order detection, it became a partial issue in this experiment due to the vicinity of Cu L3 edge (~ 931.3 eV) with Pr M5 (~ 929 eV).

4.3 Data Analysis and Results

As said, we have concentrated more on samples 19-36, 19-31 and 19-35 (pure PBCO). At first we have searched the presence of CDW peaks along H direction. The experimental geometry is the usual one used in RIXS (or REXS) experiments with the sample perpendicular to the scattering plane. The only difference is that now a-axis is perpendicular to sample surface, so that now is the $q_\perp$ which is critical to the experiment. We have also used different L values during the measurements, exploiting the fact that CDW signal should not depend on q_L since there's no correlation between different CuO_2 planes [2, 22, 25].

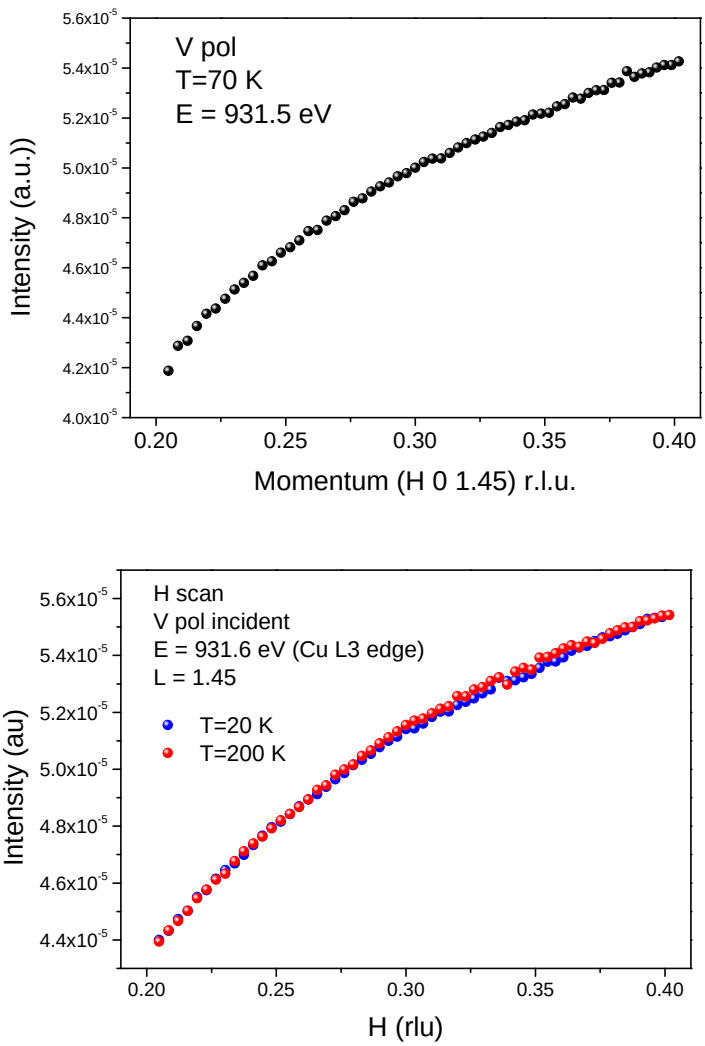

Figure 4.4: Hscan, at L=1.45, for samples 19-36(UD85 (top) and 19-39 UD 80 (bottom). Both samples are 300nm thick and are grown over PBCO. No CDW-related peak is visible. Both scans were performed at Cu L3 edge, and the one on 19-39 also was performed at two different temperatures).

Initially we have searched a Charge Order signal in sample 19-36, which has a thickness of 300 nm. H-scans were performed at cu L3 edge (931.5 eV) and at

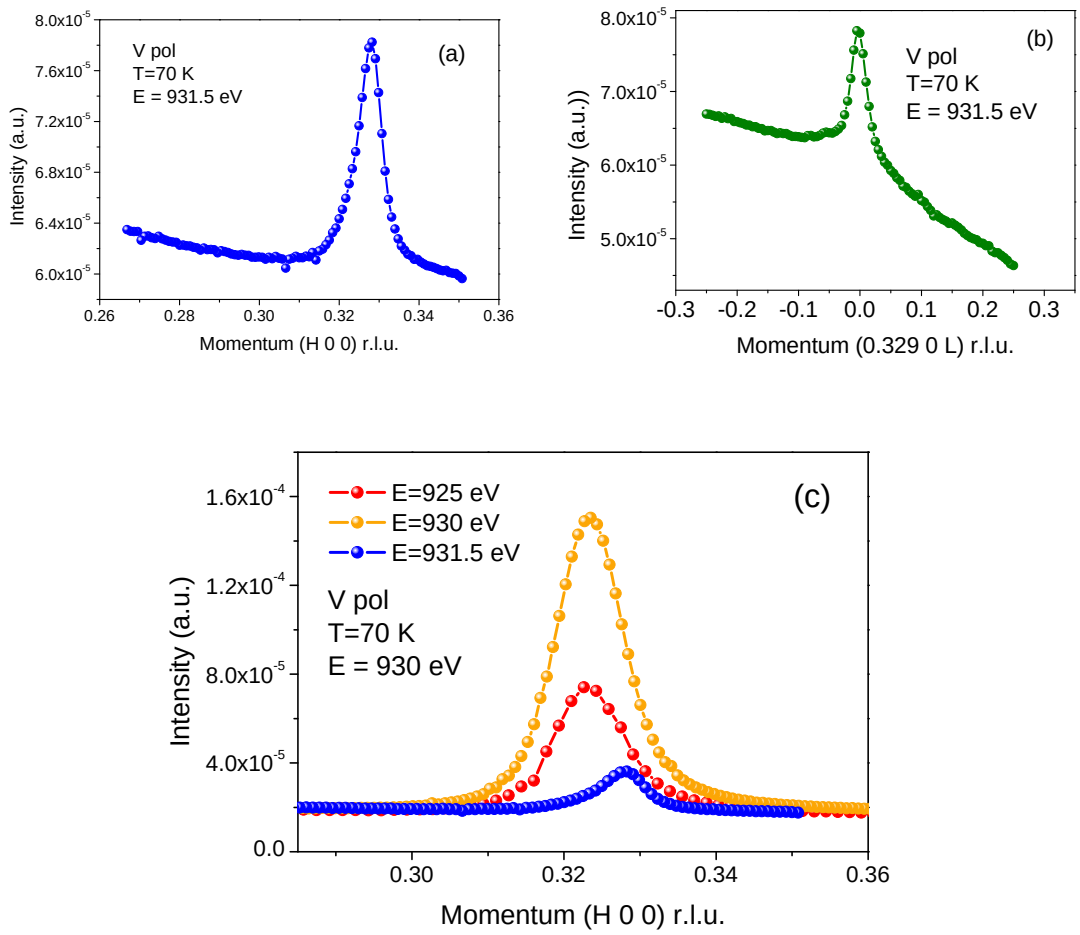

Figure 4.5: (a) H scan around 0.31 at K=0 and L=0,showing the presence of a strong superstructure peak. (b) L scan performed at H=0.325 and K=0, where the peak reaches its maximum value. (c) Energy dependence of the peak.

L=1.45. Based on the results of previous chapter, we expected to find evidence of CDW, though with an intensity reduced roughly by a factor 10. However, as shown in figure 4.4, no evidence of CDW was found along H at $L = 1.45$ at the Cu L3 edge. The same scan was repeated on sample 19-39, which has the same thickness of 19-36 (300nm) but it is even more underdoped: again, no peak was found (figure 4.4). To rule out the possibility of some strange "under peak" at high temperature we explored momentum dependence at 20 and 200K. We then decided to change the value of L to 0, and we found an extremely strong peak, with an intensity about 24% of the background.

To establish definitively that it was not related to charge effects, we performed three checks: first a L-scan (figure 4.5) which showed that the peak is very narrow along L, a behaviour completely incompatible with ordinary 2D charge order; then, an energy dependence of the intensity of the peak. These last scans, which we report in figure 4.5, seem to indicate that peak is resonating at the Praseodymium M5 edge, and is thus related to PBCO (the buffer layer). Finally, a temperature dependence showed that this peak is T-independent. All this information (high

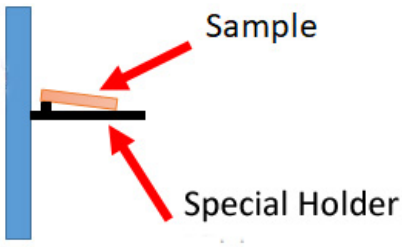

Figure 4.6: Schematic representation of the holder used for the K-scans. Angle χ was not precisely measured, but we can estimate it to be less than 5°.

intensity, sharpness in momentum space, temperature independence) favour the hypothesis of a super-structure peak, although it is unclear why it is present at an incommensurate H value. Since we recognized that Pr was apparently playing an important role in the measurements, we tried to explore all the effects related to it in thinner sample, where X-Rays penetration depth is greater than thickness of YBCO films. Much of this analysis was performed on a YBCO sample UD 75K 50nm thick, and revealed some interesting and not expected results. Since it is not directly related to the charge order in YBCO, we have dedicated an appendix to it A.

The second main part of the experiment has been dedicated to search the presence of charge order signal also along K direction in reciprocal space. To do that, we have worked on sample 19-31, a YBCO UD film 50nm - thick with a T_c of 65K. Even though such a small thickness increases signals coming from Praseodymium, this choice was motivated by the fact that signal coming from charge order is maximized in under-doped samples. At first, we have again verified that no CDW peaks are present along (H,0) direction. Multiple scans were performed at different L, because again nothing was found around $L = 1.45$ r.l.u. No charge order related peaks were detected.

As it has been already mentioned, in this type of samples H lies along the perpendicular component of the transferred momentum (at least when $\chi = 0$), therefore $q_\perp$ cannot be made negligible while keeping $q_\parallel \approx 0.3$. The solution to this problem is to rotate the sample along angle χ to almost 90°: a rotation of exactly 90° would in principle make H zero, but then the effective surface of the sample probed by the beam would be vanishing, so that angles χ too close to that value reduce too much the intensity of the signal. Since UE46 diffractometer does not have any motor controlling motion along χ, we have mounted the sample on a special holder, whose scheme is presented in figure 4.6. Before proceeding with the momentum scans, we have checked whether Praseodymium-related effects were still visible in this configuration by performing a XAS on the sample (figure 4.7a): Pr M5 edge disappeared both in Fluorescence and Electron yield. This is due to the fact that minimization of H now requires grazing incidence, and thus the effective penetration depth decreases by a factor $\sin\theta$, where θ is the angle between incident (or scattered) beam and the surface of the sample. To reach the point (ε , 0.3 , 1.45) in reciprocal space we used $\theta = 135.9°$ and $2\theta = 158.6°$. Using our estimate

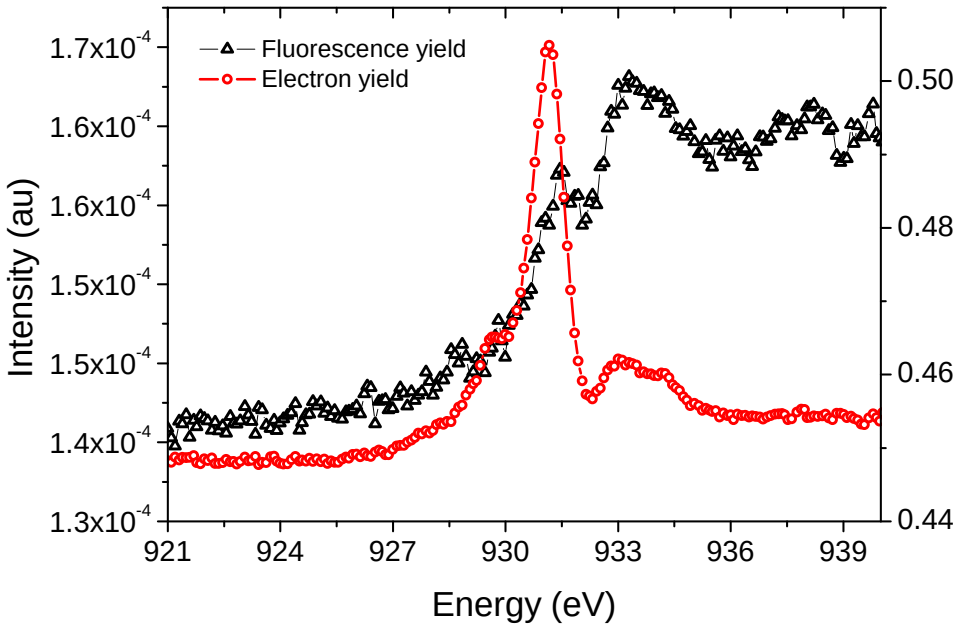

(a) XAS on YBCO UD 65K, 50nm thick, in fluorescence (left axis) and electron (right axis) yield. Praseodymium M5 edge is only slightly visible.

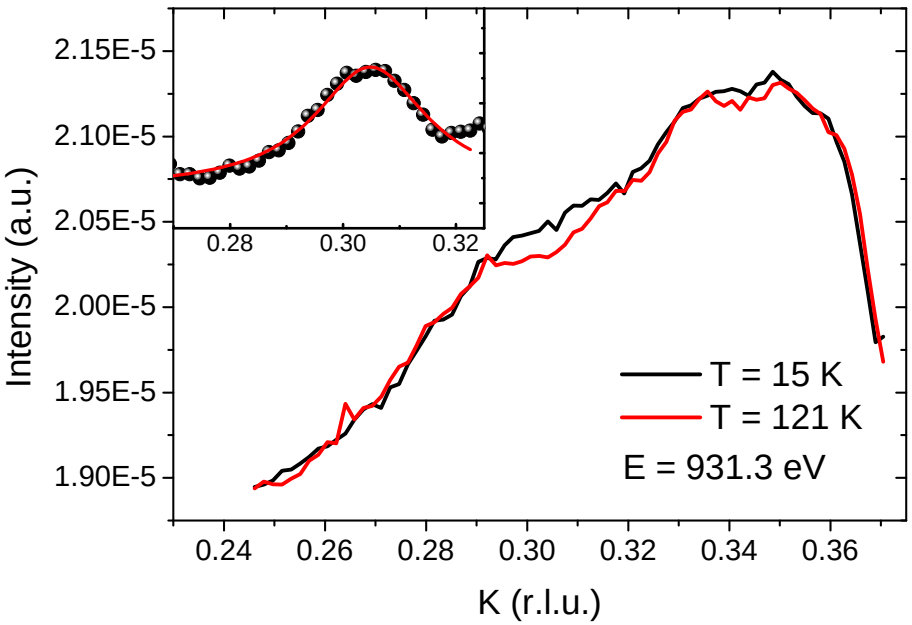

(b) Raw scan (ε , K , 1.45) at T = 15K and T = 121K. Energy was set at 931.3 eV, the maximum of Cu L3 edge according to XAS (figure 4.7a). A clear bump is visible around K = 0.3 in low - T scan. Figure's inset shows a peak resulting from the subtraction of the two scans, with a lorentzian fitting.

Figure 4.7: XAS and (H,0) scan on sample 19-31 mounted on the new holder.

of $\chi = 87°$, we can calculate:

$$|H| = 2k_0 \sin\frac{2\theta}{2}\cos\left(\theta - \frac{2\theta}{2}\right)\cos\chi \approx 0.011\ r.l.u. \tag{4.1}$$

Which is small w.r.t K=0.3, but still quite comparable with the FWHM of the Narrow Peak along H direction, and thus reduces signal coming from CDW peak roughly of a factor 2. Since we were expecting an extremely weak peak, we acquired scans also at high temperature (121K) and used them as a background, subtracting them to low - T scans. The energy was set to 931.3 eV, the maximum of XAS absorption spectrum according to the XAS. aw data is presented in figure 4.7b: each scan is the average of 4 curves and each point had a 1 ms acquisition time. First, we note that the complex experimental geometry produces a strange background that cannot be fitted easily by a polynomial, and in which it's impossible to recognize a peak. Also, around $K = 0.34$ (or, equivalently, $\theta = 129°$) signal falls abruptly. This is of course not a feature of the material, and it's probably due to a certain portion of the beam impinging out of the sample while θ moves. Despite all of these problems, we can indeed observe a clear bump in the low temperature scan centred at $K = 0.3$, which is more or less the position at which one expects the CDW - wavevector to be when $p \approx 0.12$ [22].

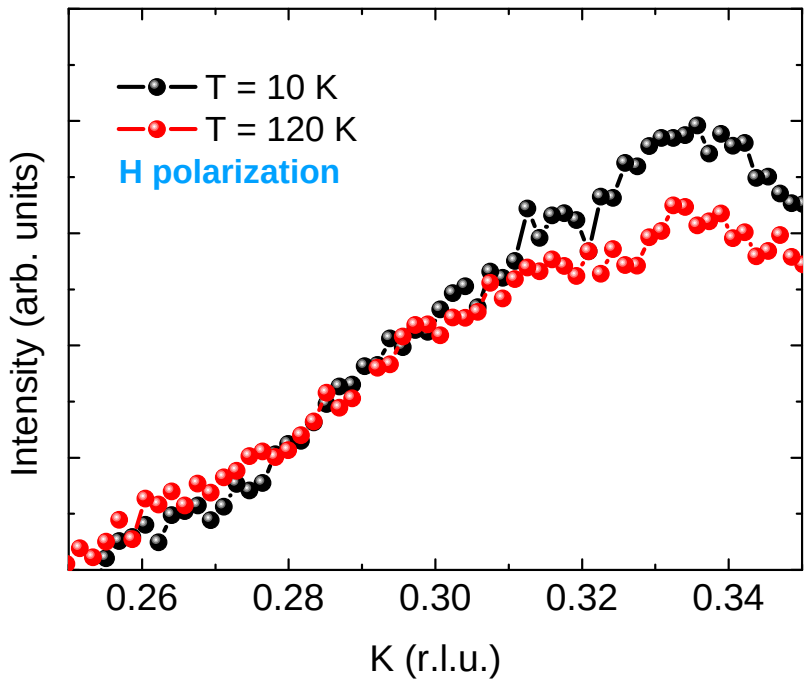

Figure 4.8: K scan with H polarization at 15K and 121K. No peak is visible around 0.3 r.l.u. Due to geometrical reasons, background changes a high T, giving rise to a spurious peak.

To establish that the peak observed is indeed due to charge order, we used two different methods. First, we checked whether it was present also with H polarization:

as known, the CDW signal is greatly reduced when incident light has a polarization not completely lying on a-b plane [25]. We performed a low - T and a high - T scan with horizontal polarization, with results shown in figure 4.8. As can be seen, apart from a very strange background, no superimposed peaks are visible in the scan @T=10K. The two scans become quite different at high values of H, an effect probably due to geometrical problems as explained before.

Second check was the energy dependence of the peak. Since charge order is a phenomenon related to Cu atoms residing in CUO_2 planes, it should disappear when moving away from Cu L3 resonance around 931 eV. We acquired other scans at other five different energies (930.3 eV, 930.6 eV, 931.6 eV, 931.9 eV, 932.5 eV and 936 eV) at both low and high energy: raw scans are presented in figure 4.9. As can be seen, backgrounds become stranger moving away from L3 resonance,

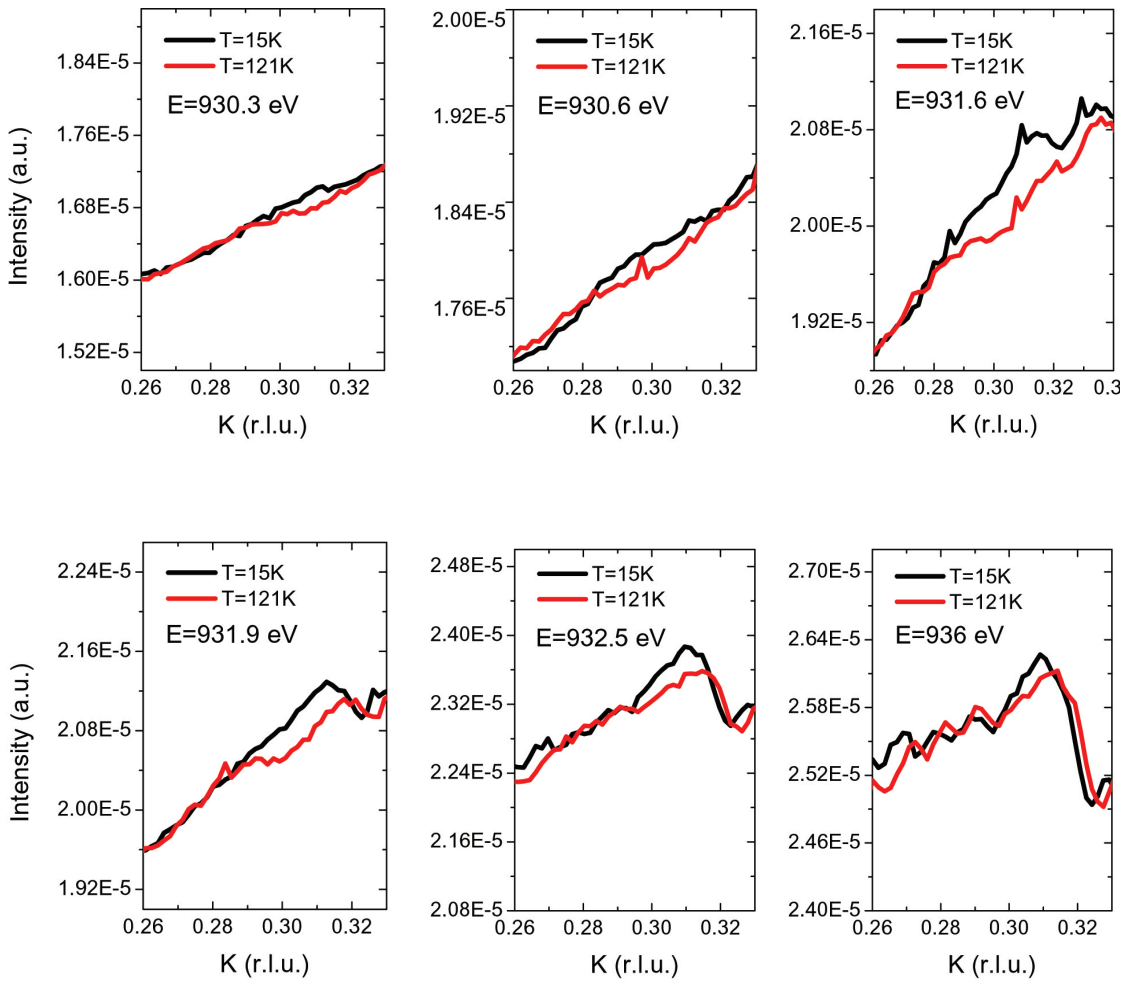

Figure 4.9: K-scans at different photon energies (E increases from left to right and from top to bottom). L=1.45 r.l.u. for all the scans. As can be seen, the bump disappears when moving away from Cu resonances, but at the same time background's shape becomes more complicated.

and there's no more a satisfying match between different temperatures. At each

photon energy, we followed the same procedure outline before for the scan at 931.3 eV: we first removed the pikes caused by the top-up injection method, and then we smoothed the curves to reduce uncorrelated noise; the results are shown in figure 4.10. Despite the fact that background's shape becomes more complicated moving away from resonance, making subtraction more and more problematic, a clear reduction in charge order signal is visible. Fittings are presented for 930.3, 930.6, 931.6 and 931.9 eV.

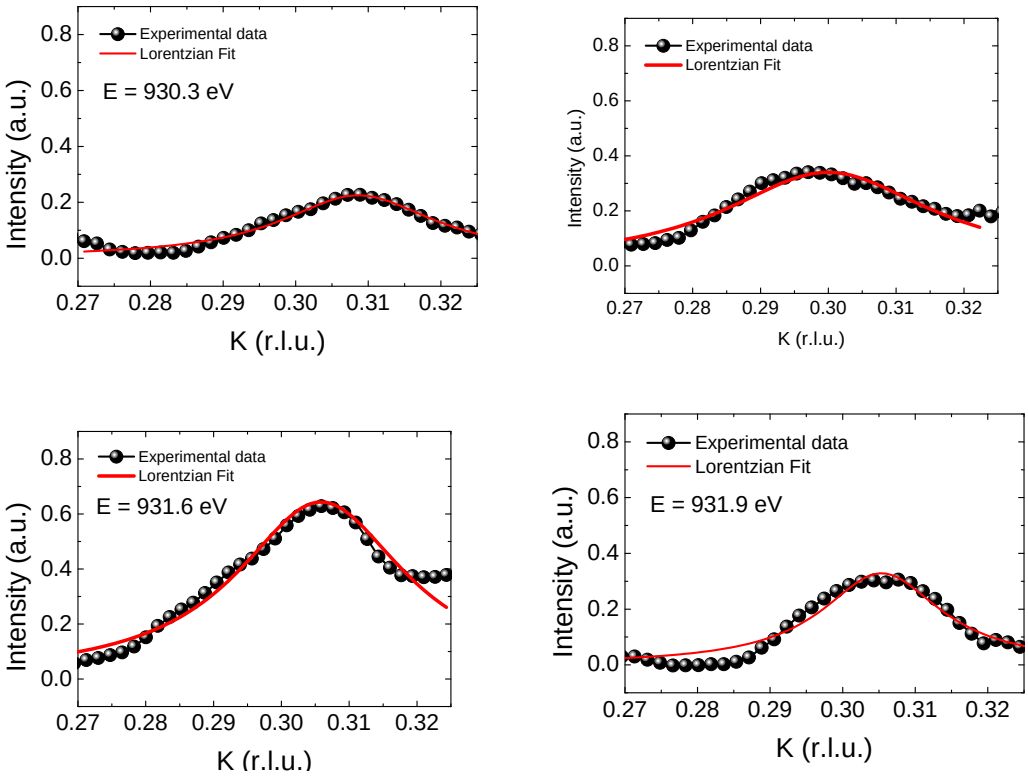

Figure 4.10: Result obtained subtracting scan at 15K with scan at 121K. Curves have been smoothed before subtraction using Adjacent-Averaging. Also shown are Lorentzian fitting of the peaks.

To better quantify the reduction in signal, we compared it to the XAS scan (figure 4.11) As shown in [61], the normalized intensity of the peak follows the shape of the absorption signal around the resonance. The XAS signal (in electron yield) is plotted with a solid line, while the dots represent the intensity of the CDW peak (fitted with a Lorentzian). Since we missed the maximum of Cu L3 absorption, intensities were normalized at $E = 931.6$ eV. The big error bars are mostly due to uncertainty of the fitting parameters, which result in big confidence intervals. CDW signal indeed vanishes when moving away from Cu resonance and nicely follows the absorption shape, at least within error.

These two experimental verifications demonstrate that the bump observed at $K = 0.3$ $r.l.u.$ at low temperature comes indeed from charge density waves. To sum up, our analysis showed that no charge order signal is present along H in a-axis oriented films, even at 300 nm, but it is still visible along K direction.

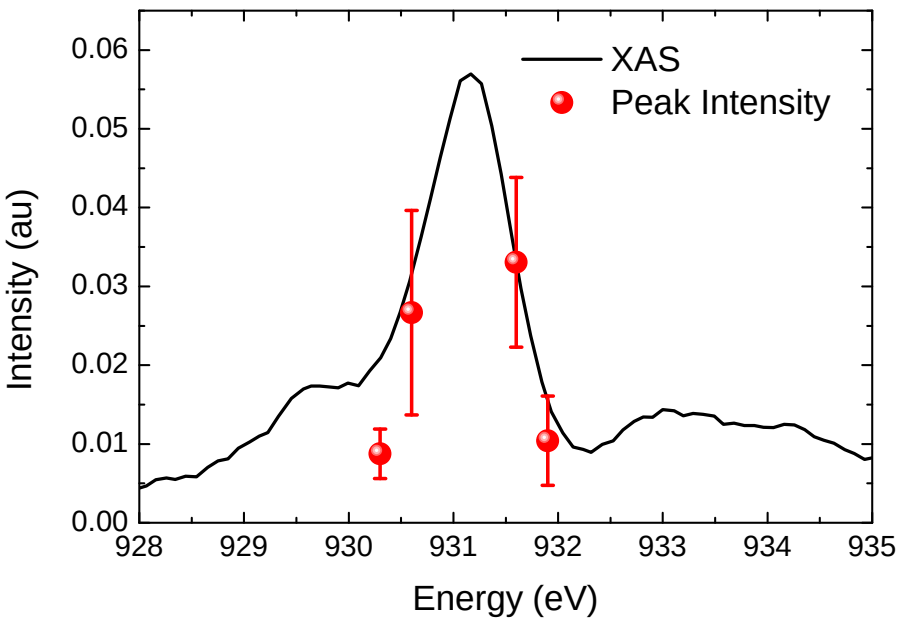

Figure 4.11: XAS vs Intensity of charge order peak. XAS is plotted in solid line. Since maximum of Cu absorption was missed, intensities have been normalized at 931.6 eV.

This is in agreement with the results of the previous chapter on YBCO nanodots, which showed a significant reduction of peak intensity when shrinking the lateral dimension of the structures (i.e. when reducing the area of Cu_2 planes). These experimental results seem to indicate that CDW are affected by a mesoscopic confinement of a-b planes; also, only waves with wavevector parallel to the direction of confinement disappear, while the other ones survive. This is in agreement with what observed on nanodots (and an even stronger result, since here we have found CDW along "non confined" direction). The next step will be to measure what happens with a YBCO thickness between 500 and 1000 nm (i.e. the range between nanoscale structures and bulk material): this is however a more challenging task under the point of view of material growth, since such thick films could be much less homogeneous.

Appendix A

Unexpected incommensurate peaks in PBCO

In this appendix, we will present some interesting results obtained when studying a-axis films, and which we have (with a high degree of certainty) attributed to the $PrBa_2Cu_3O_{7-x}$ (PBCO) seed layer. For clarity, we report here the table with the characteristics of the studied films:

Sample	YBCO Thickness [nm]	PBCO thickness [nm]	Doping	T_c [K]
19-36	300	90	UD	85
19-39	300	90	UD	80
19-31	50	90	UD	65
19-34	50	90	UD	75
19-35	0	90	-	-

Table showing main properties of the samples studied.

A.1 Superstructure peak

When searching for charge order in sample 19-36 (see table 4.2), which was 300 nm thick, we found a very strong peak along H located at a value close to the one expected for CDW. In particular, it was located at (0.325, 0, 0), meaning that it has an incommensurate value along H direction but a commensurate one along L. The proves that it is indeed not related to charge order in YBCO were already outlined in the previous chapter (4), and we will present here a brief summary.
First, the peak was very sharp both in H and L directions (see figure 4.5 in the previous chapter), something not compatible to 2-D charge order, that shows no dispersion along the L direction in reciprocal space [25]. As shown in the next figures, the peak was present also in sample 19-34, 19-31 and most importantly in sample 19-35, which only contained PBCO (we will not show this scan here). Since we could not easily access points with $H = 0$, we do not know whether it is present also along the K direction. Its intensity is about 30% of background in sample 19-36 and it is even bigger in sample 10-34 and 19-31 (see figure A.1, right

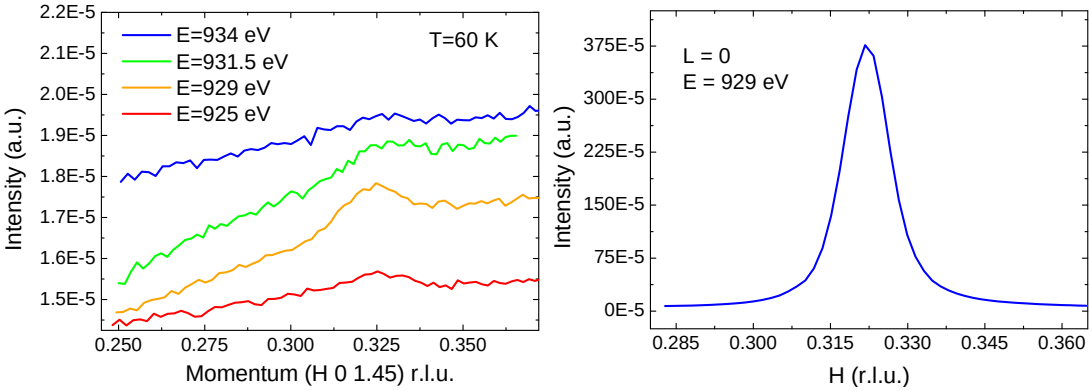

Figure A.1: Superstructure peak in samples 19-34 and 19-31, measured with H scans at $E = 929$ eV (Pr M5 edge). Left panel (sample 19-34) was taken at L=1.45, right panel (sample 19-31) at L=0.

panel), where the thickness of YBCO film, acting as a capping layer, is smaller. In particular, in sample 19-34 it remains visible even at L=1.45, as can be seen from figure A.1 (left panel). Such high intensity could be also due to the fact that we are at specular reflection, since $L \propto Q_{\parallel} = 0$.
Secondly, while giving appreciable signal also at Cu L3 edge (931.3 eV), it clearly resonated at the Praseodymium edge (929 eV), meaning that it was a feature of PBCO and not of YBCO (see again figure 4.5 in the previous chapter). We report

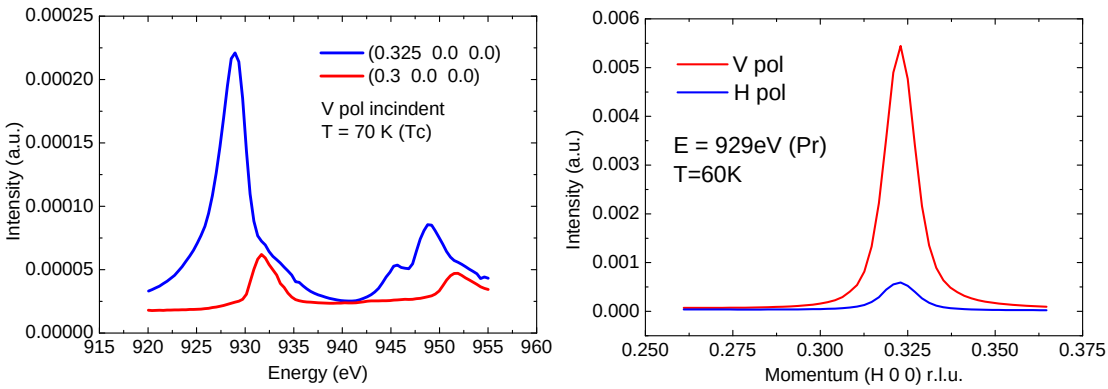

Figure A.2: Left panel shows a XAS in TFY for sample 1936, for H=0.325 (at the superstructure peak) and H=0.3. Right panel shows the polarization dependence for L=0: red is σ, blue is π.

here a XAS measurement in Total Fluorescence Yield (TFY) at two different points in reciprocal space. At H=0.325, where the peak reaches its maximum, the XAS shows a dominant contribution from Praseodymium; when instead we move away from that point, Cu L3 edge is the only absorption peak detectable.
Finally, it showed no significant temperature dependence, as shown in figure A.3 for sample 19-34.
All this information point clearly towards a superstructure peak. The fact that it shows dispersion along both H and L means that the modulation has a three dimensional character. Moreover, the H value seems to be incommensurate with the lattice. Another interesting feature is that the peak intensity clearly diminishes

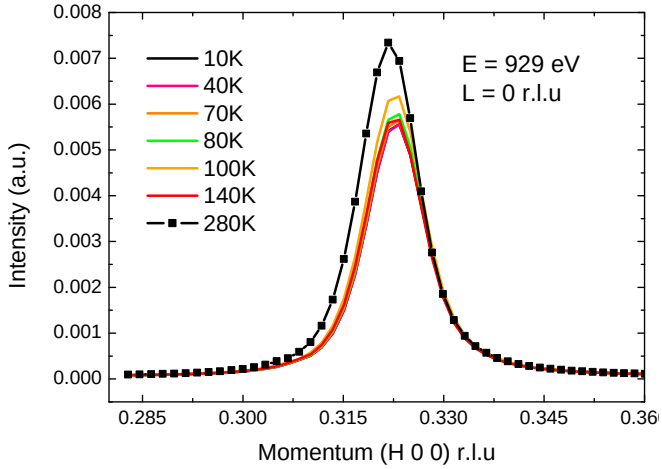

Figure A.3: Temperature evolution of the superstructure peak in sample 19-34. As can be seen, only a mild dependence is present.

when using H (π) polarization (figure A.2).

A.2 Temperature dependent peaks in samples 19-34 and 19-31

While investigating this superstructure peak in sample 19-34, we found another feature located at slightly different values of H and L: we will refer to this peak as the "second feature". H and L scans at T= are reported in figure A.4. This new peak

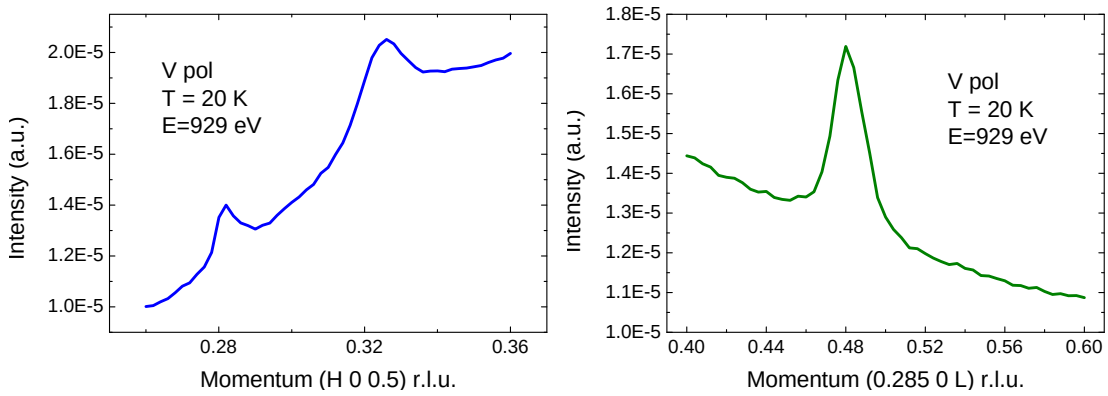

Figure A.4: H and L scans of the temperature-dependent feature in sample 19-34, located in (0.285,0,0.48). Both scans were performed at T=20 K and at the Praseodymium edge (E = 929 eV). The peak near H =0.32 r.l.u is the superstructure peak.

is clearly centred at (0.285, 0, 0.5) and is quite sharp both in H and L. Moreover, it seems to resonate at both Pr and Cu edges, differently from the superstructure peak. To establish its nature, we performed a temperature dependence at both edges. Since the results are similar, we present only the ones acquired at E = 929 eV. To isolate the peak from the background, we could not subtract the scan at

high T, because the intensity never decreased to zero at all temperatures probed. We then simply fitted a fourth order polynomial in the region away from the peaks, and then subtracted it from the scan considered. The results, along with the raw scans, are presented in figure A.5; parameters have been extracted from a lorentzian fitting. The intensity clearly drops between 60 and 65 K, which is slightly lower

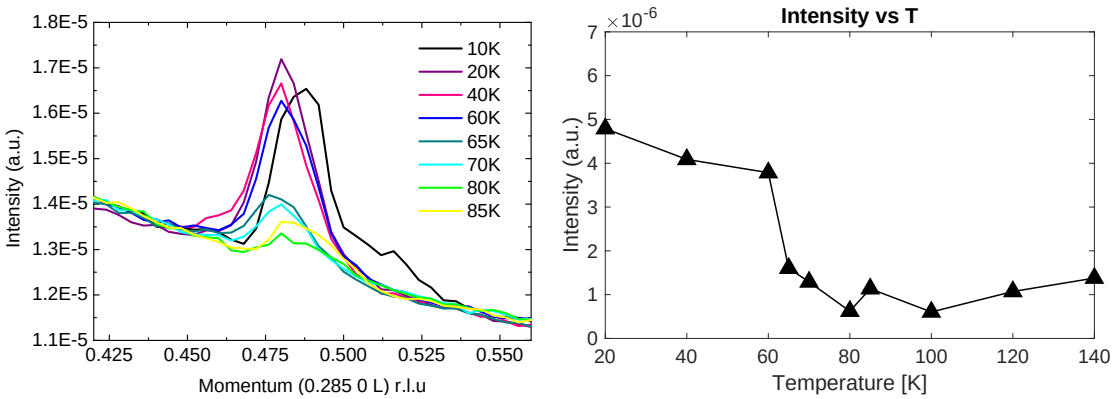

Figure A.5: Temperature dependence of second feature in sample 19-34. L scans were centred at H=0.285, on the maximum of the peak along H. In the left panel, scans above $T = 85$ K are not shown for clarity. Energy was set at Pr M5 edge (929 eV).

than the T_c of the YBCO film (75 K). However, it never disappears completely, but interestingly seems to rise again between 100 and 300 K. This behaviour is present along the two directions H and L. The width is instead more or less constant with temperature.

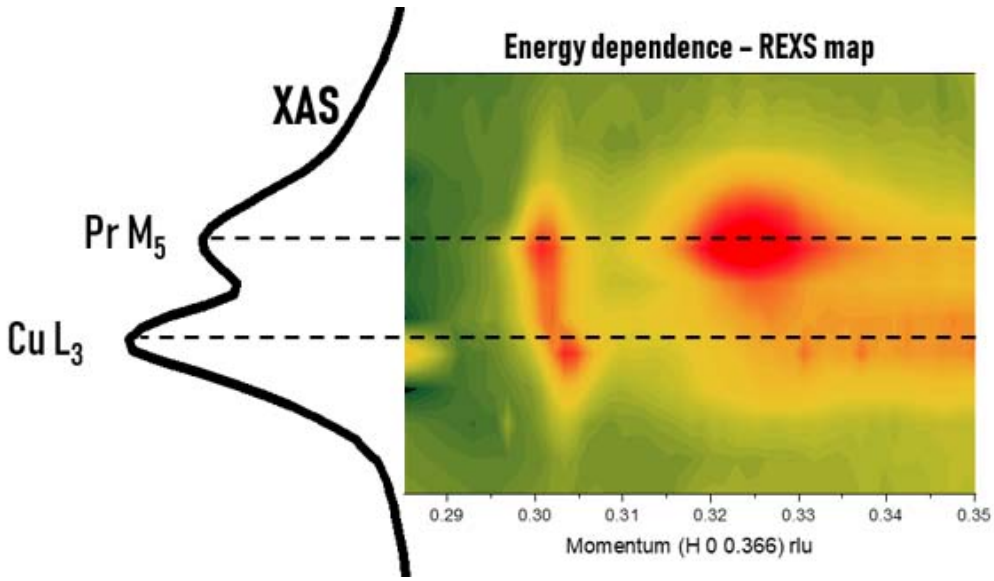

Figure A.6: Momentum-Energy map on sample 19-31 at $T = 20$ K and $L = 0.366$. Curves between the energy values effectively probed have been interpolated for clarity.

A similar peak was found also in sample 19-31 at $T = 20$ K, but centred in (0.293, 0, 0.366). While the position in momentum space is clearly different in L,

these two peaks share some characteristics. First, the H value is similar (0.285 vs 0.3). Secondly, they resonate both at Cu L3 and Pr M5 edges: figure A.6 shows a momentum-energy map. As can be seen, while the superstructure peak disappears when moving away from 929 eV, the second feature found in sample 19-31 does not have a clear resonance at either Copper or Praseodymium.

A.3 Peaks in sample 19-35

Finally, we performed a reciprocal-space map on sample 19-35, which only contained PBCO. As said before, the superstructure peak was again present, although with a slightly different value of H. When searching for the second feature around the (0.3,0,0.45) point, we found two distinct peaks. Figure A.7 reports the scans of the plane H-L: the two peaks are quite sharp, with an approximate FWHM of $\approx$ 0.005 r.l.u., and are located at (0.293, 0, 0.48) and (0.305, 0, 0.41), respectively. They were present at both Pr M5 edge (929 eV) and Cu L3 edge

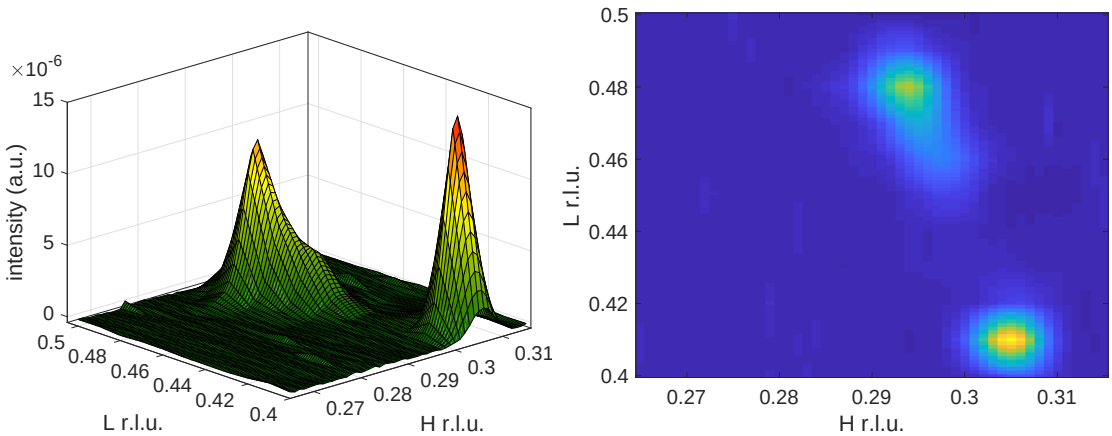

Figure A.7: 3D and 2D reconstruction of scanned part of H-L plane in PBCO ($T = 20$ K, $E = 929$ eV). As can be seen, the two peaks are located at different values of both H and L; moreover, while the peak at L=0.48 seems to have an elongated shape, with an oblique principal axis.

(931.6 eV), albeit with a lower intensity at Cooper edge.
We performed a temperature dependence on the two peaks, and found results similar (but not equal) to the one obtained for the "second feature" on sample 19-34, which underwent a strong reduction in intensity between 60 and 65 K: results are shown in figure A.8 for E =929 eV. While the intensity of the peak in (0.293,0,0.48) shows a smooth drop between 20 and 60 K, the intensity of the other one displays a sharper decrease between 40 and 60 K. This might be associated with a phase transition, but it is unclear of which type. It seems unreasonable, for example, to think of a magnetic transition, since PBCO is an antiferromagnetic material but the Neèl temperature is around 19 K (at least in crystals) [62, 63]. Another interesting property is that the peak has an elongated shape, but the principal axis (i.e. the one with bigger FWHM) is not oriented along H or L, and is instead oblique in H-L space. Finally, it is worth to note that the peak at (0.293, 0, 0.48) shares a

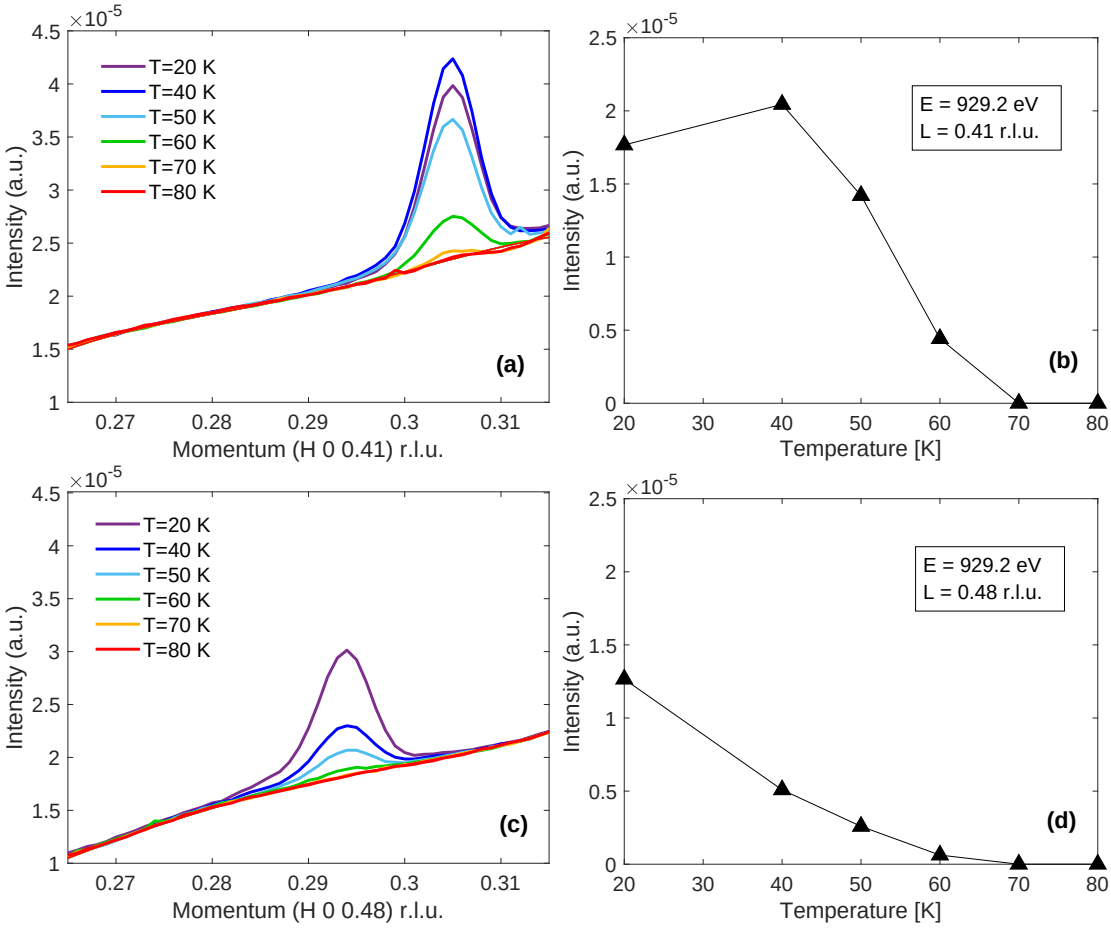

Temperature [K]	L=0.41		L=0.48	
	Intensity [a.u.]	FWHM [r.l.u.]	Intensity [a.u.]	FWHM [r.l.u.]
20	1.77(7)	0.0055(2)	1.26(5)	0.0059(2)
40	2.04(8)	0.0055(2)	0.51(2)	0.0060(2)
50	1.42(6)	0.0055(2)	0.26(2)	0.0060(3)
60	0.4(3)	0.0048(3)	0.06(2)	0.005(1)
70	0	-	0	-
80	0	-	0	-

Figure A.8: Panels (a) and (c): raw H scans of the features in $L = 0.41$ and $L = 0.48$ r.l.u., respectively, for different temperatures. Panels (b) and (d) report the corresponding Intensity vs T curves, as extracted from lorentzian fittings. Table reports the parameters used in fittings: errors, coming from confidence intervals in the fitting, are reported in parenthesis.

similar position with the "second feature" found in sample 19-34 (figure A.4), but a quite different temperature dependence, which is softer in this case.

To sum up: we observed a lot of different features clearly related to PBCO. First, we found a ubiquitous strong peak probably related to a super-structure: it was centred in (0.325,0,0), resonated only at Praseodymium edge and showed no temperature dependence. Moreover, its intensity dropped when using H polarization. We found then different temperature-dependent peaks: in samples 19-31 and 19-34, we detected similar peaks located at ≈(0.3,0,0.366) and ≈(0.285,0,0.48), respectively; in 19-35, instead, we detected two temperature-dependent peaks in (0.293, 0, 0.48) and (0.305, 0, 0.41): they both disappeared above 80 K.

Bibliography

[1] Gaetano Campi et al. "Inhomogeneity of charge-density-wave order and quenched disorder in a high-T c superconductor". *Nature* 525 (2015), p. 359 (cit. on pp. 1, 20, 39, 53).

[2] R. Arpaia et al. "Dynamical charge density fluctuations pervading the phase diagram of a Cu-based high-Tc superconductor". *Science* 365 (2019), pp. 906–910 (cit. on pp. 2, 7, 21, 59).

[3] Leon N Cooper. "Bound electron pairs in a degenerate Fermi gas". *Physical Review* 104 (1956), p. 1189 (cit. on p. 3).

[4] J George Bednorz and K Alex Müller. "Possible highT c superconductivity in the Ba- La- Cu- O system". *Zeitschrift für Physik B Condensed Matter* 64 (1986), pp. 189–193 (cit. on p. 4).

[5] Neven Barišić et al. "Universal sheet resistance and revised phase diagram of the cuprate high-temperature superconductors". *Proceedings of the National Academy of Sciences* 110 (2013), pp. 12235–12240 (cit. on pp. 4, 14).

[6] DG Hawthorn et al. "Resonant elastic soft x-ray scattering in oxygen-ordered YBa 2 Cu 3 O 6+ δ". *Physical Review B* 84 (2011), p. 075125 (cit. on p. 4).

[7] Philip W Anderson. "The resonating valence bond state in La2CuO4 and superconductivity". *science* 235 (1987), pp. 1196–1198 (cit. on p. 4).

[8] Bernhard Keimer et al. "From quantum matter to high-temperature superconductivity in copper oxides". *Nature* 518 (2015), p. 179 (cit. on pp. 5–7).

[9] G Roth et al. "On the structure of non-superconducting YBa 2 Cu 3 O 6+ x". *Zeitschrift für Physik B Condensed Matter* 69 (1987), pp. 53–59 (cit. on p. 5).

[10] Mathieu Le Tacon et al. "Intense paramagnon excitations in a large family of high-temperature superconductors". *Nature Physics* 7 (2011), p. 725 (cit. on pp. 5, 6).

[11] David Gustafsson et al. "Fully gapped superconductivity in a nanometre-size YBa 2 Cu 3 O 7–δ island enhanced by a magnetic field". *Nature nanotechnology* 8 (2013), p. 25 (cit. on p. 6).

[12] Dale J Van Harlingen. "Phase-sensitive tests of the symmetry of the pairing state in the high-temperature superconductors—evidence for d x 2- y 2 symmetry". *Reviews of Modern Physics* 67 (1995), p. 515 (cit. on p. 6).

[13] Nicolas Doiron-Leyraud et al. "Quantum oscillations and the Fermi surface in an underdoped high-T c superconductor". *Nature* 447 (2007), p. 565 (cit. on pp. 6, 7).

[14] MR Norman et al. "Destruction of the Fermi surface in underdoped high-T c superconductors". *Nature* 392 (1998), p. 157 (cit. on p. 6).

[15] Q Li et al. "Two-dimensional superconducting fluctuations in stripe-ordered La 1.875 Ba 0.125 CuO 4". *Physical review letters* 99 (2007), p. 067001 (cit. on p. 6).

[16] S Blanco-Canosa et al. "Resonant x-ray scattering study of charge-density wave correlations in YBa 2 Cu 3 O 6+ x". *Physical Review B* 90 (2014), p. 054513 (cit. on pp. 6, 13, 26, 35).

[17] JM Tranquada et al. "Evidence for stripe correlations of spins and holes in copper oxide superconductors". *nature* 375 (1995), p. 561 (cit. on pp. 6, 8, 9).

[18] R Daou et al. "Broken rotational symmetry in the pseudogap phase of a high-T c superconductor". *Nature* 463 (2010), p. 519 (cit. on p. 6).

[19] CM Varma et al. "Phenomenology of the normal state of Cu-O high-temperature superconductors". *Physical Review Letters* 63 (1989), p. 1996 (cit. on p. 7).

[20] G Seibold et al. "Marginal Fermi Liquid behaviour from charge density fluctuations in cuprates". *arXiv preprint arXiv:1905.10232* (2019) (cit. on p. 7).

[21] C Castellani, C Di Castro, and M Grilli. "Singular quasiparticle scattering in the proximity of charge instabilities". *Physical review letters* 75 (1995), p. 4650 (cit. on p. 7).

[22] Riccardo Comin and Andrea Damascelli. "Resonant x-ray scattering studies of charge order in cuprates". *Annual Review of Condensed Matter Physics* 7 (2016), pp. 369–405 (cit. on pp. 8, 11, 16, 17, 19, 27, 30, 39, 44, 50, 51, 59, 63).

[23] K Yamada et al. "Doping dependence of the spatially modulated dynamical spin correlations and the superconducting-transition temperature in La 2- x Sr x CuO 4". *Physical Review B* 57 (1998), p. 6165 (cit. on pp. 8, 9).

[24] JE Hoffman et al. "A four unit cell periodic pattern of quasi-particle states surrounding vortex cores in Bi2Sr2CaCu2O8+ δ". *Science* 295 (2002), pp. 466–469 (cit. on p. 10).

[25] G Ghiringhelli et al. "Long-range incommensurate charge fluctuations in (Y, Nd) Ba2Cu3O6+ x". *Science* 337 (2012), pp. 821–825 (cit. on pp. 11, 19, 26, 27, 32, 35, 39, 45, 47, 51, 59, 64, 67).

[26] Andrej Mesaros et al. "Commensurate 4a0-period charge density modulations throughout the Bi2Sr2CaCu2O8+ x pseudogap regime". *Proceedings of the National Academy of Sciences* 113 (2016), pp. 12661–12666 (cit. on p. 12).

[27] G De Vecchi. "Charge Order Discommensurations and Fluctuations in Cuprate Superconductors studied by Resonant Inelastic X-ray Scattering". Master thesis. Politecnico di Milano, 2017 (cit. on pp. 12, 26, 39–41, 51).

[28] J Chang et al. "Direct observation of competition between superconductivity and charge density wave order in YBa 2 Cu 3 O 6.67". *Nature Physics* 8 (2012), p. 871 (cit. on pp. 12, 24, 26).

[29] S Blanco-Canosa et al. "Momentum-dependent charge correlations in YBa 2 Cu 3 O 6+ δ superconductors probed by resonant X-ray scattering: Evidence for three competing phases". *Physical review letters* 110 (2013), p. 187001 (cit. on pp. 12, 35).

[30] W Tabis et al. "Charge order and its connection with Fermi-liquid charge transport in a pristine high-T c cuprate". *Nature communications* 5 (2014), p. 5875 (cit. on pp. 14–16, 26).

[31] Eduardo H da Silva Neto et al. "Charge ordering in the electron-doped superconductor Nd2–xCexCuO4". *Science* 347 (2015), pp. 282–285 (cit. on pp. 14, 16).

[32] Eduardo H da Silva Neto et al. "Ubiquitous interplay between charge ordering and high-temperature superconductivity in cuprates". *Science* 343 (2014), pp. 393–396 (cit. on pp. 18, 26, 35).

[33] Simon Gerber et al. "Three-dimensional charge density wave order in YBa2Cu3O6. 67 at high magnetic fields". *Science* 350 (2015), pp. 949–952 (cit. on pp. 18, 19).

[34] Tao Wu et al. "Emergence of charge order from the vortex state of a high-temperature superconductor". *Nature communications* 4 (2013), p. 2113 (cit. on p. 19).

[35] M Minola. "Magnetic, orbital and charge fluctuations in layered cuprates studied by resonant soft x-ray scattering". Phd thesis. Politecnico di Milano, 2013 (cit. on pp. 24, 26).

[36] P Abbamonte et al. "Spatially modulated'mottness' in La 2-x Ba x CuO 4". *Nature Physics* 1 (2005), p. 155 (cit. on pp. 24, 25, 29).

[37] C Dallera et al. "Charge-transfer excitations in lanthanum compounds measured by resonant inelastic x-ray scattering at the M 5 edge". *Physical Review B* 64 (2001), p. 153104 (cit. on p. 24).

[38] Eugen Weschke and Enrico Schierle. "The UE46 PGM-1 beamline at BESSY II". *Journal of large-scale research facilities JLSRF* 4 (2018), p. 127 (cit. on p. 25).

[39] Sergio Caprara et al. "Dynamical charge density waves rule the phase diagram of cuprates". *Physical Review B* 95 (2017), p. 224511 (cit. on pp. 26, 39).

[40] Luuk JP Ament et al. "Resonant inelastic x-ray scattering studies of elementary excitations". *Reviews of Modern Physics* 83 (2011), p. 705 (cit. on pp. 27, 29, 30).

[41] G Dellea. "Collective excitations in high temperature superconducting cuprates studied by resonant inelastic soft x-ray scattering". Phd thesis. Politecnico di Milano, 2016 (cit. on pp. 32, 58).

[42] Helmholtz-Zentrum Berlin. *Bessy II*. 2012. URL: https://www.helmholtz-berlin.de (cit. on pp. 33, 35, 37).

[43] J Clarke. *Insertion Devices lecture 4: Undulator Magnet Designs*. 2013. URL: https://www.cockcroft.ac.uk/wp-content/uploads/2014/12/Lecture-4.pdf (cit. on p. 35).

[44] U Englisch et al. "The elliptical undulator UE46 and its monochromator beam-line for structural research on nanomagnets at BESSY-II". *Nuclear Instruments and Methods in Physics Research Section A: Accelerators, Spectrometers, Detectors and Associated Equipment* 467 (2001), pp. 541–544 (cit. on pp. 34, 35).

[45] J Clarke. *Insertion Devices lecture 2: Wigglers and Undulators*. 2014. URL: https://www.cockcroft.ac.uk/wp-content/uploads/2014/12/CLarke-Lecture-2.pdf (cit. on p. 35).

[46] R Comin et al. "Charge order driven by Fermi-arc instability in Bi2Sr2-xLaxCuO6+ δ". *Science* 343 (2014), pp. 390–392 (cit. on p. 35).

[47] H Petersen et al. "Review of plane grating focusing for soft x-ray monochromators". *Review of scientific instruments* 66 (1995), pp. 1–14 (cit. on p. 36).

[48] G Papari et al. "High critical current density and scaling of phase-slip processes in YBaCuO nanowires". *Superconductor Science and Technology* 25 (2012), p. 035011 (cit. on p. 41).

[49] Peter Larsson, Bengt Nilsson, and ZG Ivanov. "Fabrication and transport measurements of YBa 2 Cu 3 O 7- x nanostructures". *Journal of Vacuum Science & Technology B: Microelectronics and Nanometer Structures Processing, Measurement, and Phenomena* 18 (2000), pp. 25–31 (cit. on p. 41).

[50] Ke Xu and James R Heath. "Long, highly-ordered high-temperature superconductor nanowire arrays". *Nano letters* 8 (2008), pp. 3845–3849 (cit. on p. 41).

[51] Riccardo Arpaia et al. "Improved nanopatterning for YBCO nanowires approaching the depairing current". *IEEE Transactions on Applied Superconductivity* 23 (2013), pp. 1101505–1101505 (cit. on p. 41).

[52] Riccardo Arpaia et al. "Probing the phase diagram of cuprates with YBa 2 Cu 3 O 7- δ thin films and nanowires". *Physical Review Materials* 2 (2018), p. 024804 (cit. on p. 41).

[53] Shahid Nawaz et al. "Approaching the theoretical depairing current in YBa2Cu3O7- x nanowires". *Physica C: Superconductivity* 495 (2013), pp. 33–38 (cit. on p. 41).

[54] Shahid Nawaz et al. "Microwave Response of Superconducting Y Ba 2 Cu 3 O 7- δ Nanowire Bridges Sustaining the Critical Depairing Current: Evidence of Josephson-like Behavior". *Physical review letters* 110 (2013), p. 167004 (cit. on p. 41).

[55] Reza Baghdadi et al. "Fabricating nanogaps in YBa 2 Cu 3 O 7- δ for hybrid proximity-based Josephson junctions". *Physical Review Applied* 4 (2015), p. 014022 (cit. on p. 41).

[56] E Trabaldo et al. "Transport and noise properties of YBCO nanowire based nanoSQUIDs". *Superconductor Science and Technology* 32 (2019), p. 073001 (cit. on p. 41).

[57] Reza Baghdadi et al. "Toward YBa2Cu3O7-x Nanoscale Structures for Hybrid Devices". *IEEE Transactions on Applied Superconductivity* 25 (2014), pp. 1–4 (cit. on p. 41).

[58] Riccardo Arpaia et al. "YBa2Cu3O7- δ nanorings to probe fluxoid quantization in High Critical Temperature Superconductors". *Physica C: Superconductivity and its Applications* 506 (2014), pp. 184–187 (cit. on p. 41).

[59] S Charpentier et al. "Hot spot formation in electron-doped PCCO nanobridges". *Physical Review B* 94 (2016), p. 060503 (cit. on p. 41).

[60] Reza Baghdadi et al. "Study of in-plane electrical transport anisotropy of a-axis oriented YBa 2 Cu 3 O 7- δ nanodevices". *Physical Review B* 95 (2017), p. 184505 (cit. on p. 56).

[61] YY Peng et al. "Re-entrant charge order in overdoped (Bi, Pb) 2.12 Sr 1.88 CuO 6+ δ outside the pseudogap regime". *Nature materials* 17 (2018), p. 697 (cit. on p. 65).

[62] B Fisher et al. "Hopping conductivity in fully oxygenated PrBa 2 Cu 3 O y, YBa 2 Cu 2 CoO y, and PrBa 2 Cu 2 CoO y". *Physical Review B* 50 (1994), p. 4118 (cit. on p. 71).

[63] S Uma et al. "Magnetic ordering in single crystals of". *Journal of Physics: Condensed Matter* 10 (1998), p. L33 (cit. on p. 71).

Acknowledgements

Beamtime Acknowledgements

We thank HZB for the allocation of synchrotron radiation beamtime.

Funding Acknowledgements

This project has received funding from the European Union's Horizon 2020 research and innovation programme under grant agreement No 730872.

Personal Acknowledgements

First, I would like to express my gratitude to my supervisor, Prof. Giacomo Ghiringhelli, for finding the time and patience to answer my questions and guide me through the realization of this work, which would have been impossible without his help. I also want to sincerely thank the other members of this brilliant group, with whom I had the pleasure to work. Prof. Lucio Braicovich, whose achievements and career are a source of inspiration for every young physicist here at Politecnico. Riccardo, my co-supervisor, for transmitting me his passion and dedication, and for having patiently corrected this thesis. Roberto, for all the support and advice he has given me, both during these months and the beam-times. Matteo and Marco, for their kindness and optimism, which made me feel a part of this team. I want then to cite my lab-mates: Mattia, Pietro and Paolo, thank you for making that room a happy place to work in, and for all the discussions about Physics, about our Future and about ItaliaGuerraBot. I would like to thank my family, that supported me over all these years of sacrifices and studies, without which nothing of what I have achieved would be possible. You have always been an inspiration to me, and you will forever have my deepest gratitude; I hope to have made you proud. I want to extend this gratitude to my friends, for all the moments, laughs and experiences that made these years lighter.

And, finally, I want to thank the girl with whom I shared all the failures, successes, joys and anxiety of these University years.
Thank you, Charlotte.

Milano, October 2019 L. M.